International
Progress Report

IPR-05-37

Äspö Hard Rock Laboratory

TRUE Block Scale continuation project

Analysis of reactive transport in a fault structure and associated background fractures

Daniel Billaux

Itasca Consultants

September 2005

Svensk Kärnbränslehantering AB
Swedish Nuclear Fuel
and Waste Management Co
Box 5864
SE-102 40 Stockholm Sweden
Tel 08-459 84 00
+46 8 459 84 00
Fax 08-661 57 19
+46 8 661 57 19

Äspö Hard Rock
Laboratory

Report no.
IPR-05-37
No.
F56K
Author
Daniel Billaux
Date
September 2005
Checked by
Anders Winberg
Date
September 2006
Approved
Anders Sjöland
Date
2006-11-29

Äspö Hard Rock Laboratory

TRUE Block Scale continuation project

Analysis of reactive transport in a fault structure and associated background fractures

Daniel Billaux

Itasca Consultants

September 2005

Keywords: Channel, DFN, Fault, Flow, Fracture, In-situ, Network, Prediction, Retention, Sorbing, Tracer

Executive summary

Context

The TRUE Block Scale Continuation project was prompted by the realisation that a number of questions remained unanswered after the TRUE Block Scale project. It was decided that these pending questions would be expressed in the form of hypotheses. Among these, this modelling work focuses on the following: "*Transport at experimental time scales is significantly different for faults (significant alteration, brecciation and fault gouge) and joints (with or without alteration), due to the indicated differences in microstructure and properties*"

The model

Structure related data, as well as fracture intersection positions and transmissivities along boreholes are directly included as deterministic data in the model (the main feature in the investigated part of the volume under study is Structure #19). The rest of the fracture network (i.e. background fractures that do not intersect the boreholes) is represented as a stochastic model with statistical geometrical properties. Flow and transport paths are simulated by projecting grids of 1D channels on the various features

Calibration and predictions

First, flow-only calibration uses the drawdown observed during in-situ pre-tests CPT-1 to CPT-3 to assess the transmissivity of Structure #19 and the distribution of transmissivities of the background fractures; then the non-reactive transport properties are calibrated based on the CPT-4a, CPT-4b and CPT-4c tracer tests.

For a given type of feature, (i.e. structure, or background fracture), we distribute the various immobile pore spaces between the channels according to the areas we assume they occupy in this feature type. At this stage, we chose to consider the presence of only a minimal amount of fault gouge, with 5% of the area of Structure #19 concerned.

The calibration yields the following tentative conclusions:

- We need to introduce very heterogeneous structures, with a fairly large wetted surface;
- The calibrated background fracture properties are those of simpler features: less wetted surface per fracture area, smaller apertures for a given transmissivity;
- Diffusion is needed to properly account for the experimental results;
- Structure (#19) response for one realization is already "averaged", there is no major difference between single-realization and multiple-realization-averaged breakthrough curves;
- Background fracture response varies widely between realizations. Breakthrough curves averaged over realizations then have little meaning, because of the wide range of variations in the potential actual response.

Numerical prediction of two reactive transport experiments – the two BS2B tests, on flow paths I (inside Structure #19) and II (tracer injected in a background fracture and recovered in Structure #19) using the calibrated properties is then compared to the actual measurements. The numerical predictions lack significant retardation. Also, the initial rise of the breakthrough curves is too steep, indicating a lack of dispersivity (or, equivalently, of small scale heterogeneity) in the model.

Transport parameters

The discrepancy between simulations and measurements can be traced mostly to a probable underestimate of the amount of gouge present. With this remediated, the new simulations are close to the experimental results. Furthermore, the new transport parameters used for the evaluation are also compatible with the earlier tests CPT-4a, CPT-4b and CPT-4c. This means that the evaluation parameters we chose provide a consistent model, able to reproduce adequately all observed behaviour.

However, a negative implication is that very different retardation behaviours can be obtained for two sets of parameters, both yielding almost identical responses for the calibration tests simulations. The calibration as performed here did not provide enough constraints to accurately predict the later runs.

Flow paths

While Flow path I is, predictably, almost exclusively confined to Structure #19, Flow path II is also limited to a few background fractures before tracers reach the sink constituted by Structure # 19, as illustrated by the figure below.

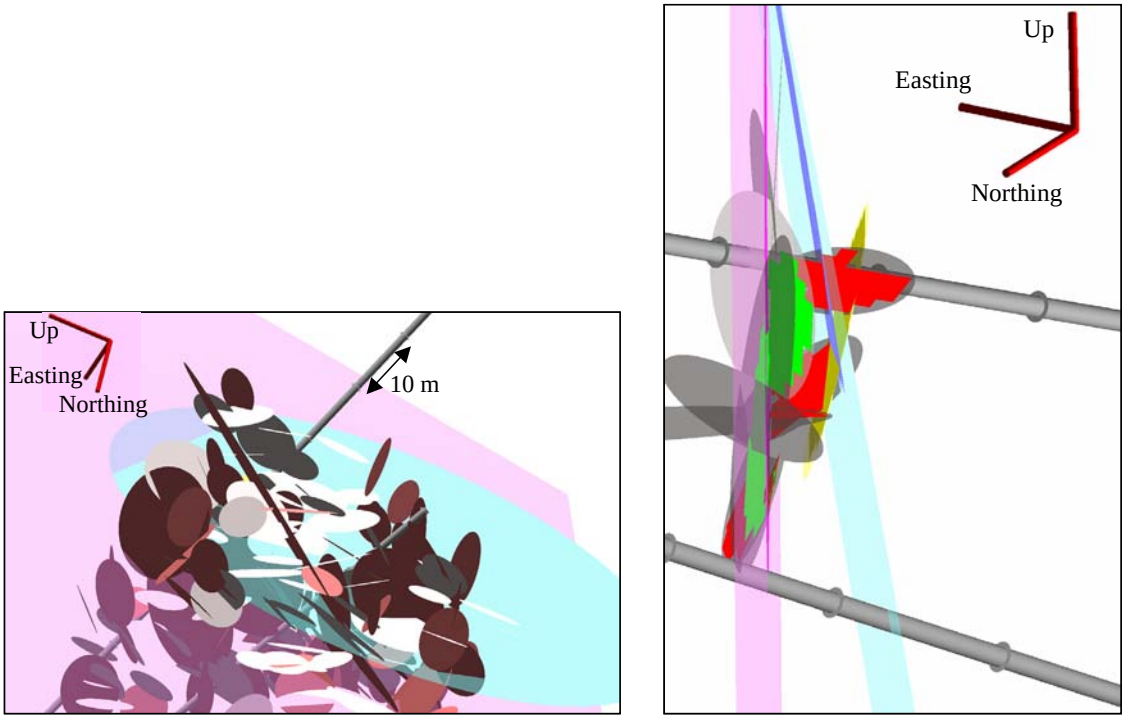

General view of the model, with Structure #19 in pink in the background (left), and fractures supporting the transport paths (right).

Överblick av modellen med Struktur #19 i bakgrunden (rosa) med övriga sprickor som bygger upp transportvägarna (höger).

Difficulties

The scale we are considering here is probably way below the Representative Elementary Volume (REV) for transport in this network, if such a REV exists. We are therefore relying on a "point statistic" (i.e. one realisation) to make deductions about differences between structures and background fractures.

Whereas fault gouge seems to have a major effect on the in-situ tests performed, it would essentially act as a thin coating and be saturated fairly rapidly in long term "repository" conditions. Therefore, the one part of the system that most influences its behaviour at the time scale we can investigate is probably not important for the time scale we are really interested in.

Conclusions

Background fractures and structures can be studied independently of each other: on one hand, a path originating and finishing in the same structure will be extremely unlikely to leave the structure, because of the structure higher conductivity, and therefore will be insensitive to background fracture network properties. On the other hand, the use of a structure as a "sink" for a path originating in a background fracture permits acceptable recoveries, while travel is so much faster in the structure that we can disregard the part of the transport path in the structure, and consider only reactive transport in the background fractures network.

Coming back to the initial hypothesis, indeed, transport is significantly different for structures and for background fractures. However, contrasts in microstructure and properties are only one aspect of the difference. A structure is a "known" object (although imperfectly known), with a defined conceptual framework. For background fracture transport, geometry cannot be known deterministically. At the scale involved, the same network statistical properties can yield realizations with widely different behaviours.

When studying a nuclear waste repository, the behaviour of many possible transport paths shall be anticipated, at scales close to the one studied here (scale of the transport paths from deposition hole to the nearest structure), without the a priori knowledge, by the way of non-sorbing tracer tests, of these various transport paths. This will be a much more challenging task, for which we will need to revert to stochastic analyses.

Sammanfattning

Sammanhang

Projektet TRUE Block Scale Continuation föranleddes av att ett antal återstående frågeställningar som identifierats efter TRUE Block Scale projektet. Dessa frågeställningar uttrycktes som hypoteser. Bland dessa fokuserar det här presenterade modellarbetet på *”Transport på experimentella tidsskalor i förkastningssprickor (faults, med påtaglig omvandling, brecciering och lerigt sprickfylllnadsmaterial (fault gouge)) är signifikant annorlunda på grund av noterade skillnader i mikorostruktur och egenskaper*”.

Modellen

Struktur-relaterade data, liksom lägen för sprickkorningar och transmissivitetsdata längs borrhål används som deterministisk information i modellen (huvudstrukturen i den undersökta delen av bergvolymen är Struktur #19). Resten av spricknätverket (dvs bakgrundssprickor som inte skär borrhålen) representeras i en stokastisk modell med statistiskt underbyggda geometriska egenskaper. Flödes- och transportvägar simuleras genom att överlagra en beräkningsgriddar av 1D kanaler på de modellerade enheterna.

Kalibrering och prediktion

Kalibrering av flödesmodellen utnyttjar avsänkningsdata från de genomförda för-försöken CPT-1 till CPT-3 för att uppskatta fördelningen av transmissivitet i Struktur #19 och fördelningen av transmissivitet i bakgrundssprickorna. Därefter kalibrerades icke-reaktiva transportegenskaper baserat på spårförsöken CPT-4a, CPT4b och CPT4c.

För en given ingående komponent (struktur eller bakgrundspricka) kan de olika immobila porvolymerna fördelas mellan de olika kanalerna på basis av den yta de antas ockupera i denna typ av struktur. Det antas här att endast en liten andel (5%) av sprickfyllnad (fault gouge) existerar i den del av Struktur #19 som berörs av experimentet.

Kalibreringen gav följande översiktliga slutsatser:

- Behov att introducera mycket heterogena strukturer med mycket stor flödesvätt yta;
- De kalibrerade egenskaperna hos bakgrundssprickor visar på ”enklare strukturer” med mindre flödesvätt yta och mindre apertur för en given transmissivitet;
- Matrisdiffusion behövs för att förklara erhållna experimentella resultat;
- Erhållna resultat för Struktur#19 för en realisering är redan ”medelvärdesbildade”, det finns ingen större skillnad mellan en resultatet för enskild realisering och medelvärdesbildade resultat baserad på multipla realiseringar.
- Inverkan av bakgrundssprickor varierar stort mellan olika realiseringar. Medelvärdesbildning ab multipla realiseringar har därför liten mening då resultaten från enskilda realiseringar kan variera så stort.

Numeriska förutsägelser av de två reaktiva injiceringarna (BS2B) i flödesväg I(Struktur #19) och II (injicering i en bakgrundsspricka under pumpning i Struktur #19) med användande av kalibrerade egenskaper, jämfördes med experimentella resultat. Det kan noteras att de numeriska prediktionerna saknar signifikant retardation. Vidare är den initiala delen av genombrottskurvorna för brant, vilket indikerar brist på dispersion (eller analogt, brtist på småskalig heterogenitet) i modellen.

Transportparametrar

Bristen på överensstämmelse mellan modellprediktioner och experimentella data kan överlag härledas till en trolig underskattning av mängden sprickfyllnad längs flödesvägen. Med detta åtgärdat så erhålls en bättre överensstämmelse med de experimentella resultaten. Vidare är de transportegenskaper som används i utvärderingen också kompatibla med de som användes för att simulera tidigare försök; CPT-4a, CPT-4b och CPT-4c. Detta innebär att de parametrar som använts vid utvärderingen ger en konsistent modell som kan reproducera väl alla observationer. Men, en negativ aspekt är att mycket olika retardationsuppträdanden kan erhållas för två olika set av parametrar, som båda visat nära identiska utfall i samband med kalibreringen. Detta visar att den kalibrering som utförts hör inte gav tillräcklig avgränsning för att korrekt prediktera de efterföljande försöken.

Flödesvägar

Där flödesväg I, av naturliga skäl, företrädesvis är avgränsad till Struktur#19 så är flödesväg II avgränsad till ett fåtal bakgrundsprickor innan spårämnena når den huvudsakliga sänkan (pumpsektionen) som är etablerad i Struktur#19, se figur i den engelsk sammanfattningen.

Svårigheter

Den skala som vi analyserar här är troligen väsentligt mindre än REV (representativa elementarvolymen) för transport av lösta ämnen i ett spricknätverk., om ett sådant REV existerar. Vi förlitar oss därför på en ”punktstatistik” (en realiseraing) för att analysera skillnaderna mellan strukturer och bakgrundssprickor.

Där sprickfyllnad (fault gouge) verkar ha en markerad effekt på in situ försök, trots sin begränsade tjocklek, skulle den verka som en tunt yttre lager som skulle mättas relativt snabbt under de långa tider som är aktuella för ett geologiskt förvar. Därför kommer en komponent som är mycket betydelsefull för de tidsskalor vi studerar här att vara oväsentlig för de tidskalor vi verkligen är ute efter.

Slutsatser

Bakgrundssprickor och strukturer kan studeras oberoende av varandra: en flödesväg som börjar och slutar i samma struktur lämnar med stor sannolikhet inte denna struktur, och är därför oberoende av egenskaperna hos bakgrundssprickorna. Användande av en ”struktur” som sänka för en flödesväg som startar i en bakgrundsspricka medger acceptabel retur av injekterad massa, och då uppehållstiden i ”strukturen” är mycket kortare kan den del av transporten som sker i strukturen bortses ifrån, och den reaktiva transporten i nätverket av bakgrundssprickor analyseras.

För att återgå till den inledningsvis nämnda hypotesen, så är transport signifikant annorlunda i strukturer respektive bakgrundssprickor. Skillnader i mikrostruktur och egenskaper är endast en del av den noterade skillnaden. En struktur är ett ”känt” objekt (om än ofullständigt känt), som dessutom är del av ett väldefinierat konceptuellt ramverk. För transport i bakgrundssprickor är geometrin av detta nätverk inte känt deterministiskt. På den aktuella skalan kan samma statistiska nätverksparametrar ge realiseringar med väsentligt olika egenskaper.

För ett förvar för radioaktivt avfall förväntas analys av många möjliga flödesvägar på skalor motsvarande den som analyserats i denna studie, utan kunskap från icke-sorberande försök i dessa. Detta kommer att vara en mycket stor utmaning där man förmodligen måste utnyttja stokastisk analys.

Contents

List of Figures

List of Tables

1 Introduction

1.1 Hypotheses

The TRUE Block Scale Continuation (or TRUE-BSC) project was prompted by the realisation that a number of questions remained unanswered after the TRUE Block Scale project (TRUE BS). It was decided that these pending questions would be expressed in the form of hypotheses. Hypotheses were chosen for their relevance (i.e. they correspond to unanswered questions), and for their "verifiability" within the technical and financial constraints of the new experimental program. The following main hypotheses were selected when designing the tracer tests.

- **Hypothesis I a)** Microstructural (i.e. detailed geological, mineralogical and geochemical) information can provide significant support for predicting transport of sorbing solutes at experimental time scales,
- **Hypothesis I b)** Transport at experimental time scales is significantly different for faults (significant alteration, brecciation and fault gouge) and joints (with or without alteration), due to the indicated differences in microstructure and properties,
- **Hypothesis I c)** Longer distance pathways are dominated by fault rock zone behaviour, while shorter pathways (representative for fractures in the vicinity of a deposition hole) may be more likely to be dominated by joint fracture characteristics.
- **Hypothesis II c)** Fracture retention properties tend to be scale-dependent primarily due to differences in microstructure.

Among these hypotheses, Hypothesis I a) questions the conceptual framework of the whole exercise: "taking a macro hydrostructural model, adding to it microstructure information should enable the prediction of reactive tracer behaviour". It will be supported mostly by successful (close enough to experimental results) and consistent (any two successful models should not be based on widely varying assumptions) predictions. In other words, although this hypothesis can be addressed by an individual modelling team, its resolution is really contingent on the comparison of the various models.

Because the final reactive tracer tests (denoted BS2B), as shown in subsequent sections, involve both a Structure and a Background fracture, Hypothesis I b) can also be substantiated or refuted, at least in part, by the experiment and its evaluation. The last two hypotheses above will be more difficult to study based on the experimental results, because in fact the reactive tracer tests investigate very similar transport path lengths.

The ANDRA/Itasca team has focussed, during the project, on the relative effect of the background fractures and structures (here, almost exclusively Structure #19, as far as reactive transport is concerned). As such, this work applies foremost to Hypothesis I b), and to a lesser degree to Hypotheses I c) and II c).

1.2 Work phases

The TRUE-BSC project was organized, over a shorter time frame, with the same flexibility as the previous TRUE BS project. Several iterations of investigation were performed, each followed by an evaluation and adaptation of the design of the next phase. In the early phases of such a program, modelling can be a help in 1) scoping and 2) interpreting intermediate results. During the first phase of the TRUE-BSC project (BS2A), the feasibility of reactive tracer tests, both within Structure 19 and from background fractures to a sink in Structure 19 was evaluated. Itasca participated in scoping calculations [Darcel, 2003] that concluded on the feasibility of such tests, on the condition that pathways in the background fracture system would be fairly short, and that the sink would be located in a Structure in order to achieve an acceptable recovery rate for the radioactive reactive tracers. Interference pre-tests named CPT-1, CPT-2 and CPT-3 [Andersson et al., 2004, IPR-04-25] were performed, with pumping located in the planned sink in Structure 19. A first batch of simulations were aimed at two goals:

- Verify that the experimental results are compatible with our prior knowledge or assumptions concerning Structure 19 and its environment, and more generally with the hydrostructural model as described by [Andersson et al., 2002, TR-02-13].
- check that hydraulic results from these tests confirm the feasibility of performing the reactive tracer tests.

These simulations are reported in Chapter 3.

After checking hydraulic results, a new batch of tests was performed, this time using non-reactive tracers. The main aim of these tests was to qualify the proposed experimental setup for the use of radioactive tracers, by showing tracer recoveries in excess of 70% of the injected mass. These tests used the same sink as CPT-3, and are named CPT-4a, CPT-4b and CPT-4c [Andersson et al., 2004, IPR-04-25]. We first use the results of these tests to calibrate the transport properties of Structure #19 and the background fractures, as described in Section 4.1.

We then set out to predict the results of reactive tracer tests, using the calibrated model and specifications for the retention properties of the various defined immobile zones of the microstructural model for the respective tracers (Section 4.2). After comparing the blind simulations with the actual test results, we evaluate the model by checking which parameters may best explain the discrepancies (Section 5) and testing the significance of the differences between Structure #19 and the background fracture population. Finally, Sections 6 and 7 discuss and conclude this work.

2 Modelling choices and model building

2.1 Hypotheses

The present model builds upon the one previously used to assess feasibility of the TRUE Block Scale Continuation project [Darcel 2003]. Most of the model's current characteristics are inherited from this previous model. Structure related data, as well as fracture intersection positions and transmissivities along boreholes are directly included as deterministic data in the model. The rest of the fracture network (i.e. background fractures that do not intersect the boreholes) is represented as a stochastic model with statistical geometrical properties.

Flow and transport paths are simulated by projecting grids of 1D channels on the various features, and also considering intersections between the features as channels, therefore providing for the connectivity of the flow/transport network. Furthermore, for transport, full mixing is assumed at channel intersections.

2.2 Model extent and boundary conditions

The model extent was discussed between the various groups during the course of the project. The initial model was very much inherited from the Äspo HRL task 6C model developed by [Dershowitz et al., 2003]. As such, it encompassed a 200 m side cube (BS2 Experimental volume), with boundary conditions as shown in Figure 2-1, taken from the above mentioned report, except the South face which we chose to set to no flow. Figure 2-2 shows the position of this cube relative to the underground galleries (in blue) and to the TRUE Block Scale boreholes (in black). Also shown in this figure are the pumping and head measurement nodes (respectively in red and blue) in the model, for the CPT-1 test, and the cylinder that limits the domain for generation of background fractures.

It was decided later in the project that the 200m cube, together with the boundary heads provided for it, could be advantageously replaced by a 500m cube and another set of boundary heads fitted by the JNC/Golder team [Dershowitz et al., in prep.]. For example, one can readily see on Figure 2-2 that the (red) pumping node for test CPT-1 is very close to the boundaries of the initial model, casting doubt on the correctness of imposing constant conditions, be them heads or flow, on all the cube faces. Figure 2-3 shows the 500 m cubic domain, with the same details as in Figure 2-2, for the CPT-1 test, and using the same scale. The heads obtained in the model using the new boundary conditions, and without any pumping or injection in the TRUE Block Scale rock volume, are shown on Figure 2-4.

We are in fact interested in the flow and transport in the vicinity of Structure #19. We already know that large deterministic structures account for most of the flow that occur in the rock mass: they were chosen, among other criteria, for that purpose. Therefore, we consider that when pumping in Structure #19, flow paths to the model cube boundaries will be through the deterministic structures, with background fractures providing local shortcuts, but no significant long path. Accordingly, we generate background fractures only in the main region of interest, centred on the pumping point.

Background fracture centres are sampled only from this cylinder. Note that a fracture may extend outside of the generation region and will not be truncated at its boundary. Also, conditioned background fractures are assigned on a borehole only along the portion of the borehole that is inside the generation region.

Examples of the background fracture generation region are shown in Figure 2-2 (initial model) and Figure 2-3 (final model used for the simulations). It is a cylinder, with its centre at the pumping point, with its axis normal to Structure #19. For the CPT-1 (Figure 2-3), CPT-2 (Figure 2-5) and CPT-3 (Figure 2-6) tests, we chose a cylinder with a radius of 120 m and a 40 m long axis. For the CPT-4a, CPT-4b, and CPT-4c tests discussed later, the cylinder is smaller: a 25 m radius and a 40 m long axis.

Finally, we restrict the model domain further, for tests CPT-4a, CPT-4b and CPT-4c, and also for the later BS2B series of tests. In all these tests, pumping as well as most of the tracer injections are located in Structure #19, and the few remaining injections are located very close to Structure #19, in what is labelled as Background Fracture 1 (BG1). Whereas the hydraulic modelling requires a fairly large domain, transport during these tests is much more of a local phenomenon. Because the sink is much stronger than the injection sources and is located in a relatively conductive structure, transport paths do not deviate significantly from the geometric region between the injection and pumping points. We take advantage of this fact by using a much smaller domain for transport. A simulation is then performed in two steps. First, the steady-state heads due to the pumping and injections are computed using the 500 m – sided domain. A new transport domain is then defined, by taking a box, parallel to the coordinate axes, such that all injection and pumping points for a given test are included in the model, and are situated at least 5 m away from the model boundaries. Figure 2-7 to Figure 2-9 show the corresponding inner boxes, together with the large 500 m domain, the cylindrical background fracture generation domain, boreholes, galleries, and pumping and injection points for tests CPT-4a, CPT-4b and CPT-4c respectively.

When simulating the pumping test in the large domain, nodes are added at the boundaries of the inner box for future use. These nodes have no effect on the results, but enable us to obtain the exact computed heads at these boundaries. The list of heads at these “inner boundaries” is saved. The small model is then built, with a finer grid, and the list of heads is used to set the boundary conditions of the small model for transport. When using the inner model, we then check that the flows at its boundaries are similar to the ones crossing the same – then virtual - boundaries in the large model.

For all the tests simulated in this work, flow rates measured during the actual test, or planned flow rates, are imposed at the given borehole sections.

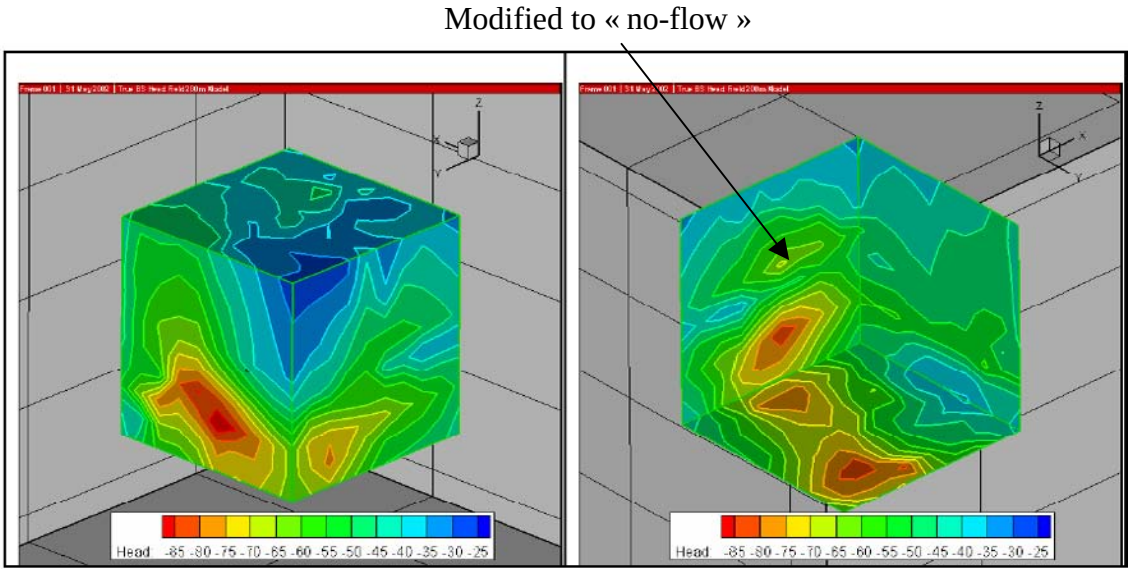

Figure 2-1: *Boundary conditions on the 200m block. X is Easting, Y is Northing, Z is upward. After [Dershowitz et al., 2003]*

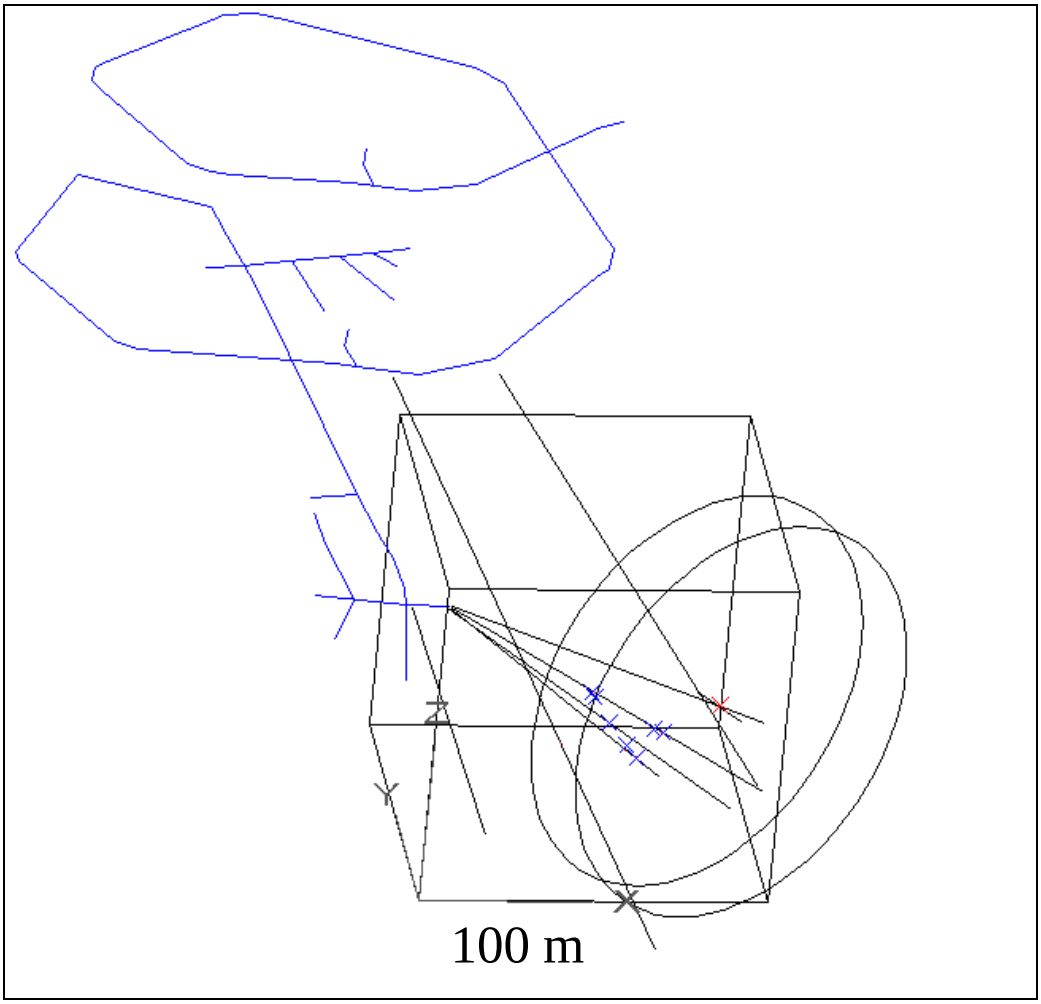

Figure 2-2: *Setup for CPT-1 test. View of the initial model domain, a 200m block, with galleries, boreholes. X is Southing, Y is Easting, Z is upward.*

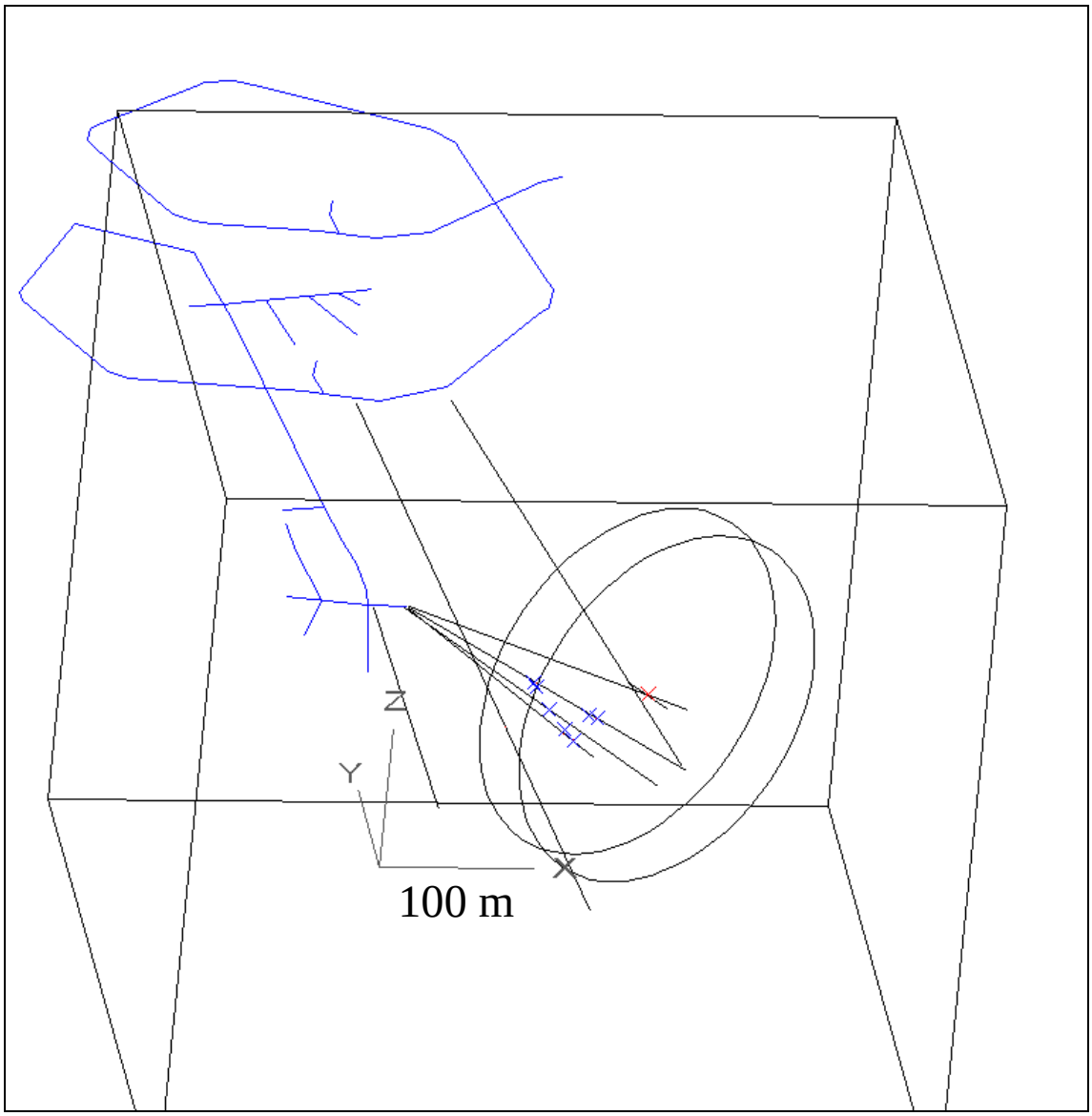

Figure 2-3: *Setup for CPT-1 test. View of the new model domain, a 500m block, with galleries, boreholes, cylindrical BG fracture generation domain. X is Southing, Y is Easting, Z is upward.*

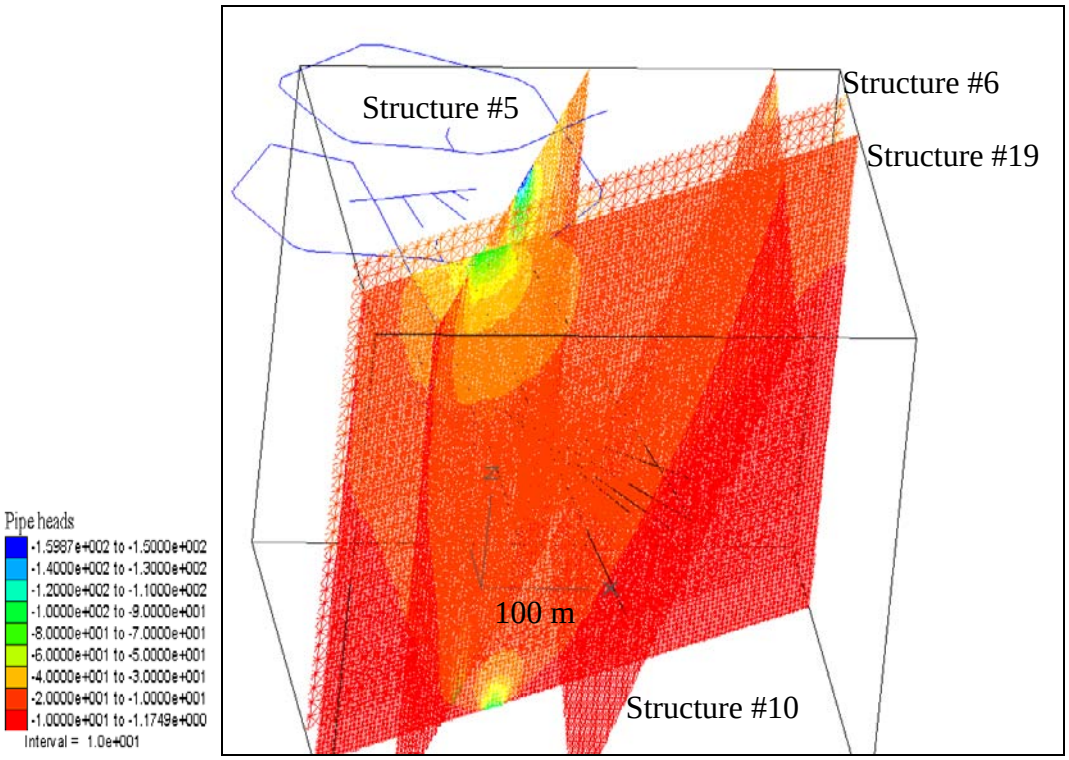

Figure 2-4: *View of the hydraulic head in deterministic structures. 500m block, with galleries, boreholes. X is Southing, Y is Easting, Z is upward.*

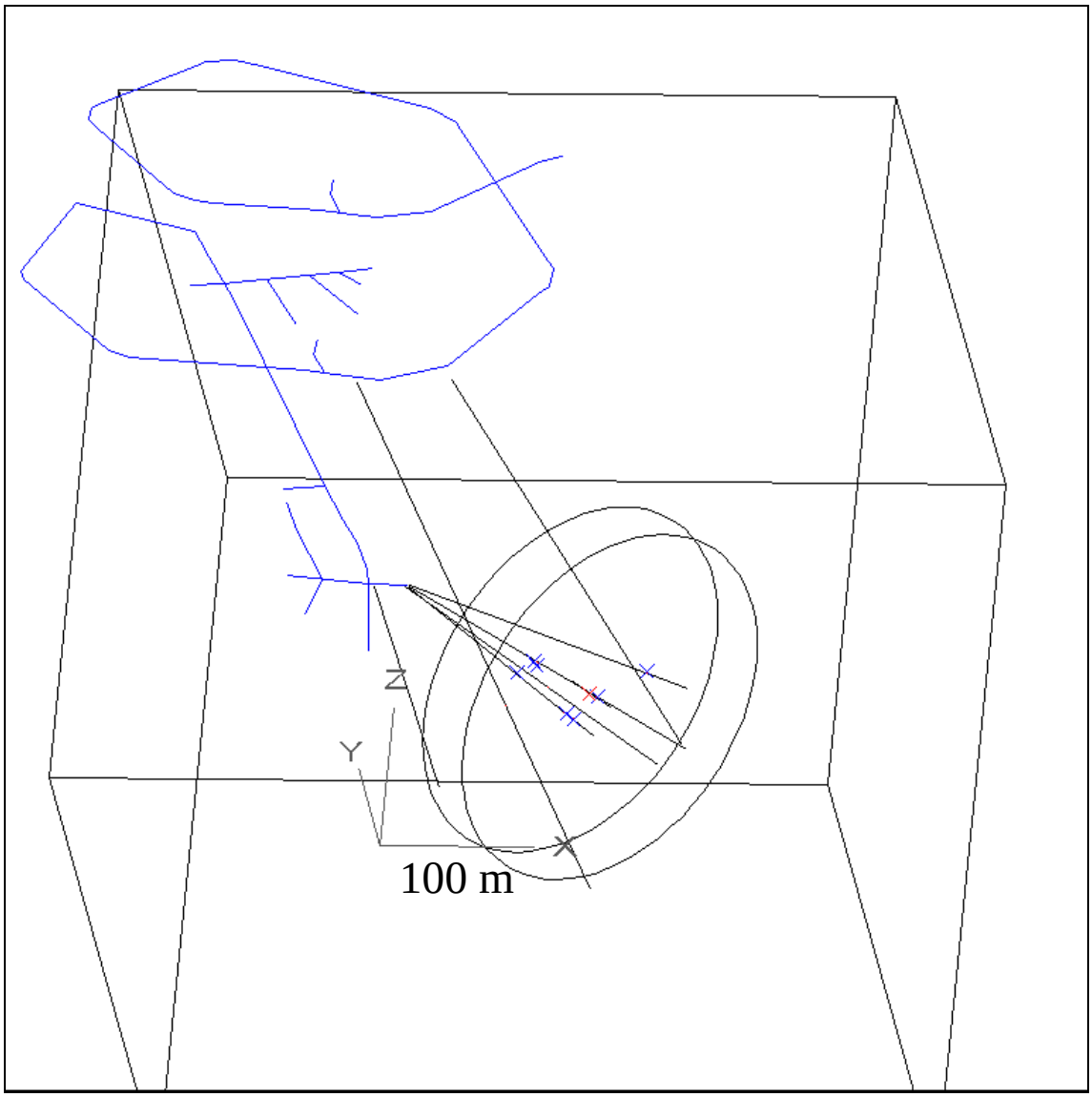

Figure 2-5: *Setup for CPT-2 test. View of the new model domain, a 500m block, with galleries, boreholes, cylindrical BG fracture generation domain. X is Southing, Y is Easting, Z is upward.*

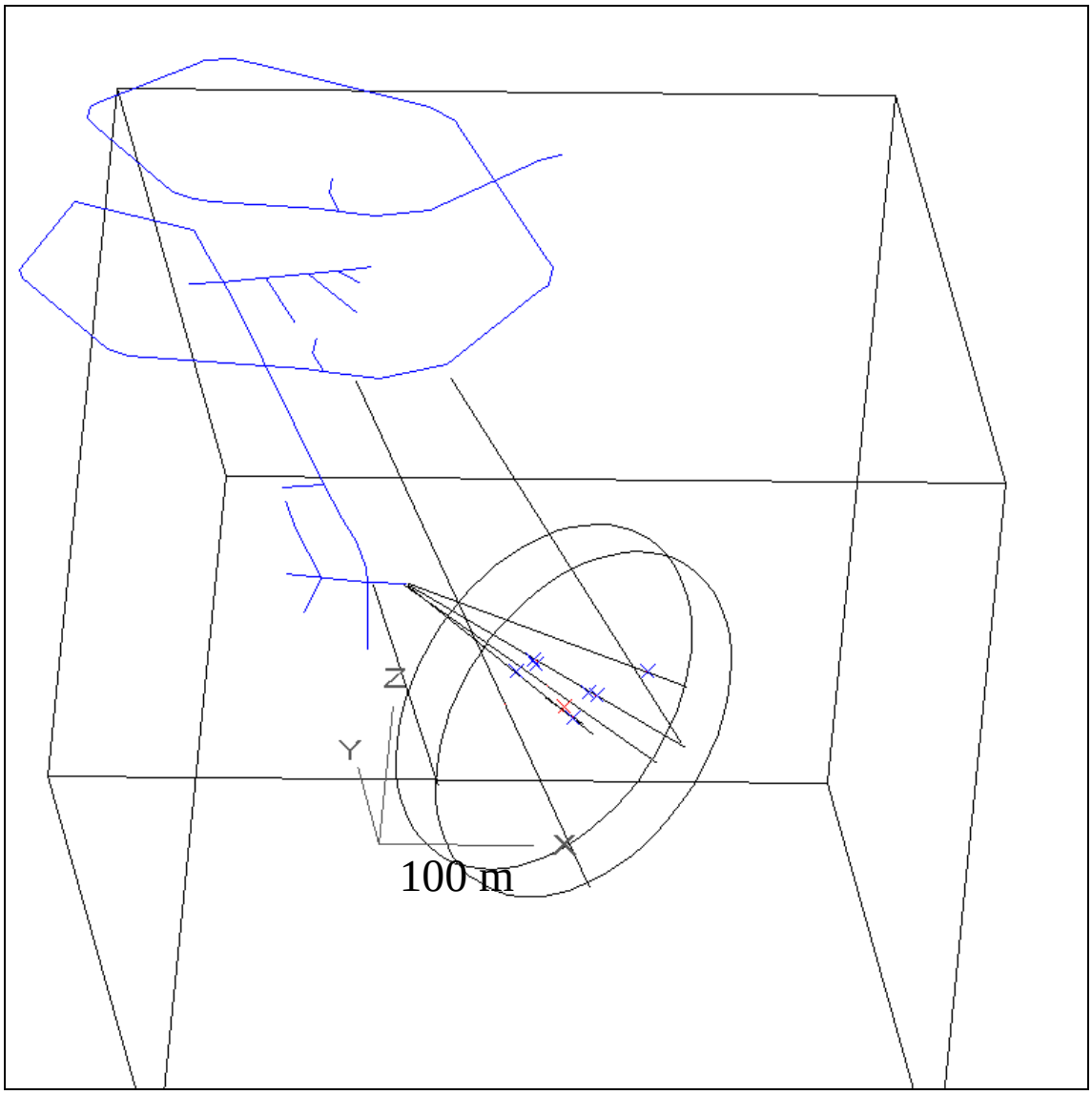

Figure 2-6: *Setup for CPT-3 test. View of the new model domain, a 500m block, with galleries, boreholes, cylindrical BG fracture generation domain. X is Southing, Y is Easting, Z is upward.*

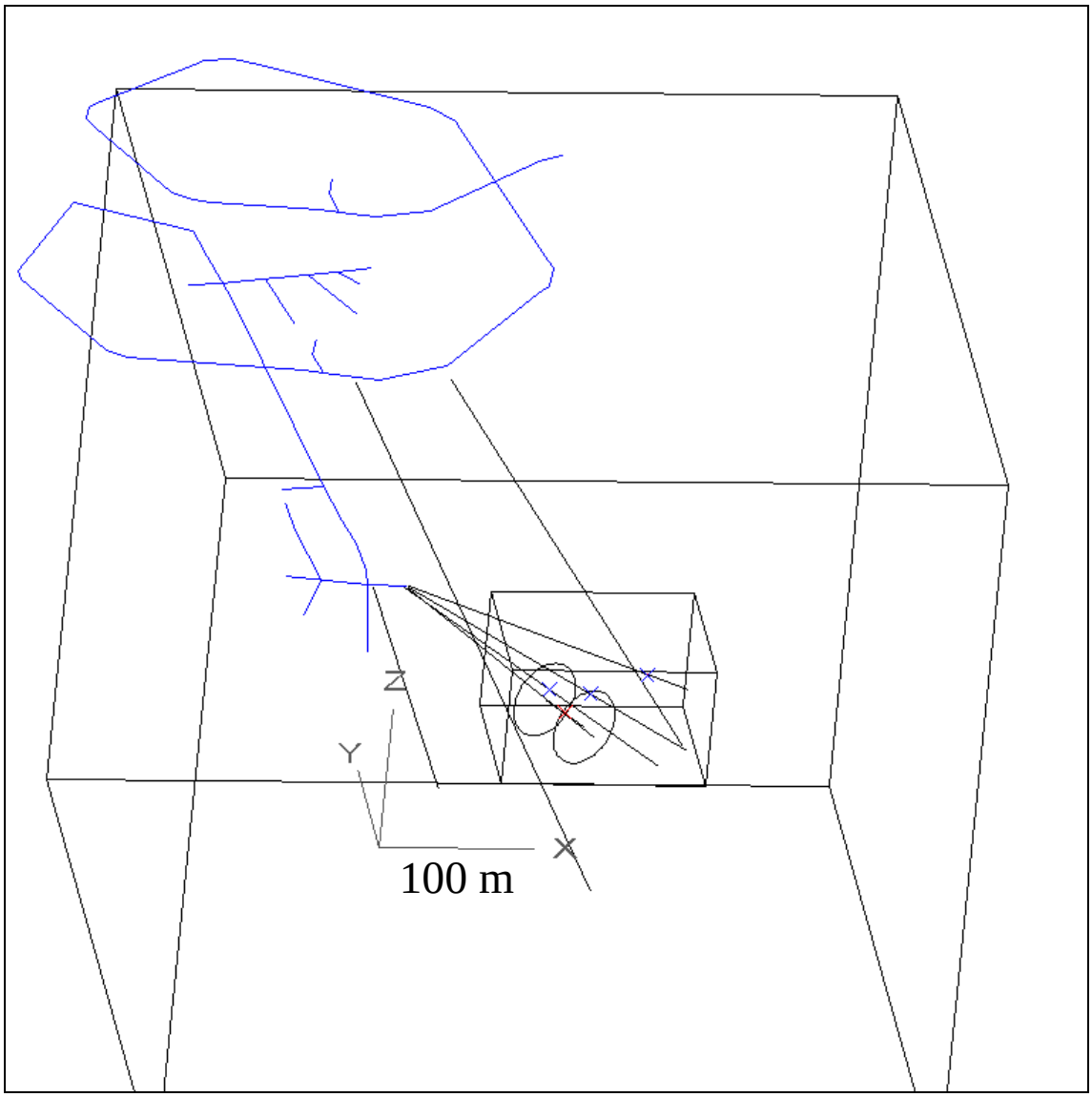

Figure 2-7: *Setup for CPT-4a test. View of the model domain with galleries, boreholes, cylindrical BG fracture generation domain, inner transport domain. X is Southing, Y is Easting, Z is upward.*

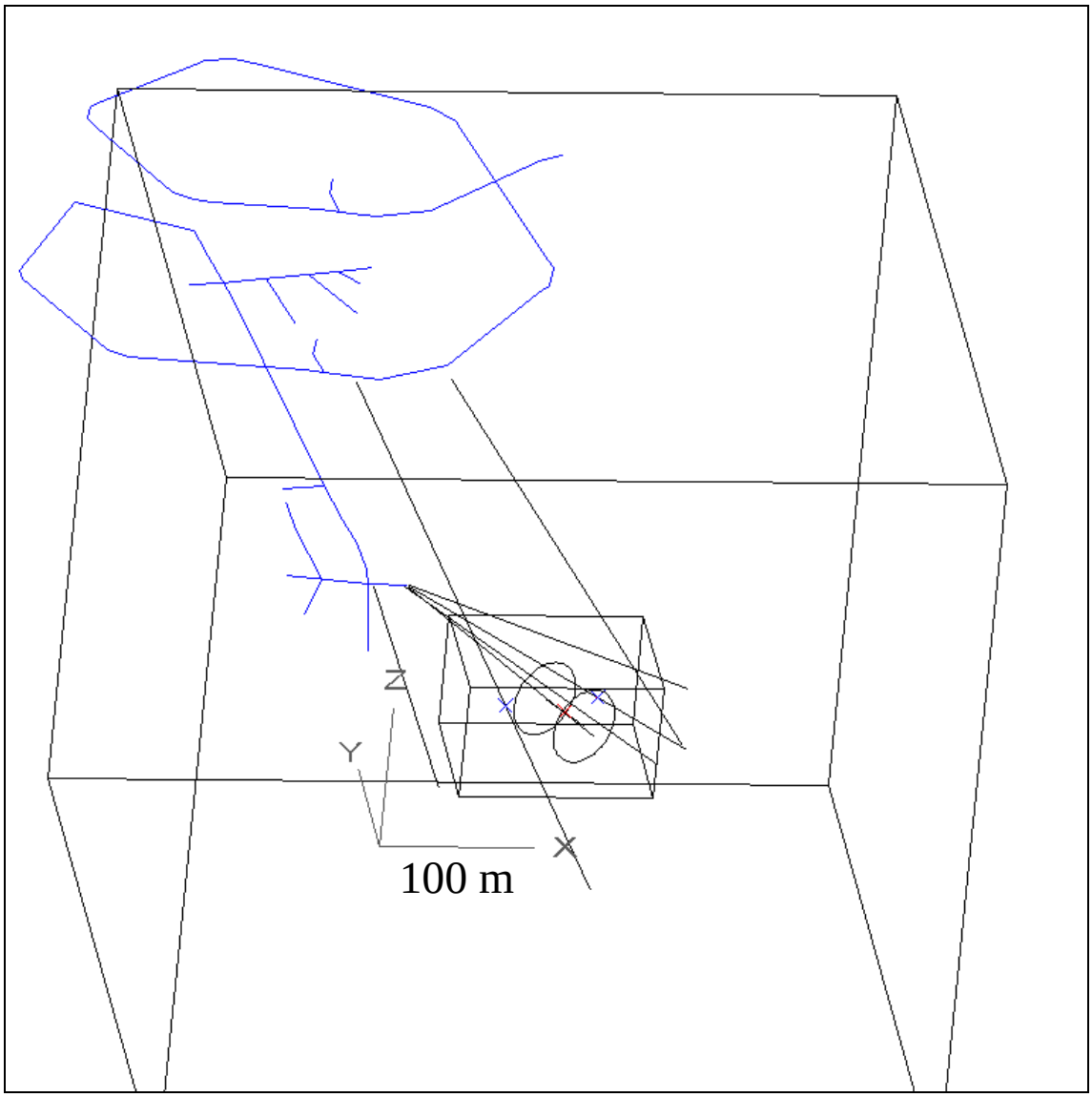

Figure 2-8: *Setup for CPT-4b test. View of the model domain with galleries, boreholes, cylindrical BG fracture generation domain, inner transport domain. X is Southing, Y is Easting, Z is upward. 100m long coordinate axes.*

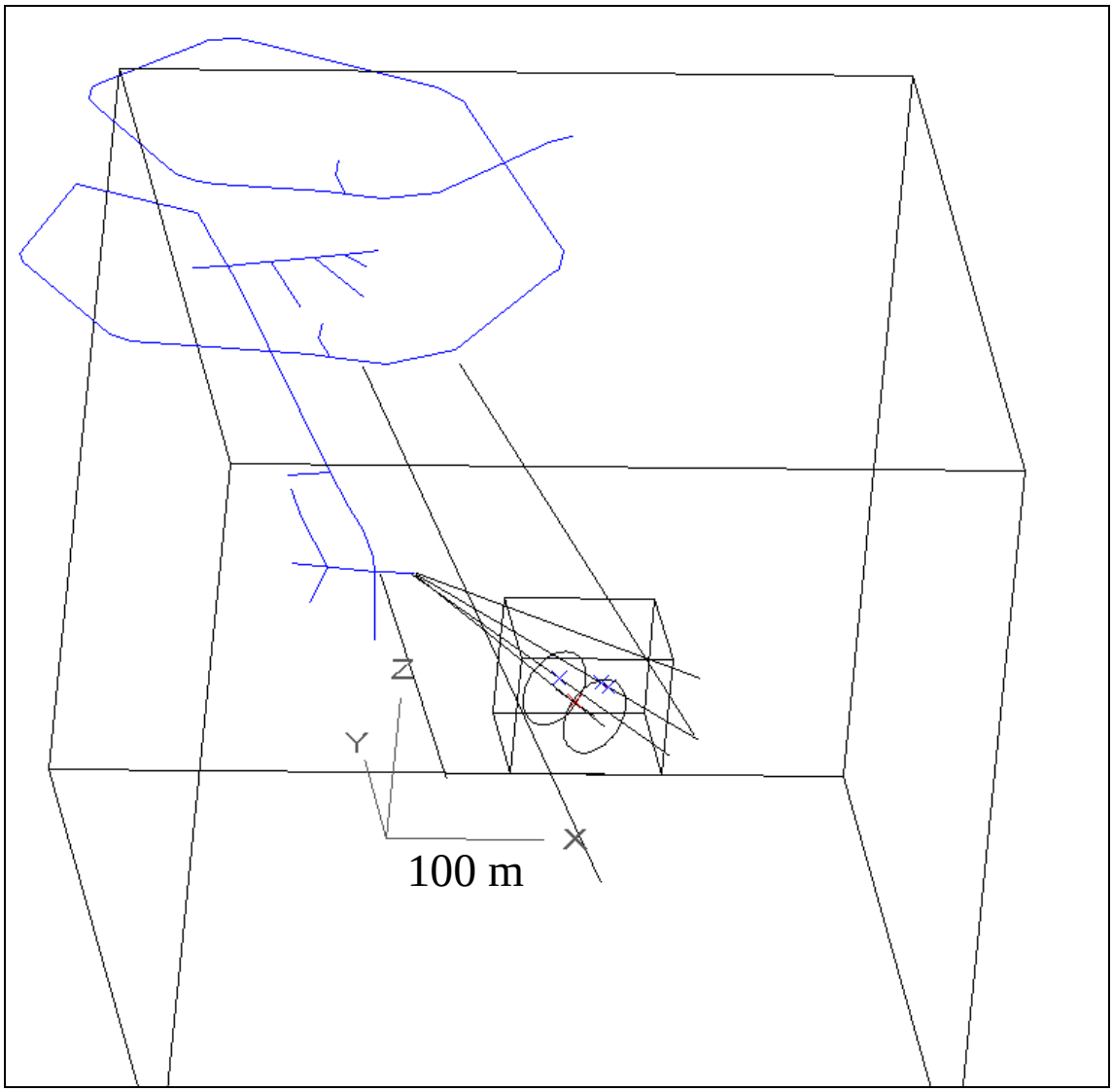

Figure 2-9: *Setup for CPT-4c test and BS2B tests. View of the model domain with galleries, boreholes, cylindrical BG fracture generation domain, inner transport domain. X is Southing, Y is Easting, Z is upward.*

2.3 The fracture network

In this section, the geometry and hydraulic material properties (transmissivity) of the deterministic structures and background fractures are outlined, followed by a description of transport properties.

The total flow network consists of the union of the deterministic structures, of the conditioned background fractures intersecting the boreholes, and of the "purely stochastic" ones. Channels are projected on all these features, then intersections between the various features are computed and stored. Such intersections are also considered as conductors, therefore permitting connection of the whole channel network. Any intersection between two features is assigned a conductivity taken from the distribution used for the most transmissive of the two features, and the corresponding section.

Except otherwise indicated, we use ten realizations (changing the seed of the pseudo-random number generator in the code) for each simulation we perform, and results are given in terms of the average and standard deviation of the response.

2.3.1 Deterministic structures

The following TRUE BS structures, #05, #06, #07, #10, #13, #19, #20, #21, #22, #23, #24 were included in the model. Their positions and properties were taken from [Dershowitz et al., 2003] and first used without any change. However, the extent of structures #05, #06 and #10 were then increased in the course of the project, since there is no indication that these structures should be truncated, and the extent given in Dershowitz et al. (2003) was arbitrary, and only meant to help plot readability. Table 2-1 gives the initial transmissivities used for the structures in the model. Note that all structures are considered homogeneous at large scales. In other words, we simulate only local variability, but no large scale trend, in the properties of any structure.

The two borehole intercepts denoted "BG1" and "BG2" are treated in the same manner as any other conditioned background fracture. Therefore, these two intercepts, respectively in boreholes KA0025F02 and KA0025F03, are represented by independent background fractures, which may or may not be connected depending on the realization.

Table 2-1: Transmissivity properties of structures, in m^2/s.

#05	**#06**	**#07**	**#10**	**#13**	**#19**
4.020E-07	1.910E-07	9.760E-08	2.980E-08	1.380E-08	1.020E-07
#20	**#21**	**#22**	**#23**	**#24**	
1.430E-07	6.020E-08	2.190E-08	1.660E-07	8.510E-08	

Flow paths within structures are represented by two superimposed square grids of channels [Rachez and Billaux, 2002], the second one oriented at 45 degrees from the first as shown in Figure 2-10. Using two grids greatly improves the accuracy of transport calculations in a large feature. We keep this for the hydraulic-only simulations in order to use consistent numerical models throughout the modelling. In the 500m model used for hydraulic computations, the spacing of the first square grid of channels is 15 m for all structures except structure #19, where it is 5m. The spacing of the second square grid of channels is then 15 m– respectively 5 m – divided by $\sqrt{2}$, i.e. about 10.6 m and 3.5 m. When building the inner model for transport simulations, we use a "first grid spacing" of 3 m for all structures except #19, and 1 m in Structure #19, which translate into a "second grid" spacing of 2.1 m and 0.71 m, respectively.

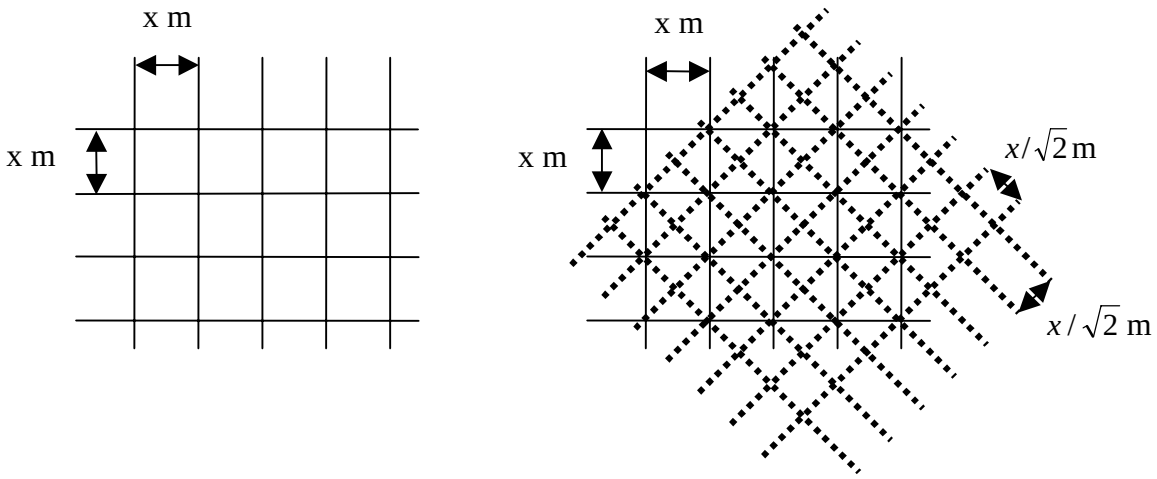

Figure 2-10 : *Two superimposed square grids of channels on each structure, after [Rachez and Billaux, 2002]*

Varying conductivities are generated for the channels in a given structure. The mean conductivity ***C*** is computed from the mean structure transmissivity ***T***, using the following equation:

$$C = T * \frac{g}{shapef}$$

Where:

> *g* is the grid size (length of the square edges), and
> *shapef* is a shape factor, with a value of "$1+\sqrt{2}$" for the "squares plus diagonals" grid that is used here (two superimposed square grids, with relative spacing 1 and $\sqrt{2}$ respectively).

It can easily be verified that the transmissivity – conductivity relationship above yields, for a homogeneous regular grid, flow properties equivalent to those of a *2d* continuum with transmissivity ***T.*** As an illustration, Figure 2-11 shows the log-conductivities obtained, in the initial 200 m – sided domain illustrated in Figure 2-2, when using *g* = 10 m for all structures. Figure 2-12 shows the same view, after increasing the model size to 500 m and extending several structures to the boundaries of the model, as mentioned above. Note that, even in the absence of any other physics in the model, the complete mixing condition at channel intersections produces significant dispersion at the network scale.

We assume at the start that within each structure, channel conductivity is distributed according to a truncated lognormal law, with a mean as given by Table 2-1 and the above equation, a coefficient of variation equal to 10%, and a minimum value equal to 1% of the mean. Values for Structure #19 are then changed during calibration. Note that the mean conductivity defined above does not yield the correct large scale structure transmissivity in the case of a broad distribution of the channel conductivities within the structure. Indeed, the mean conductivity required to obtain a given large scale transmissivity will be significantly higher if the standard deviation of the conductivities

increases. The transmissivity of such a network will not depend directly on the arithmetic mean of conductivities. In fact, if the number of conductors (channels) involved is large, the overall transmissivity depends on the geometric mean of the channel conductivities, which is much smaller than the arithmetic mean when standard deviation increases. For the initial standard deviation equal to 10% of the mean, we consider this negligible, and compute the average conductivity as explained above. However, when we broaden the distribution, we run a simple test to obtain the new "real" transmissivity corresponding to the fitted mean conductivity. We isolate the given structure by deleting all other conductors, and impose a unit gradient in it. Measuring the flows at its boundaries yields the transmissivity.

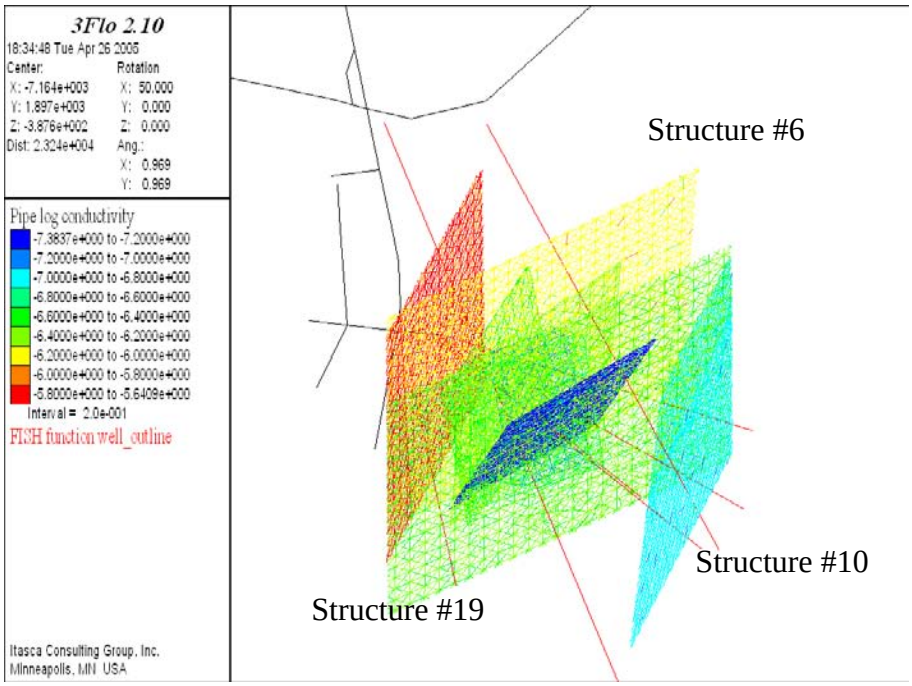

Figure 2-11: *Log-conductivities of the Structure channels in the initial model (200 m). View is due East, looking from above at a 50° angle. Tunnels in black and boreholes in red.*

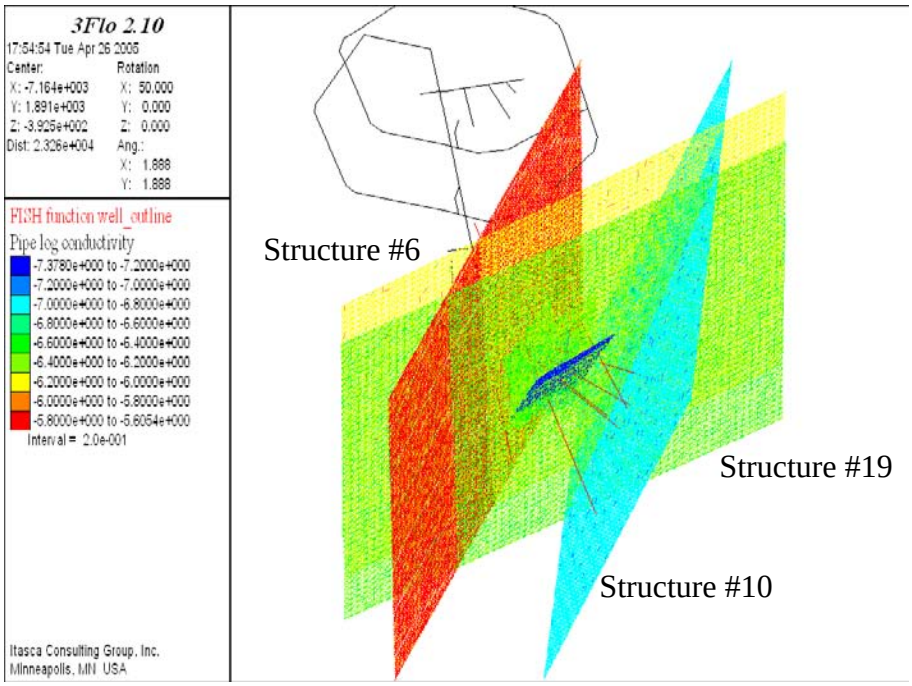

Figure 2-12: *Log-conductivities of the Structure channels in the extended model (500 m). View is due East, looking from above at a 50° angle. Tunnels in black and boreholes in red.*

2.3.2 Stochastic fractures

The "stochastic fractures" comprise all the "non structure" fractures included in the model, that is both fully stochastic and “conditioned to borehole” fractures. The stochastic fractures therefore correspond to the background fracture population.

Relevant available data are mainly expressed in terms of statistical representations. For instance over the TRUE Block Scale rock volume, the mean density of conductive background fractures has been estimated to be P_{32c}=0.29m^2/m^3 (Dershowitz et al., 2003). The distribution of the fractures in space is considered Poissonian and uses the above P_{32c} value. The fracture size distribution used is a power-law. The parameters of the power law are the scaling exponent a_{3d} and the minimum radius l_{min}. Here, we take a_{3d} = 3.8 and l_{min} = 3. The choice of the statistical models, as well as their parameters, are discussed in [Darcel, 2003].

Previous studies (Andersson et al., 2002, Dershowitz et al., 2003) have permitted building of models of fracture sets and corresponding orientation distributions for the background fractures (Table 2-2). These models are used to generate the orientations of stochastic fractures.

Known borehole intersections are all taken into account by conditioning the background fracture generation to these intersections, as discussed in [Darcel, 2003].

Table 2-2: Model of fracture set and orientation distribution deduced from TRUE Block Scale orientation estimations (from Andersson et al., 2002 (p125) and Dershowitz et al., 2003 (p 48).

Parameter	Basis	Set #1	Set#2
Orientation distribution	Two fitted sets	Fisher distribution Mean Pole (Trend, Plunge)=(211, 0.6) Fisher Dispersion κ=9.4	Fisher distribution Mean Pole (Trend, Plunge)=(250,54) Fisher Dispersion κ=3.8
intensity P_{32}		0.16 m^2/m^3 55.2% of fractures	0.13 m^2/m^3 44.8% of fractures

The transmissivity distribution of background fractures is deduced from the interpretation of flow rates measured by the Posiva flow logs. The derivation of the transmissivity distribution is performed by applying the radial flow equation to the flow in the Posiva flow log data (Andersson et al., 2002, p125). This leads to:

$$T = \frac{Q}{2\pi \cdot \Delta H} \cdot \ln\left(\frac{R}{r_w}\right) \sim \frac{Q}{\Delta H},$$

where Q is the flow rate and ΔH is the head drop. Posiva flow logs cover a range of measured flow rates going from 0.002 l/min to 5 l/min. This corresponds to a minimum transmissivity at $8 \times 10^{-11} m^2/s$ (with ΔH set to 410m, corresponding to the TRUE BS block depth).

A compilation of the flow logs performed in the boreholes of the TBS rock volume lead to a lognormal distribution for the transmissivity with a mean = -8.95 $\log_{10}(m^2/s)$ and a standard deviation of 0.93 $\log_{10}(m^2/s)$ (Table 3-1 in [Dershowitz et al., 2003]). Typically, conductive background fractures have a transmissivity between 10^{-11} and 10^{-9} m^2/s. Note that this unique transmissivity distribution is given for the two background fracture orientation sets defined in Table 2-2, just as was the case for the length distribution.

We assume no correlation between fracture transmissivity and fracture size (radius). Also, note that the lognormal transmissivity model we use excludes the transmissivity properties of deterministic structures. Finally, for the background fractures, flow paths are represented by a simple square grid, and channel conductivities are computed from the fracture transmissivity in the same way as for structures, as discussed in Section 2.3.1, using a factor *shapef* equal to 1. The grid spacing is 4 metres in the 500 m model, and is reduced to 0.8 m in the inner model.

2.3.3 Transport

The network properties for transport are illustrated in Figure 2-13. The following discussion applies to both types of features: either Structures or background fractures.

As discussed above, channel conductivities *C* are generated directly, in order to obtain the given large-scale feature transmissivity. We then use a simple geometrical conceptual model to describe the transport properties. A channel is considered as a flat ribbon, with width *w* and thickness *2b*. The width *w* can be deduced from the grid spacing *g* by consideration of the feature surface area. Supposing that flow covers the whole area, we need:

$$w = \frac{g}{2.shapef}$$

to obtain the correct total area. In fact, the flow area is not necessarily the same as the area of the feature: on one hand, the sides of the feature are in contact in some parts of the feature area, and/or filling may prevent flow in some other parts. On the other hand, the feature may be constituted of several sub-planes, in which case the flow area is actually larger than the feature area. We express this into a single parameter, which we call the "contact fraction" c_f (see Figure 2-13). The limiting value $c_f = 1$ means that the whole plane of the feature is in contact, and no area is left for flow, while $c_f = 0$ means that the area available for flow is equal to the area of the feature, and $c_f = -1$ corresponds to a feature made of two fully open sub-planes. Taking this parameter into account, we obtain:

$$w = \left(1 - c_f\right)\frac{g}{2.shapef}$$

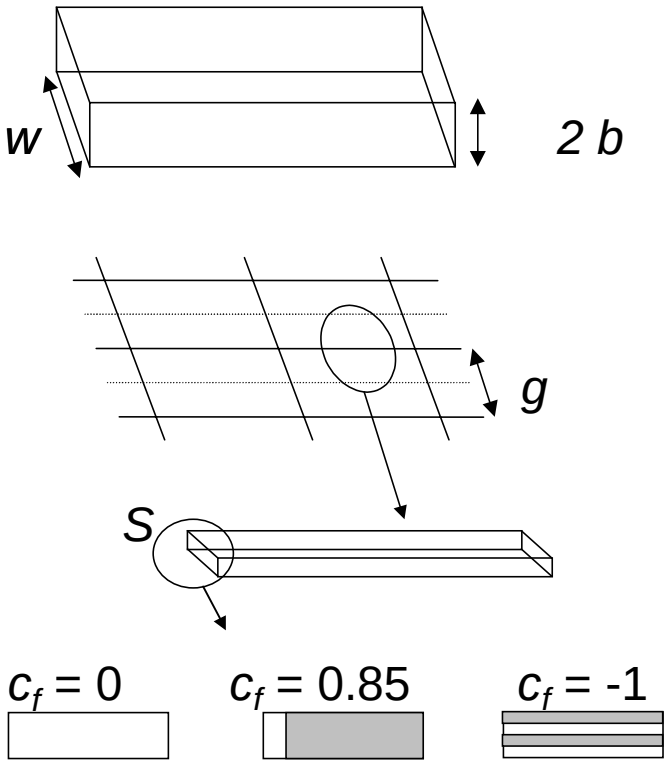

Figure 2-13: *Channel geometry for transport*

Once we know the width of a channel, we obtain its aperture *2b* in the following way. First, we note that the "local transmissivity" of this ribbon is *C/w*. We then use a square or cubic law for the variations of local transmissivity with aperture. This brings:

$$2b = \alpha\left(\frac{C}{w}\right)^{1/x}$$

where α is constant for all the channels in a structure, and *x* is 2 or 3. For $x = 3$ this equation is the translation of Poiseuille's law in the channel. For coefficient α, we start with the value $\alpha = 0.01$ for all the features. Note that α has a dimension $[L]^{(1-2/x)}\ [T]^{1/x}$. The dimension of α will therefore be $[L]^{1/3}\ [T]^{1/3}$ for x = 3, and $[T]^{1/2}$ for x = 2.

For a given channel grid (i.e. fixed *g* and *shapef*, given conductivity distribution), properties *x*, α and c_f completely describe the geometry of the system with regards to conservative as well as reactive transport. Their main respective effects can be described as follows:

- An increase in x decreases the variability of the apertures, therefore diminishing macro-dispersion effects. It also decreases the mean thickness of the channels, thus decreasing advective travel times.
- An increase in α increases the mean thickness of the channels, therefore increasing advective travel times.
- An increase in c_f reduces the width of the channels and increases their thickness, therefore diminishing the relative influence of surface exchanges (i.e. diffusion to the matrix and retention on the sides of the feature) versus advective mass transport. Also, the flow section is decreased, resulting in faster advective travel.

In addition to the above parameters, a non-reactive transport model may be completed by the choice of a longitudinal dispersion D_l representing the flow variability at the scale of the channels, i.e. below the length scale defined by the grid.

2.3.4 Intersection between borehole and feature

It is well known that for many features, not all the boreholes intersecting them show significant flow rates. This is due to the heterogeneity inherent to most hydraulic conductors, in which part of the area is either sealed or closed while most of the flow is carried by a limited portion of the area. However, when reproducing a test, we know that a given sink was chosen precisely because its intersection with a given feature is well defined and allows significant flow rates. Note that the actual behaviour of such intersections depends heavily on the diameter of the test well.

In the model, the connection between a borehole and a feature is handled in the following way. The code first detects the intersection between the borehole segment and a feature. Once the channels have been generated on all features, for each intersection, the node on the feature closest to the exact intersection point is obtained, and linked to a "borehole node" at the centre of the borehole section, by a very transmissive pipe with a very small section. In this way, any flow rate (either source or sink) imposed on the borehole node is transmitted to the features cutting it, with negligible head loss and travel time.

For tracer injection, two cases may occur, either injection of a Dirac or injection through a “tracer dilution” procedure. For the case of the Dirac, particles are simply added at the borehole node at time “t=0”, while the injection flow rate, if any, is imposed at this same node. For the other case of tracer dilution, a new pipe is connected to the borehole node and the injection flow rate is imposed at its other extremity. This pipe has a high transmissivity, and therefore does not contribute to head losses. However, its volume is equal to the circulating volume in the injection loop. The total mass of tracer is then emplaced in this pipe at time “t=0”, and particles are advected progressively out of this pipe. They are mixed at the end of every time step, to reproduce the continuous mixing occurring in the injection loop.

3 Analysis of in situ pre-tests (hydraulics)

3.1 Framework

In this part of the work, we reproduce the drawdowns for tests CPT-1 to CPT-3. We start with the initial parameters discussed in Chapter 2, then modify the transmissivity of Structure #19 and possibly the distribution of transmissivities of the background fractures. Also, because of the heterogeneity of Structure # 19, the actual steady-state drawdown at the pumping point for a given test is mostly representative of the local transmissivities around that point. To take this into account, we add a skin effect at each well section represented in the model. This skin effect influences only the near-pumping drawdown. It is obtained by multiplying the transmissivity of the channels directly connected to the well node (see section 2.3.4) by a given "skin factor". Note that a value of skin factor below one means head losses around the well, whereas a skin factor above one mimics a higher transmissivity area around the well.

3.2 Model specification

The model used here is based on the hydrostructural model that best fits the overall data available from the TRUE Block Scale Rock volume [Andersson et al., 2002] [Dershowitz et al., 2003]. Deterministic data are used to place the structures and to condition the background fracture field to known intersections with boreholes. The geometrical statistical properties of the general fracture network model are taken from the analyses presented in [Darcel 2003]. The next sub-sections detail the model specifications for the three test configurations.

3.2.1 Interference test configuration

The three configurations CPT-1, CPT-2 and CPT-3 correspond to pumping in the three boreholes intersecting Structure #19 (see Figure 2-3, Figure 2-5, and Figure 2-6). Table 3-1, Table 3-2, and Table 3-3 specify the pumping section, as well as the observation sections, for each of the three tests. For each section, we give the structure, if any, probed by the section, as well as the Euclidian distance from the pumping section.

Table 3-1: Pumping and observation sections for test CPT-1

#	Borehole	Section	Structure	Distance (m)
1	KA2563A	S1	#19	118
2	KI0023B	P2	#19	83
3	KI0025F02	R5	#13 & #21	80
4	KI0025F02	R3	#19	48
5	KI0025F02	R2	BG	45
6	KI0025F03	R3	#19	68
7	KI0025F03	R2	BG	66
8	KI0025F	R2	#19	pumping

Table 3-2: Pumping and observation sections for test CPT-2

#	Borehole	Section	Structure	Distance (m)
1	KA2563A	S1	#19	70
2	KI0023B	P2	#19	37
3	KI0025F	R2	#19	48
4	KI0025F02	R5	#13 & #21	41
5	KI0025F02	R2	BG	5
6	KI0025F03	R5	#13	49
7	KI0025F03	R3	#19	21
8	KI0025F03	R2	BG	20
9	KI0025F02	R3	#19	pumping

Table 3-3: Pumping and observation sections for test CPT-3

#	Borehole	Section	Structure	Distance (m)
1	KA2563A	S1	#19	54
2	KI0023B	P2	#19	27
3	KI0025F	R2	#19	68
4	KI0025F02	R5	#13 & #21	37
5	KI0025F02	R3	#19	21
6	KI0025F02	R2	BG	24
7	KI0025F03	R5	#13	39
8	KI0025F03	R2	BG	7
9	KI0025F03	R3	#19	pumping

3.2.2 Flow properties

The transmissivity and small scale heterogeneity of Structure #19 are the main fitting parameters. We start with a mean transmissivity as given in Table 2-2, and a lognormal distribution of channel conductivities with coefficient of variation equal to 10%. Also, all skin factors are set to one initially.

3.3 Numerical simulations

3.3.1 Initial results

The drawdowns for the three tests are shown in Figure 3-1, Figure 3-2 and Figure 3-3. In each figure, we represent the measured and simulated drawdown versus distance from the pumping well. For each measurement/simulation point, we indicate in what feature the point is located. Also, a bar code represents the standard deviation of the values obtained for the 10 realizations of the simulation.

All the drawdowns are overestimated, indicating an underestimation of the transmissivity of Structure #19. Also, by analysing the head difference at small distances from the pumping well, i.e. between the value at the pumping well and the measurement point closest to the well, we can see that the head gradient at the origin is overestimated for test CPT-1, and underestimated for tests CPT-2 and CPT-3 (compare the slope of the curve from the origin and the overall slope, when taking only points far from the origin). This means we underestimate the transmissivity area around KI0025F (pumping well for test CPT-1), and conversely overestimate the transmissivity around the pumping wells for CPT-2 and CPT-3, i.e. KI0025F02 and KI0025F03. Note that these observations are consistent with the flow dimension analyses previously performed on the tests responses, which concluded on the presence of high transmissivities around well KI0025F and low transmissivities around well KI0025F03.

Drawdowns at observation points situated in Structures #13 and #21 are found much lower than the drawdowns in Structure #19. This reflects the less transmissive connection to these points. The observation points in background fractures (denoted by "BG" in the figures), do not show a behaviour significantly different from the Structure #19 points, either in the in situ tests or in the simulations. This may indicate that these points are not well linked to the boundaries, except through Structure #19, which is the structure closest to them.

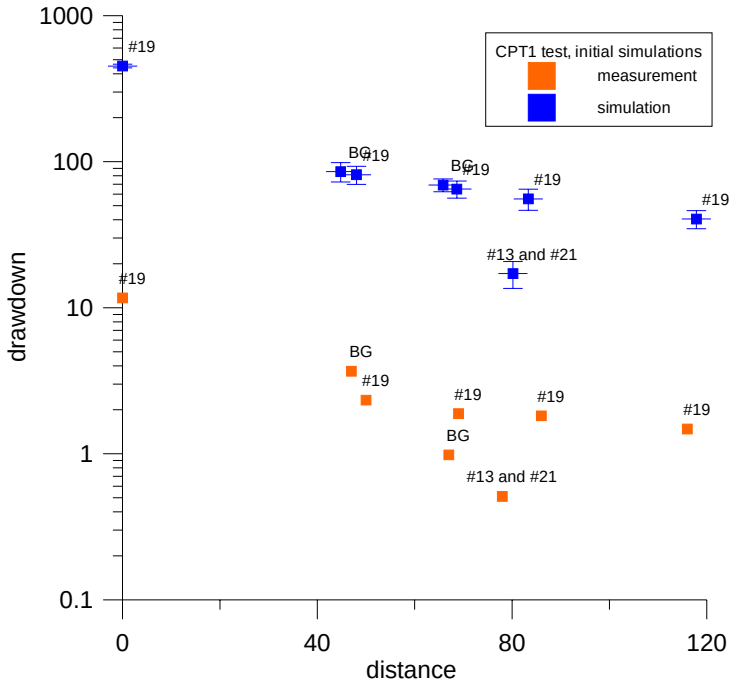

Figure 3-1: *CPT-1 test. Drawdown vs. distance. Initial simulations. Bar codes show the standard deviation for ten realizations.*

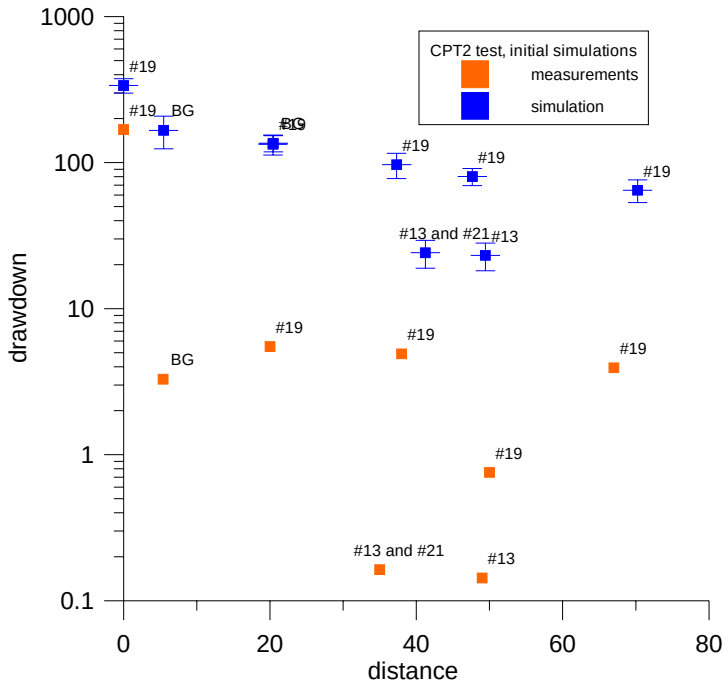

Figure 3-2: *CPT-2 test. Drawdown vs. distance. Initial simulations. Bar codes show the standard deviation for ten realizations.*

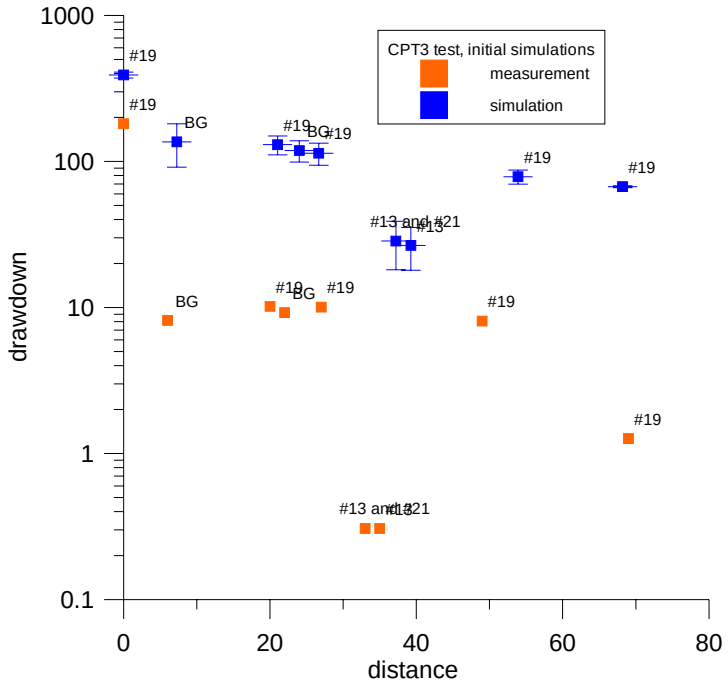

Figure 3-3: *CPT-3 test. Drawdown vs. distance. Initial simulations. Bar codes show the standard deviation for ten realizations.*

3.3.2 Results after calibration, discussion

In view of the results shown in Section 3.3.1, we make the following changes in the model parameters: a skin factor of ten is used for borehole KI0025F, section R2 (CPT-1 pumping section, with high conductivity), while skin factors of 0.03 and 0.025 are used for boreholes KI0025F2 (CPT-2 pumping section) and KI0025F3 (CPT-3 pumping section), respectively. Also, the mean transmissivity of Structure #19 is increased from the initial value of 10^{-7} m^2/s to $4\ 10^{-7}$ m^2/s. Note that the initial value is the one recommended by [Dershowitz et al., 2003]. In fact, [Anderson et al., 2002] show measured values ranging from $9\ 10^{-8}$ m^2/s to $3\ 10^{-5}$ m^2/s.

The need to use widely different skin factors to account for near-borehole effects in Structure #19 hints at a large variability of its transmissivity. We therefore also force a high heterogeneity by imposing a coefficient of variation of 2 (as well as a minimum value equal to 1% of the mean) for the lognormal distribution of channel conductivities in Structure #19. Note that when increasing the coefficient of variation of the channel conductivities, we also need to increase the mean in order to keep the large-scale transmissivity of Structure #19 constant.

The new drawdowns we obtain are shown in Figure 3-4 through Figure 3-6. The agreement with experiments is better than previously, although far from perfect. If we look at the responses within Structure #19, we observe that the gradients we produce are a bit smaller in test CPT-1, quite close to that of the experiment for test CPT-2, and somewhat larger for test CPT-3 (except an outlying measurement at 68m, corresponding to the KI0025F intersection). This fits well with our current understanding of Structure #19, with a trend from a simple feature of lower conductivity in the north west, to a more complex feature of higher conductivity in the southeast. In order to reproduce such a trend, we would need to consider that Structure #19 is heterogeneous at larger scales. However, we chose to keep our model simple and use the same mean transmissivity for Structure #19 throughout.

We tested the influence of a change in background fractures properties on the observed drawdowns. It turns out, as can be expected, that the results are controlled by the properties of Structure #19. Even drawdowns in BG1 are not significantly different if this fracture and other background fractures are made more or less transmissive.

Variability from realisation to realisation is not large for the initial simulations, and is even smaller for the final calibrated networks, despite the very high variability of the channel conductivities: once the skin effect at each pumping well is taken into account, the interference tests mostly “see” the large scale transmissivity and the boundary conditions, which do not change from one realization to another.

In summary, drawdowns in Structure #19 and its vicinity are dominated by the properties of the structure itself. Also, because of the large amount of deterministic information already present in the model, variations due to its stochastic nature are fairly small - the model is well constrained for hydraulics.

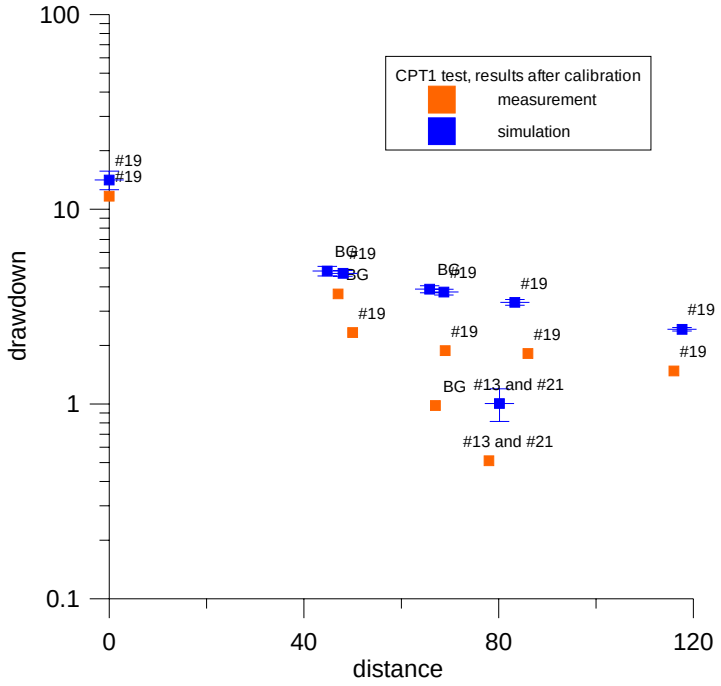

Figure 3-4: *CPT-1 test, Drawdown vs. distance. After calibration. Bar codes show the standard deviation for ten realizations.*

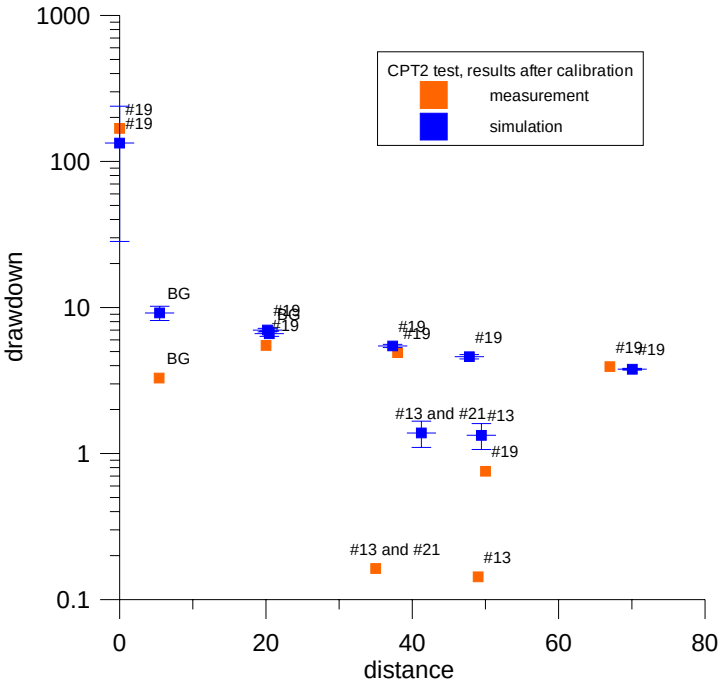

Figure 3-5: *CPT-2 test. Drawdown vs. distance. After calibration. Bar codes show the standard deviation for ten realizations.*

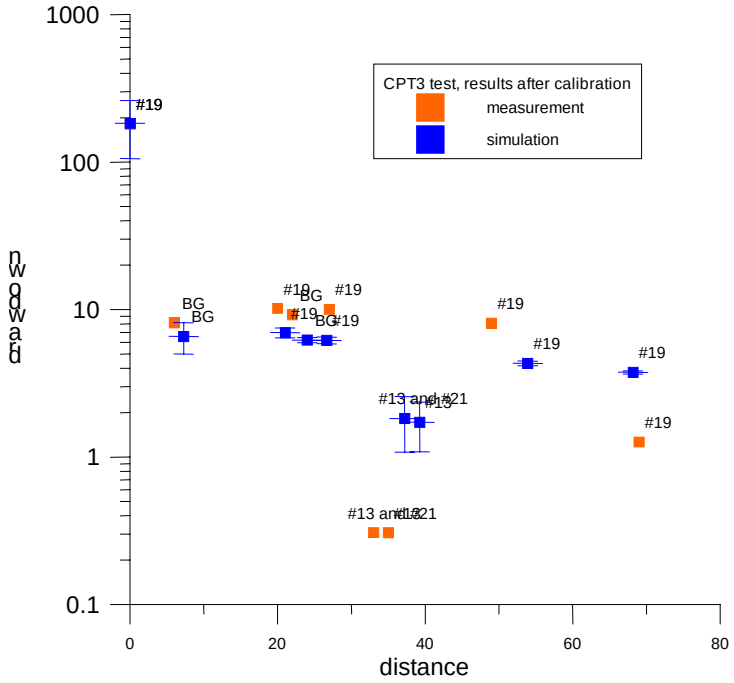

Figure 3-6: *CPT-3 test. Drawdown vs. distance. After calibration. Bar codes show the standard deviation for ten realizations.*

4 Predictions of in-situ sorbing tracer tests

4.1 Calibration of non-reactive transport properties

4.1.1 Test configuration and initial properties

The calibration was based on the CPT-4a, CPT-4b and CPT-4c tests (Andersson et al., 2004). Table 4-1 specifies the injection and pumping sections for each of the three tests. For each section, we give the structure, if any, intercepted by the section, as well as the Euclidian distance to the pumping section.

Table 4-1: Injection and pumping sections for tests CPT-4a, CPT-4b and CPT-4c

#	Borehole	Section	Structure / fracture	Distance (m)
CPT-4a				
1	KI0023B	P2	#19	27
2	KI0025F	R2	#19	68
3	KI0025F02	R3	#19	21
4	KI0025F03	R3	#19	pumping
CPT-4b				
1	KA2563A	S1	#19	54
2	KI0025F02	R2	BG 1	24
3	KI0025F03	R3	#19	pumping
CPT-4c				
1	KI0023B	P2	#19	27
2	KI0025F02	R3	#19	21
3	KI0025F02	R2	BG 1	24
4	KI0025F03	R3	#19	pumping

We start the simulations with a quite simple model for transport. We use the Poiseuille law exponent (i.e. the inverse of the exponent x is 3). The aperture coefficient α (see Section 2.3.3) is equal to 0.01 $m^{1/3}$ $s^{1/3}$ for both deterministic structures and background fractures, and the whole area of structures and background fractures is available to flow, with a contact fraction c_f equal to zero. The longitudinal dispersivity D_l in the channels is set to zero, both in structures and in background fractures. No diffusion is taken into account: matrix effective diffusivity D_m is also zero. In short, our initial model has no dispersion except the one produced by mixing at intersections (and enhanced by the large variability of channel conductivities in structures), it has no diffusion into the matrix, and flow paths occupy the whole area of all features. No initial distinction is made between the transport/retention properties of structures and background fractures. In this way, differences between structure and background fracture properties will arise from the calibration, not from *a priori* distinctions.

Our parameter space for calibration is then composed of the following parameters, both for deterministic structures and background fractures:

- Aperture exponent: x,
- Aperture coefficient: α,
- Contact fraction: c_f,
- Longitudinal dispersivity: D_l,
- Matrix effective diffusivity: D_e

During the course of the calibration, in order to keep the number of fitting parameters as low as possible, we do not distinguish between structures and background fractures for the values of the aperture exponent x and of the matrix effective diffusivity D_e. Conversely, aperture coefficients, contact fractions and longitudinal dispersivities are allowed to differ between structures and background fractures. Also, we allow the transmissivity of the BG 1 intercept to vary. Our goal here is to reproduce all test results with a unique set of parameters. Note that among the calibrated parameters, D_e is the only one that will not be used directly later for predicting reactive tracer tests. The effective diffusivities of the various radioactive tracers will be taken instead, as provided by the project.

4.1.2 Initial results

Figure 4-1 to Figure 4-3 show the results obtained with the initial parameters, for 10 realizations. All simulated travel paths are much too fast, with peak arrival times under predicted by a factor 5 to 25, and with consequently too large concentrations in all cases.

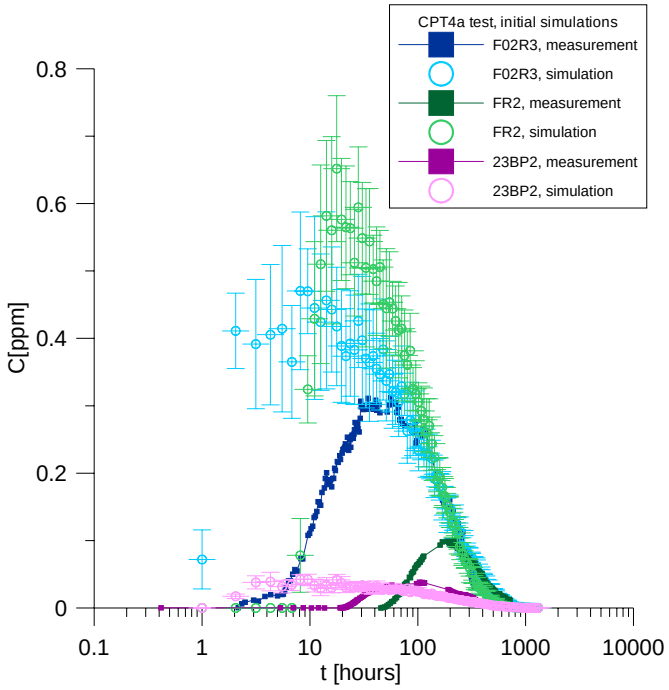

Figure 4-1: *CPT-4a test. Breakthrough curves for initial simulations. Bar codes show the standard deviation for ten realizations.*

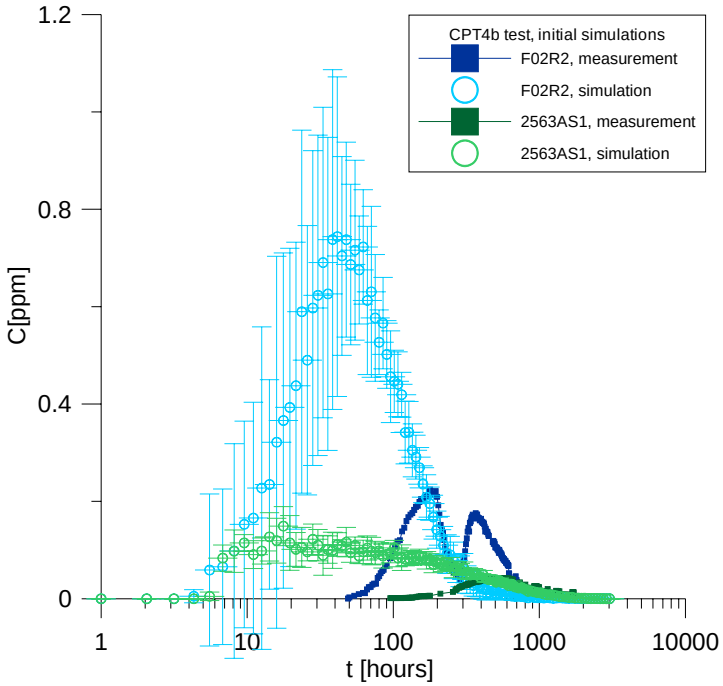

Figure 4-2: *CPT-4b test. Breakthrough curves for initial simulations. Bar codes show the standard deviation for ten realizations.*

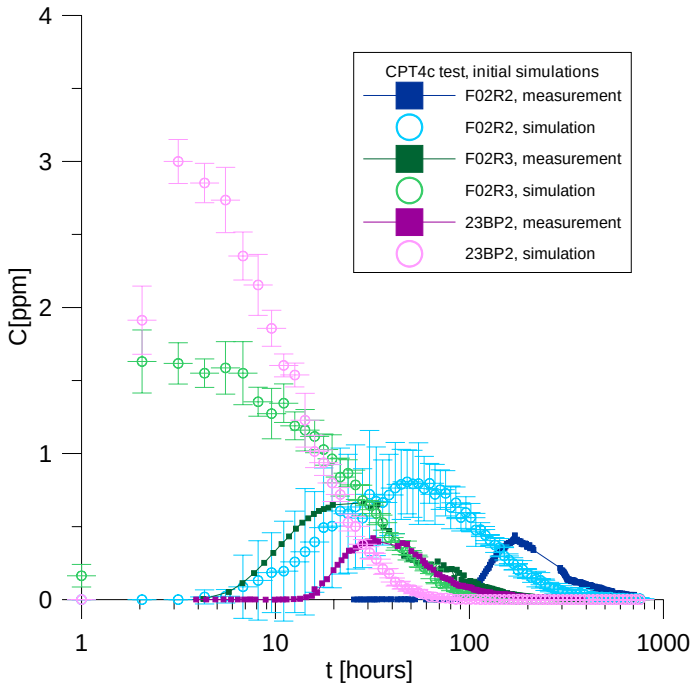

Figure 4-3: *CPT-4c test. Breakthrough curves for initial simulations. Bar codes show the standard deviation for ten realizations.*

4.1.3 Calibration, and results after fitting

We first note that all tracers will travel for some part of their path in Structure #19, since the sink is situated in it. Tracers injected in Structure #19 are likely to have almost all their travel paths in this structure, while the ones injected in BG 1 will travel both in background fractures and in Structure #19. This means that we can calibrate first the properties of Structure #19, using all the tracers injected in it. We are then able to calibrate the background fracture properties, keeping the values for Structure #19 constant.

Calibration of the Structure #19 parameters is based on the six breakthrough curves obtained in the structure: the three breakthrough curves from CPT-4a, the injection in borehole KA2563A for test CPT-4b, and injections in boreholes KI0023B and KI0025F02 for test CPT-4c. These six curves represent four different paths. We calibrate properties in order to reproduce these breakthrough curves using the same ten realizations of the network as before, and looking at the mean curves produced by these ten realizations. Calibration is by trial and error. The main steps in this trial and error process are outlined in the following paragraphs.

We first change the (transmissivity versus aperture) law in the structures, in order to get more realistic first arrivals. When first changing the aperture coefficient α only, and keeping $x = 3$, we obtain proper time scales but too sharp breakthrough curves. We therefore chose to change the aperture exponent x to 2, producing a more variable aperture field. We then need a much larger α, as indicated in Section 2.3.3. The value for structures that produces realistic time frames is 0.25 $s^{1/2}$. However, while attempting to reproduce the various breakthrough curves, we note that the curves we obtain are still too sharp. Changing the longitudinal dispersivity D_l in the structure channels to 1 m produces better first arrivals, but cannot reproduce the late time shapes: we need to introduce some diffusion into the matrix in order to obtain these shapes. We chose a medium effective diffusivity, $D_e = 5\ 10^{-11}$ m^2/s. We then need to specify a fairly large exchange surface for diffusion from structures in order to obtain the observed retardation: the contact fraction c_f is set to –1, which corresponds to a "doubled" exchange surface (see Figure 2-13).

Once the properties of Structure #19 are calibrated, we turn to the background fracture properties. Note that here, we have only two tests, on the same path, and using fairly similar boundary conditions (pumping and injection rates are almost identical). We find out that using the mean response from ten realizations cannot work: because breakthrough curves are widely different from one realization to another, the average response is too "dispersed": looking at the mean response simply cannot reproduce the "sharp" behaviour of the actual system. We then chose to work on only one realization of the network. This realization is chosen "at random". It is simply the first of the 10 realizations we had been working with.

We find that by simply adjusting the aperture coefficient α to 0.06 $s^{1/2}$, we are able to reproduce the CPT-4c curve fairly well. Any attempt to obtain a better fit for the CPT-4b test then results in worsening the fit for CPT-4c. Note that we keep the contact fraction at zero, implying the exchange surface corresponds to simple "single" joints, with only little area excluded to flow.

The final calibrated transport properties are summarized below.

Aperture exponent x:	2
Aperture coefficient α in structures:	0.25 $s^{1/2}$
Aperture coefficient α in background fractures:	0.06 $s^{1/2}$
Contact fraction c_f in structures:	-1
Contact fraction c_f in background fractures:	0
Dispersivity D_l in structures:	1 m
Dispersivity D_l in background fractures:	0 m
Matrix effective diffusivity D_e:	5 10^{-11} m^2/s

Figure 4-4, Figure 4-5 and Figure 4-6 show the breakthrough curves we obtain after calibration, for the selected single realization. For the two paths that will be used for the later BS2B tests, the calibrated model produces responses similar, if not identical, to the experimental measurements.

Injections in Structure #19 from KI0025F02, section R3 (tests CPT-4a and CPT-4c) yield simulated breakthrough curves with slightly too late first arrivals. Injections in BG 1 from KI0025F02, section R2 (tests CPT-4b and CPT-4c) produce a well fitted curve for test CPT-4c, but do not reproduce the tail of the response for test CPT-4b, as mentioned above.

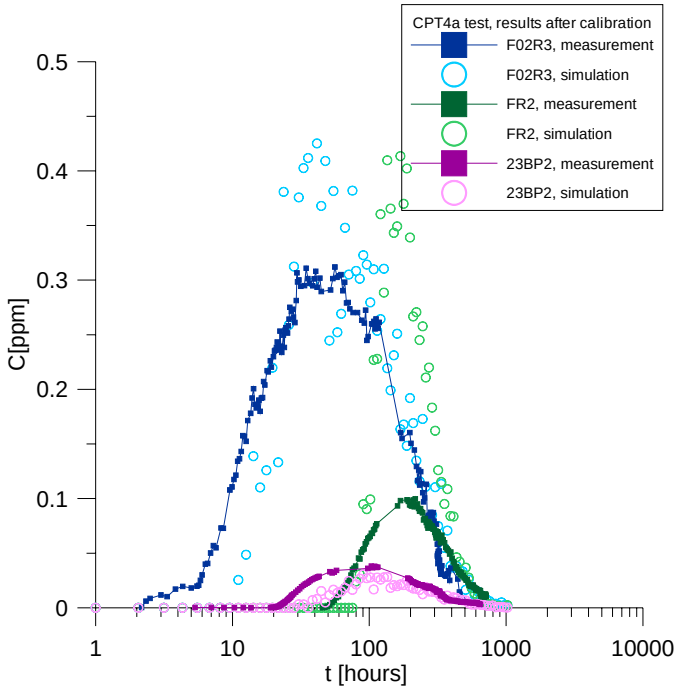

Figure 4-4: *CPT-4a test simulations. Breakthrough curves after calibration. One realization.*

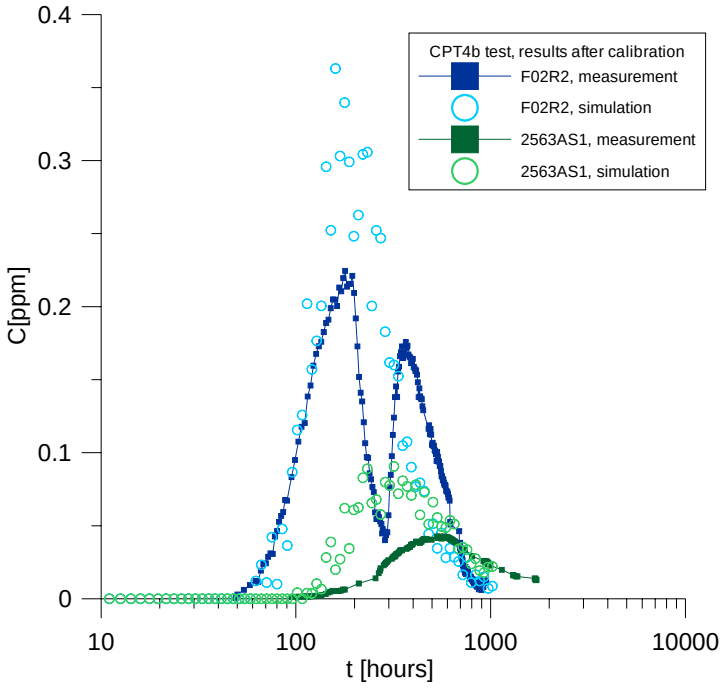

Figure 4-5: *CPT-4b test simulations. Breakthrough curves after calibration. One realization.*

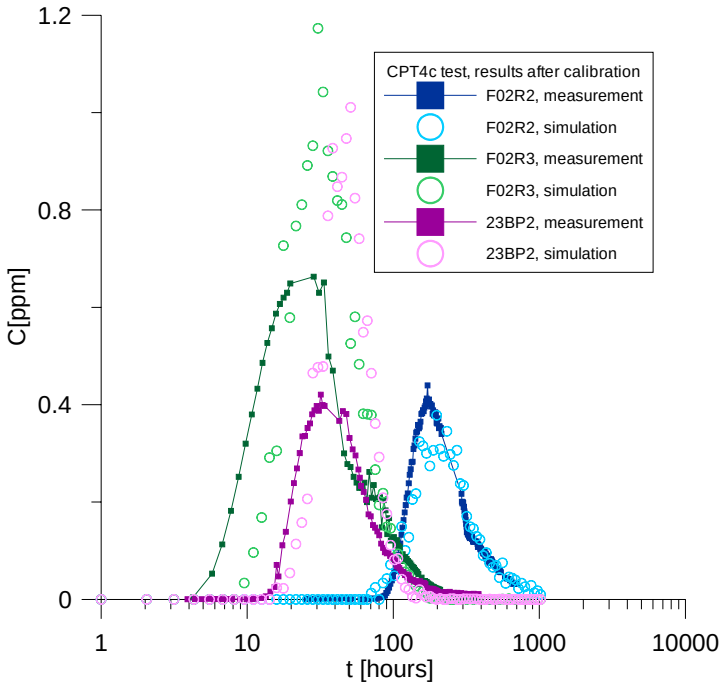

Figure 4-6: *CPT-4c test simulations. Breakthrough curves after calibration. One realization.*

Figure 4-7 shows the average breakthrough curves we obtain for ten realizations, as well as the standard deviation of the response for each time interval. The curves for injections into Structure #19 (i.e. all curves except the injections in borehole KI0025F02, section R2, tests CPT-4b and CPT-4c), are almost identical, if only a little smoother, to the ones in Figure 4-4 to Figure 4-6. When dealing with transport within a structure, results do not depend much on the realization. On the other hand, results for injection in BG 1 are quite different, and show the highest variability, as already mentioned above. We may explain the low variability of the curves for Structure #19 response by an averaging over the path length: "the path is long enough that variations in properties are averaged over it, therefore various realizations see the same averaged behaviour, over similar path lengths, and do not differ markedly from each other". However, the Euclidian distance from injection to pumping for the KI0025F02, section R2 injection in BG1 is similar (24 m) to other injection / pumping distances. In fact, compared to the perfectly connected structure where the actual path length is likely to be similar to the Euclidian distance, the background fracture path is likely to be much longer than its Euclidian "length". Here, averaging along the path "does not work", simply because connectivity plays a major role, with path lengths that may vary quite a lot from a realization to another.

In summary, we can draw the following tentative conclusions from the calibration of structure and background fracture transport properties based on tests CPT-4a to CPT-4c:

- We need to introduce very heterogeneous structures, with a fairly large flow wetted surface;
- The background fracture properties we obtain are those of simpler features: less wetted surface per fracture area, smaller apertures for a given transmissivity;
- Diffusion is needed to properly account for the experimental results;
- Structure (#19) response for one realization is already "averaged", there is no major difference between single-realization and multiple-realization-averaged breakthrough curves;
- Background fracture response varies widely between realizations. Breakthrough curves averaged over realizations then have little meaning, because of the wide range of variations in the potential actual response.

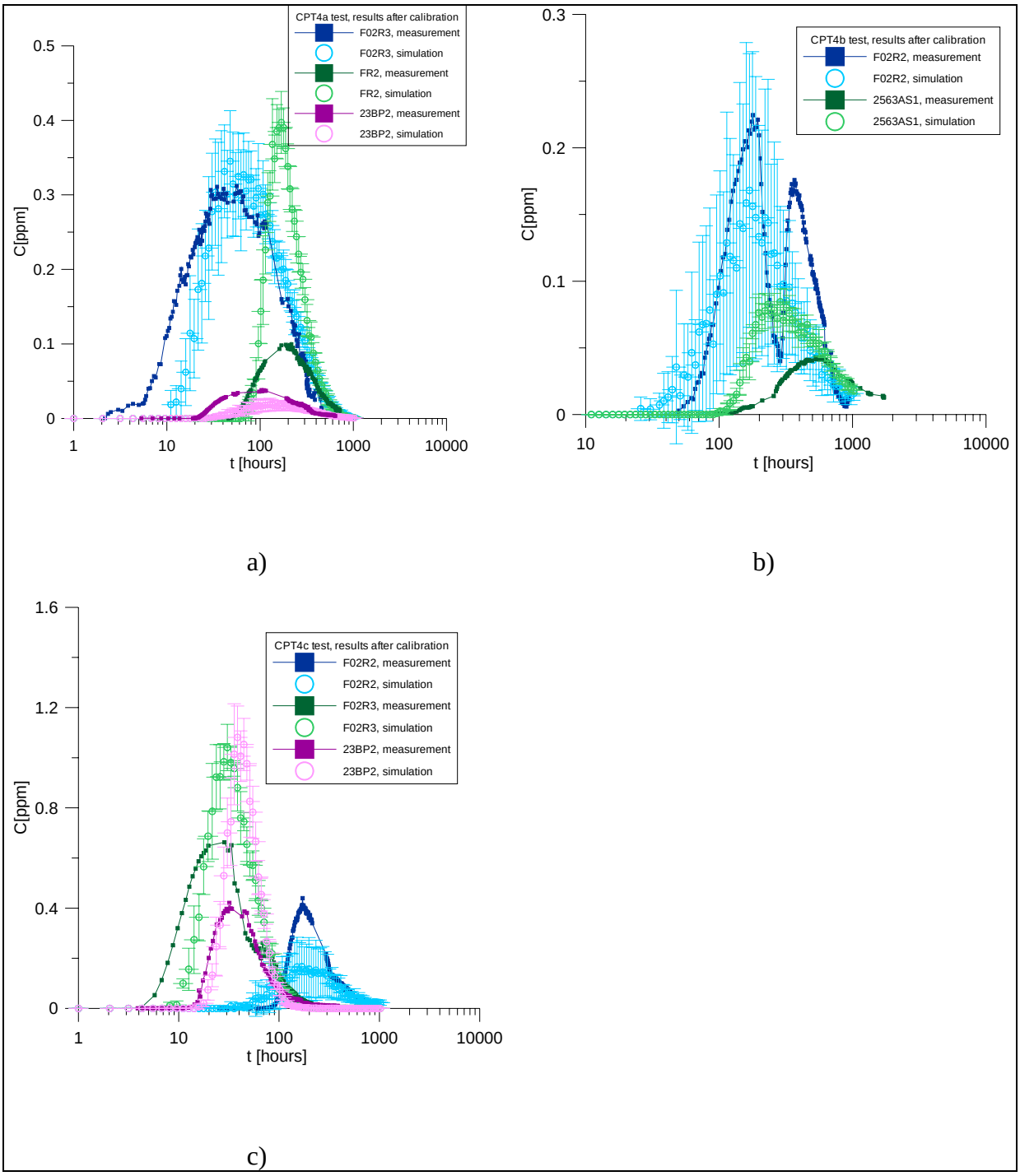

Figure 4-7: *CPT-4a to CPT-4c tests. Breakthrough curves for ten realizations after calibration. Bar codes show the standard deviation.*

4.2 Prediction of reactive tracer tests

4.2.1 Choice of properties

The transport and retention model is discussed in detail in Section 2.3. Each channel in our flow network can be in contact with one surface retention material and with one matrix type in which tracer may diffuse and be adsorbed. The immobile pore space thickness is considered infinite. This is obviously quite simple compared to the conceptual model that has been progressively put together during the course of the TRUE project, where:

1. the sides of the fracture are often lined with two or more layers of materials with finite thicknesses and contrasted properties;
2. fault gouge may be present in the fracture, while another material lines its sides, therefore providing two contrasted diffusion domains next to a given flow path, while multiplying the perimeter of the flowing section, with diffusion enabled simultaneously into the sides of the fractures and into “in fracture” fault gouge.

We cannot reproduce the layered nature of the fracture sides. However, we assign one material to every channel in the model. For a given type of feature, (i.e. structure, or background fracture), we distribute the various immobile pore spaces between the channels according to the areas we assume they occupy in this feature type.

We base the sorption, porosity and diffusivity properties in our model on the values provided by Byegård and Tullborg (2004).

The amount of fault gouge present in Structure #19 cannot be measured directly. Fault gouge was found only in KI0025F02. For the prediction, we chose to consider the presence of only a minimal amount of fault gouge, with 5% of the area of Structure #19 concerned. The remainder of the area of Structure #19 is divided between ”Cataclasite / Mylonite”, covering 20% of the area of the Structure, and hydrothermally ”Altered Diorite”, covering the remaining 75%. We will see later that the assumption on the amount of gouge in the Structure has a large influence on the results.

For background fractures, Byegård and Tullborg (2004) propose filling properties identical to the fault gouge properties, and consider that background fracture wall rock consist mostly of Altered Diorite. We follow these assumptions. We chose to consider that only 5% of the flow area is in contact with fracture filling, while the remainder is in contact with the wall rock, i.e. Altered Diorite. Note that the two ”BG fractures” sets of properties below are effectively used for all background fractures, not only BG 1.

The assumptions above are summarized in Table 4-2, together with porosities directly taken from the Data Delivery # 5, and assuming an average rock density of 2500 kg/m^3. Simple material names (column “Name” in the table) are assigned for use in the model input tables. They are indicated in Table 4-2, and then used, for simplicity in Table 4-3 detailing reactive properties.

Table 4-2 : Immobile pore space as realized in the model

	Name	Fraction of area	Porosity	Density kg/m^3
BG fractures				
Fracture filling	bg_fil	0.05	0.05	2500
Altered diorite	Bg_rim	0.95	0.006	2500
Structure 19				
Gouge filling	19_gou	0.05	0.20	2500
Cataclasite/Mylonite	19_cat	0.20	0.01	2500
Altered diorite	19_dio	0.75	0.006	2500

Diffusivities, Ka's and Kd's are taken directly from the values given, when available. However, sorption properties for a given tracer are given only for the feature in which it is injected. We need in fact a slightly more general model. Tracer injected in BG 1 has to travel through Structure # 19 too before it reaches the sink located in Structure # 19, and, less importantly, tracer injected in Structure # 19 may travel some part of its path in the background fractures intersecting the structure. Therefore, sorption properties must be specified for each tracer and for each type of immobile pore space. To complete the matrix of parameters, as given in Table 4-3, we use the following simple rules:

- For tracers I, tbDTPA, HTO, and EuDTPA, all Ka's and Kd's values are null.
- Background fracture filling Kd's for Sr, Rb and Cs are the same as fault gouge Kd's for these tracers.
- Background fracture rim altered Diorite Ka's and Kd's for Sr, Rb and Cs are the same as those in Structure 19 rim altered Diorite.
- Fault gouge Kd's for Na, Ba and Mn are the same as background fracture filling Kd's for these tracers.
- Cataclasite Ka's and Kd's for Na, Ba and Mn are the same as altered rock Ka's and Kd's for these tracers.
- Structure rim altered Diorite Ka's and Kd's for Na, Ba and Mn are the same as those for background fracture rim altered Diorite.

Note that these rules are arbitrary. They are based on the concept that 1) background fracture filling and fault gouge may have similar properties, and that altered Diorite close to a background fracture is similar to altered Diorite close to a structure. In fact, these assumptions are not critical, since the two paths to be studied are quite independent from each other, as will be seen later.

Table 4-3 : Reactive tracer properties

I	**Diffusivity (De)** m^2/s	**Ka** **m**	**Kd** m^3/kg
bg_fil	1.2e-11	0.	0.
bg_rim	4.4e-13	0.	0.
19_gou	1.1e-10	0.	0.
19_cat	9.8e-13	0.	0.
19_dio	4.4e-13	0.	0.
tbDTPA	**Diffusivity (De)** m^2/s	**Ka** **m**	**Kd** m^3/kg
bg_fil	3.0e-12	0.	0.
bg_rim	1.1e-13	0.	0.
19_gou	2.8e-11	0.	0.
19_cat	2.4e-13	0.	0.
19_dio	1.1e-13	0.	0.
Sr	**Diffusivity (De)** m^2/s	**Ka** **m**	**Kd** m^3/kg
bg_fil	5.0e-11	0.	1.3e-3
bg_rim	1.7e-13	1.5e-5	2.6e-5
19_gou	4.4e-11	0.	1.3e-3
19_cat	3.9e-13	2.2e-5	1.4e-4
19_dio	1.7e-13	1.5e-5	2.6e-5
Rb	**Diffusivity (De)** m^2/s	**Ka** **m**	**Kd** m^3/kg
bg_fil	1.3e-11	0.	1.5e-2
bg_rim	4.5e-13	1.0e-4	4.0e-4
19_gou	1.2e-10	0.	1.5e-2
19_cat	1.0e-12	8.0e-4	4.0e-3
19_dio	4.5e-13	1.0e-4	4.0e-4
Cs	**Diffusivity (De)** m^2/s	**Ka** **m**	**Kd** m^3/kg
bg_fil	1.3e-11	0.	1.0e-1
bg_rim	4.5e-13	1.0e-3	5.0e-4
19_gou	1.2e-10	0.	1.0e-1
19_cat	1.0e-12	9.8e-3	3.0e-2
19_dio	4.5e-13	1.0e-3	5.0e-4
HTO	**Diffusivity (De)** m^2/s	**Ka** **m**	**Kd** m^3/kg
bg_fil	1.3e-11	0.	0.
bg_rim	4.7e-13	0.	0.
19_gou	1.2e-10	0.	0.
19_cat	1.0e-12	0.	0.
19_dio	4.7e-13	0.	0.

EuDTPA	**Diffusivity (De)** **m^2/s**	**Ka** **m**	**Kd** **m^3/kg**
bg_fil	3.0e-12	0.	0.
Bg_rim	1.1e-13	0.	0.
19_gou	2.8e-11	0.	0.
19_cat	2.4e-13	0.	0.
19_dio	1.1e-13	0.	0.
Na	**Diffusivity (De)** **m^2/s**	**Ka** **m**	**Kd** **m^3/kg**
bg_fil	8.3e-12	0.	2.0e-4
Bg_rim	2.9e-13	7.0e-7	1.7e-6
19_gou	7.4e-11	0.	2.0e-4
19_cat	6.5e-13	7.0e-7	1.7e-6
19_dio	2.9e-13	7.0e-7	1.7e-6
Ba	**Diffusivity (De)** **m^2/s**	**Ka** **m**	**Kd** **m^3/kg**
bg_fil	5.3e-12	0.	2.7e-2
bg_rim	1.9e-13	2.9e-4	2.9e-4
19_gou	4.7e-11	0.	2.7e-2
19_cat	4.2e-13	2.9e-4	6.9e-4
19_dio	1.9e-13	2.9e-4	6.9e-4
Mn	**Diffusivity (De)** **m^2/s**	**Ka** **m**	**Kd** **m^3/kg**
bg_fil	4.3e-12	0.	1.7e-1
bg_rim	1.5e-13	1.8e-3	1.8e-3
19_gou	3.8e-11	0.	1.7e-1
19_cat	3.4e-13	1.8e-3	4.3e-3
19_dio	1.5e-13	1.8e-3	4.3e-3

4.2.2 Predictions

Table 4-4 shows the tracer paths used for the BS2B tests. Tracers I, tbDTPA, Sr, Rb and Cs are injected in flow path I, while the remaining five tracers, HTO, EuDTPA, Na, Ba, and Mn are injected in flow path II.

Table 4-4: Injection and pumping sections for test BS2B

#	Borehole	Section	Structure / fracture	Distance (m)	Flow path denotation
1	KI0025F02	R3	#19	21	I
2	KI0025F02	R2	BG 1	24	II
3	KI0025F03	R3	#19	pumping	(-)

For each tracer injected, two simulations are performed, using the same flow field. In a first run, we reproduce the actual injection history as provided by the project (TRUE Block Scale Continuation, Data Delivery 4). We then simulate the transport of a Dirac pulse. For both cases, we inject a total of 5000 particles in the model. Table 4-5 shows the performance measures for both real injection histories, and Dirac injections, for the ten tracers considered, including a comparison with experimental data (Andersson et al., 2005). We predict almost complete recovery for most tracers at 5000 hours. Figure 4-9 and Figure 4-10 show the obtained breakthrough curves, for both injection points, and for the two boundary conditions considered. All curves are normalized by the mass of tracer injected. Radioactive decay is not considered.

Table 4-5 : Performance measures, predictions. Experimental values are given in parentheses.

Tracer	Recovery time						% recovery at 5000 hours
	5%, hours		50%, hours		95%, hours		
I	20	*(15)*	42	*(63)*	111	*(-)*	100
I Dirac	14		20		62		100
tbDTPA	20	*(15)*	42	*(63)*	109	*(-)*	100
TbDTPA Dirac	14		20		61		100
Sr	21	*(19)*	45	*(105)*	118	*(-)*	100
Sr Dirac	15		21		67		100
Rb	35	*(51)*	68	*(485)*	208	*(-)*	100
Rb Dirac	25		42		177		100
Cs	142	*(550)*	278	*(-)*	1154	*(-)*	99
Cs Dirac	121		244		1111		99
HTO	74	*(183)*	142	*(790)*	409	*(-)*	99
HTO Dirac	52		89		314		99
euDTPA	71	*(155)*	132	*(500)*	298	*(-)*	100
euDTPA Dirac	48		84		183		100
Na	80	*(300)*	165	*(1500)*	1403	*(-)*	98
Na Dirac	56		101		1296		98
Ba	848	*(3300)*	2070	*(-)*	-	*(-)*	69
Ba Dirac	788		2050		-		69
Mn	4571	*(-)*	-	*(-)*	-	*(-)*	8
Mn Dirac	4516		-		-		9

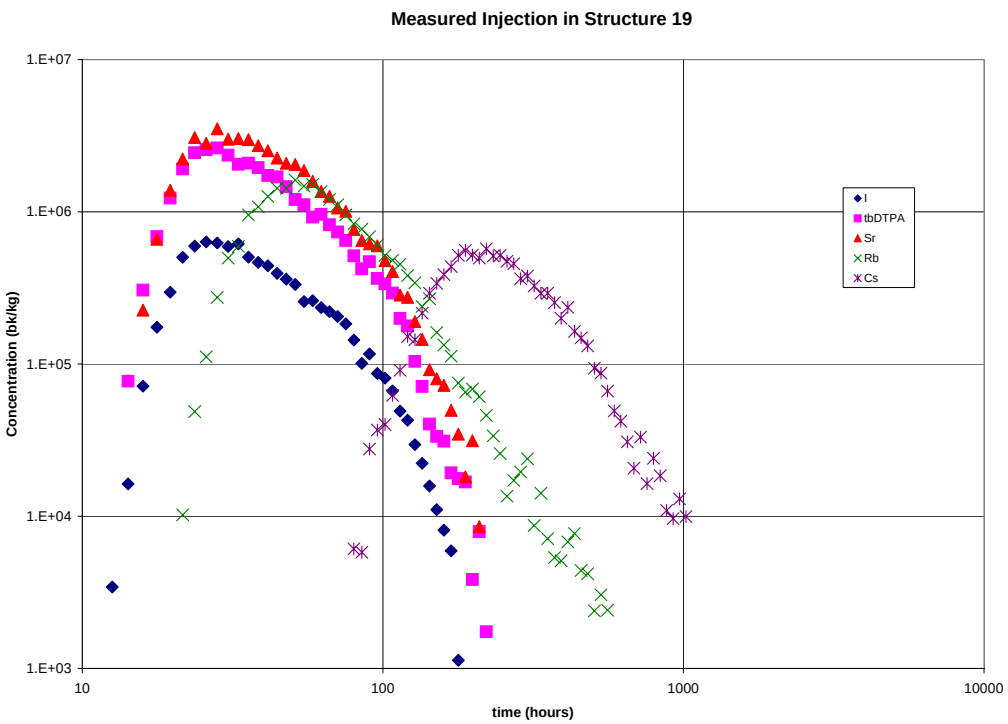

Figure 4-8: *Prediction of BS2B test. Breakthrough curves for the in situ injections in Structure 19, flow path I.*

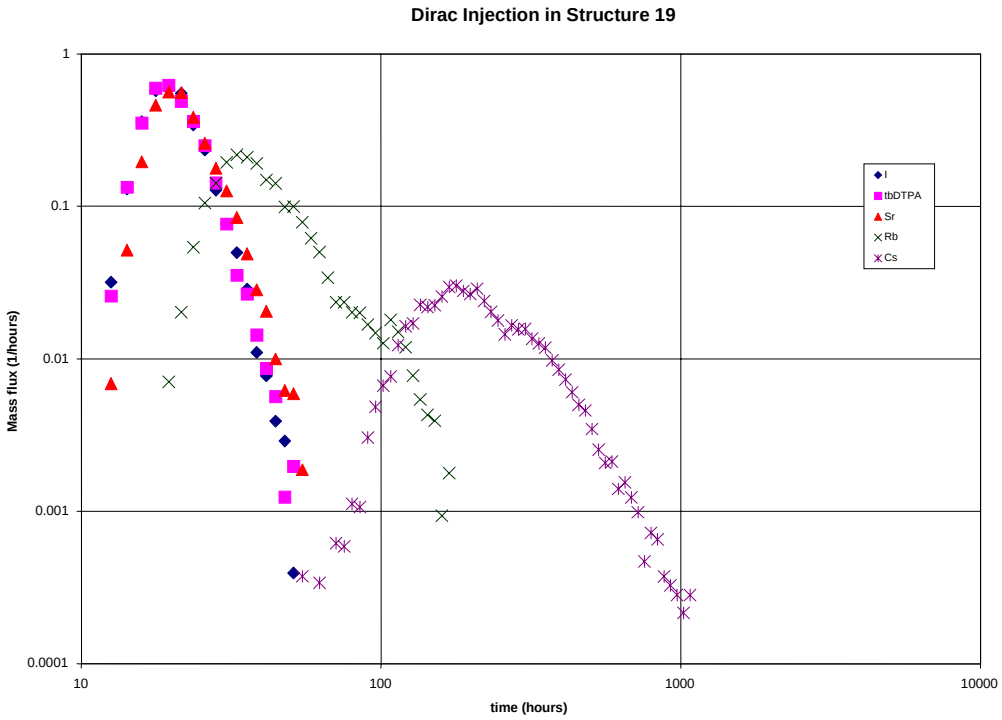

Figure 4-9: *Prediction of BS2B test. Breakthrough curves for Dirac injections in Structure 19, flow path I.*

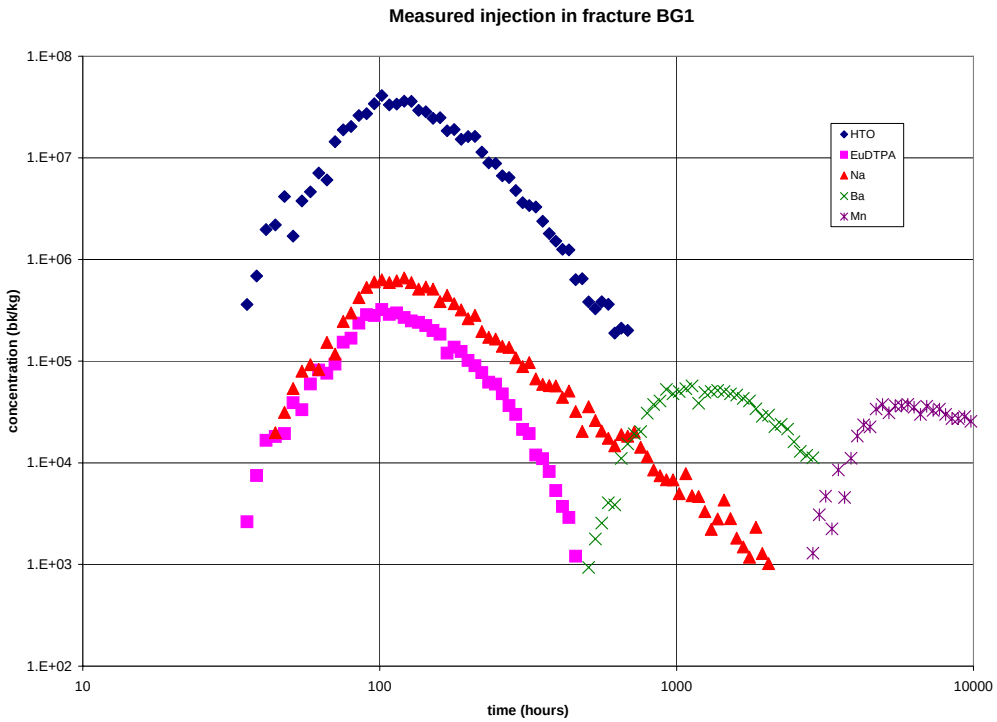

Figure 4-10: *Prediction of BS2B test. Breakthrough curves for the in situ injections in fracture BG1, flow path II.*

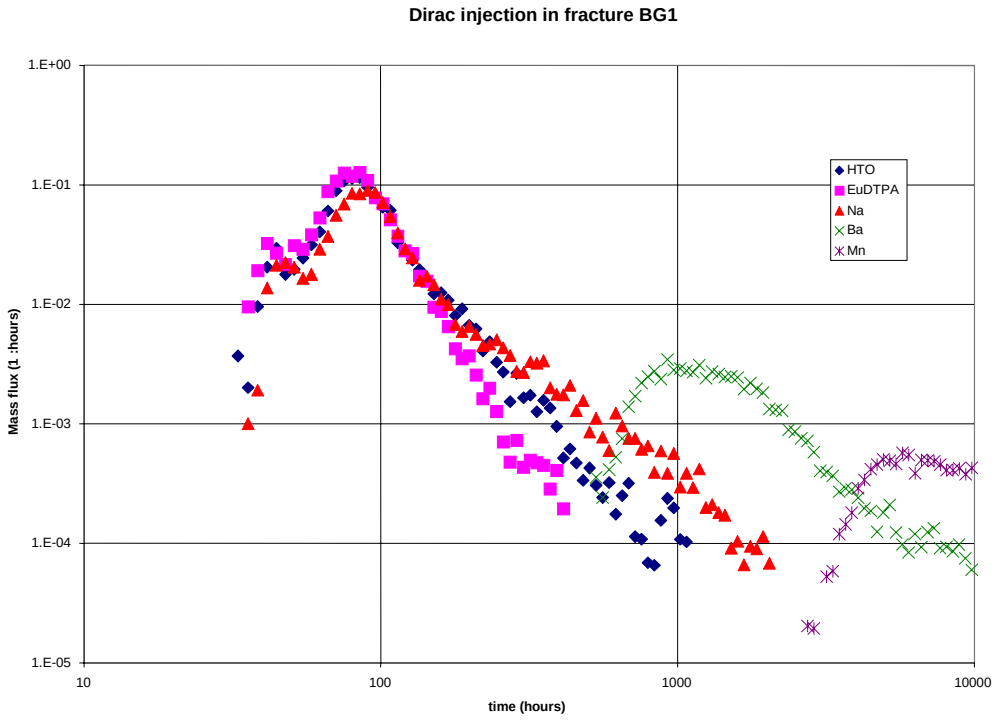

Figure 4-11: *Prediction of BS2B test. Breakthrough curves for Dirac injections in fracture BG1, flow path II.*

4.2.3 Comparison with measurements

The results obtained using the in situ injection curves are reproduced, together with the experimental breakthrough curves corrected for radioactive decay, as provided by the project experimental team (Data Delivery #6), in Figure 4-12 and Figure 4-13. Clearly, the numerical simulations significantly lack retardation. Also, the initial rise of the breakthrough curves is too steep, indicating a lack of dispersivity (or, equivalently, of small scale heterogeneity) in the model.

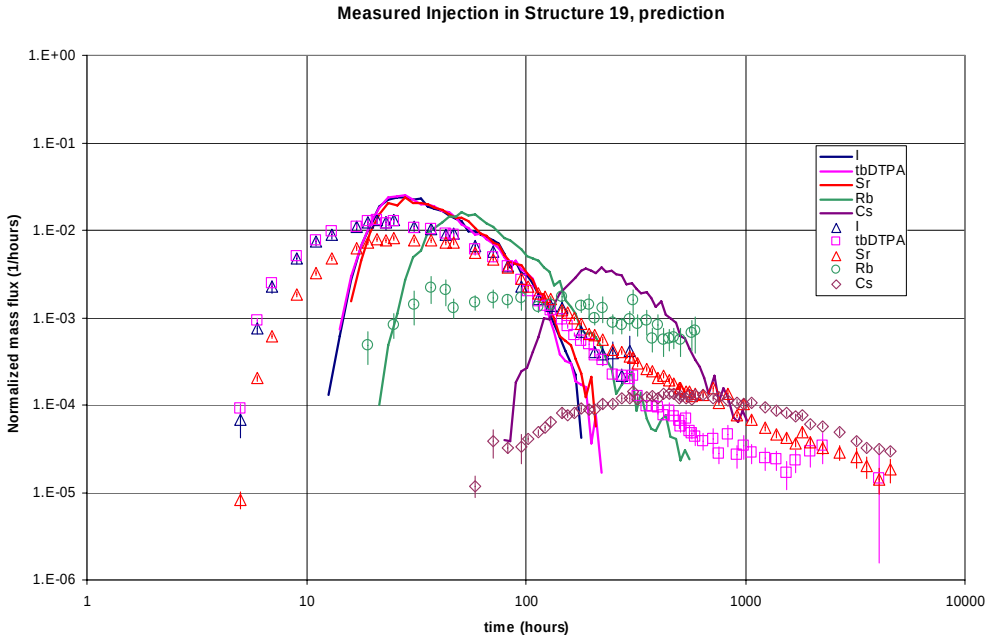

Figure 4-12: *BS2B test, injection in Structure 19 (flow path I). Measured (symbols) and predicted (solid lines) normalized breakthrough curves.*

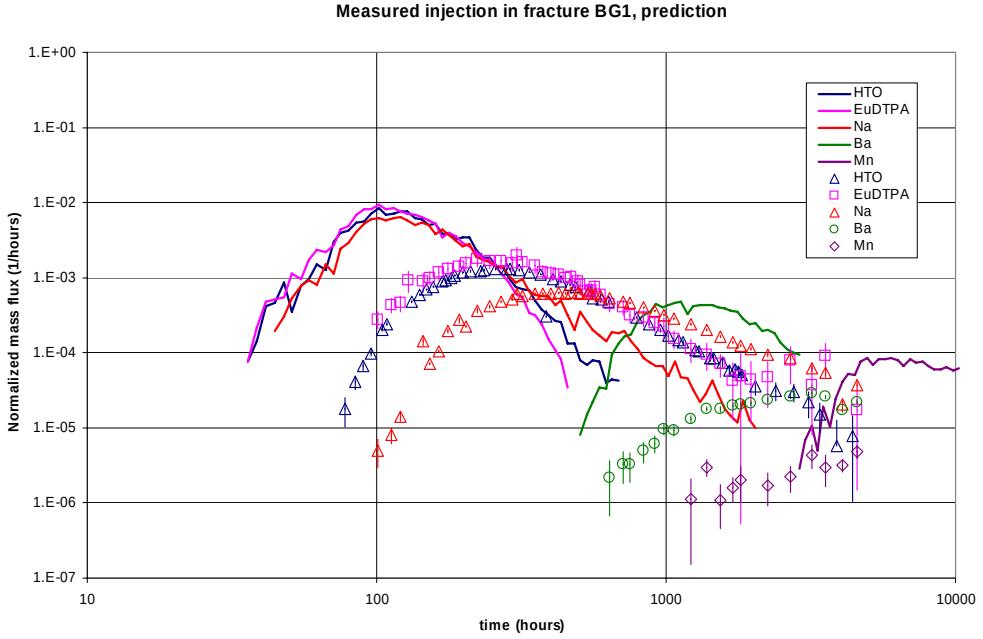

Figure 4-13: *BS2B test, injection in background fracture BG1 (flow path II). Measured (symbols) and predicted (solid lines) normalized breakthrough curves.*

5 Evaluation of in-situ sorbing tracer tests

This section describes numerical simulations aimed at studying the initial hypotheses as expressed in Section 1.1. As mentioned earlier, this individual work can partly tackle Hypothesis I a), "*Microstructural information can provide significant support for predicting transport of sorbing solutes at experimental time scales*", for which a comparison of the various models built by the project modelling teams will eventually be the best test, and try to gain insights into Hypothesis I b), "*Transport at experimental time scales is significantly different for faults and joints, due to the indicated differences in microstructure and properties*".

We first show which of the properties we had chosen caused the significant discrepancies between our predictions and the experimental results, and check that the new parameters obtained are consistent with the calibration data used before. The flow path II between the BG 1 background fracture injection and the pumping section in Structure #19 is then studied in detail, as well as the significance of the differences between Structure #19 and the background fracture population. We present here the results of the various simulations performed, together with the rationale for choosing these simulations. These results will then be further discussed in Chapter 6.

5.1 Prediction discrepancies

The objective of this part of the work is not to obtain a perfect match between a new model and the experimental results. In fact, such a "posterior" match is of little interest. We choose to stay within the same structural model (i.e. structure geometry, but also statistical geometrical properties of the background fractures network, for which we use the same realization as previously). We concentrate instead on trying to understand how the choice of microstructural parameters, and then process parameters, can yield more realistic curves.

5.1.1 Microstructural model parameters

Here, we investigate the effect of the microstructural parameters: pore space properties and dispersivities. These parameters do not vary from tracer to tracer, therefore they may explain a general "bias" or a poor shape in the breakthrough curves, but will not have a direct effect on the differences between the tracers.

We had chosen to mostly disregard the fault gouge and fracture filling in the prediction model, concentrating instead on the interaction of the tracer with the rock on the sides of the fractures and structures. This resulted in a significant underestimation of the retention in all cases. So we increase drastically the amount of gouge/fracture filling to be encountered by the tracers. We now consider that half of the background fractures and structures flow area is in contact with fault gouge or fracture filling. Table 5-1 shows the new pore space properties (refer to Table 4-2 for the meaning of material names). Also, to simulate a strong local heterogeneity in the flow field, we increase the local dispersivities D_l in the channels, from 0 m to 2 m in background fractures, and from 1 m to 5 m in Structure #19.

Table 5-1 : Immobile pore space for the evaluation model (previous values, for the prediction model, are in parentheses)

	Name	Fraction of area	Porosity	Density kg/m^3
BG fractures				
Fracture filling	bg_fil	**0.50** *(0.05)*	0.05	2500
Altered diorite	bg_rim	**0.50** *(0.95)*	0.006	2500
Structure 19				
Gouge filling	19_gou	**0.50** *(0.05)*	0.20	2500
Cataclasite/Mylonite	19_cat	**0.10** *(0.20)*	0.01	2500
Altered diorite	19_dio	**0.40** *(0.75)*	0.006	2500

Figure 5-1 and Figure 5-2 show the new breakthrough curves we obtained. Note that these results are obtained with the same realization of the network as used before. While not a perfect match, the curves are much closer to the experimental ones than the original predictions. Time scales are well reproduced, except for Ba and Mn injected in BG 1 (flow path II), for which retardation is too strong. Also, the tails of the breakthrough curves tend to be somewhat too steep for flow path I. These tails could be be changed by considering a variation in the porosity of the Structure #19 materials: through the use of Archie's law for the computation of the Formation Factor, porosities directly condition the diffusivities for the various tracers.

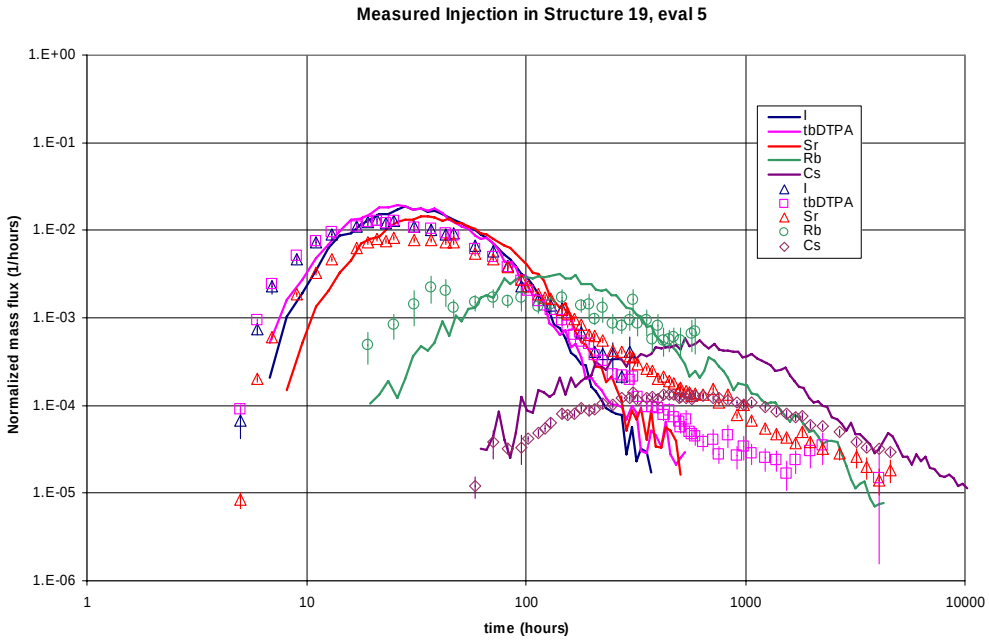

Figure 5-1: *BS2B test, injection in Structure 19, flow path I. Microstructural model evaluation. Measured and predicted normalized Breakthrough curves.*

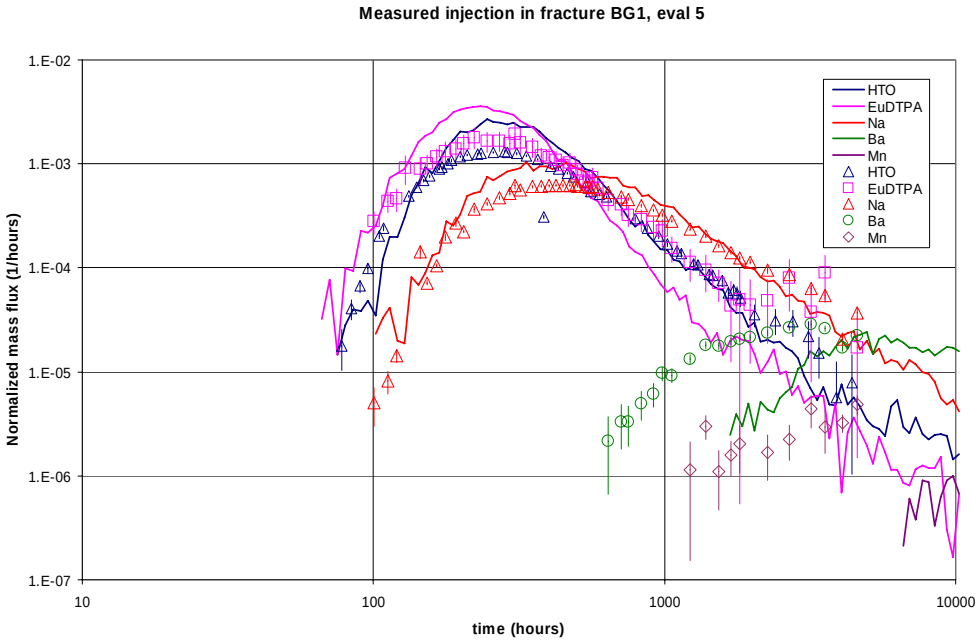

Figure 5-2: *BS2B test, injection in background fracture BG1, flow path II. Microstructural model evaluation. Measured and predicted normalized Breakthrough curves.*

5.1.2 Process parameters

As could be noted on Figure 5-2, after changing the microstructural model, we are left with a discrepancy between the relative retardations of (HTO, EuDTPA, Na) on one side, and (Ba, Mn) on the other side. However, the Kd values for Ba and Mn are in fact not known directly, but inferred from tests on the fault gouge found in Structure #20. Therefore, we can consider the effect of a change in these values.

Figure 5-3 and Figure 5-4 show the breakthrough curves we obtain when dividing by four the Kd's for Ba and Mn in fault gouge and in background fracture fillings:

- Kd for Ba is $6.8 \cdot 10^{-3}$ instead of $2.7 \cdot 10^{-2}$
- Kd for Mn is $4.25 \cdot 10^{-2}$ instead of $1.7 \cdot 10^{-1}$

These updated new breakthrough curves show an acceptable behaviour for Ba, while Mn retardation is still a little too strong.

Note that the experimental responses for HTO and EuDTPA are very similar, with identical tails. The simulated responses for these two tracers cannot be the same, since the diffusivity for HTO is four times the diffusivity of EuDTPA, and everything else is identical between the two tracers. With the HTO breakthrough curve very well matched, the EuDTPA one cannot be as good.

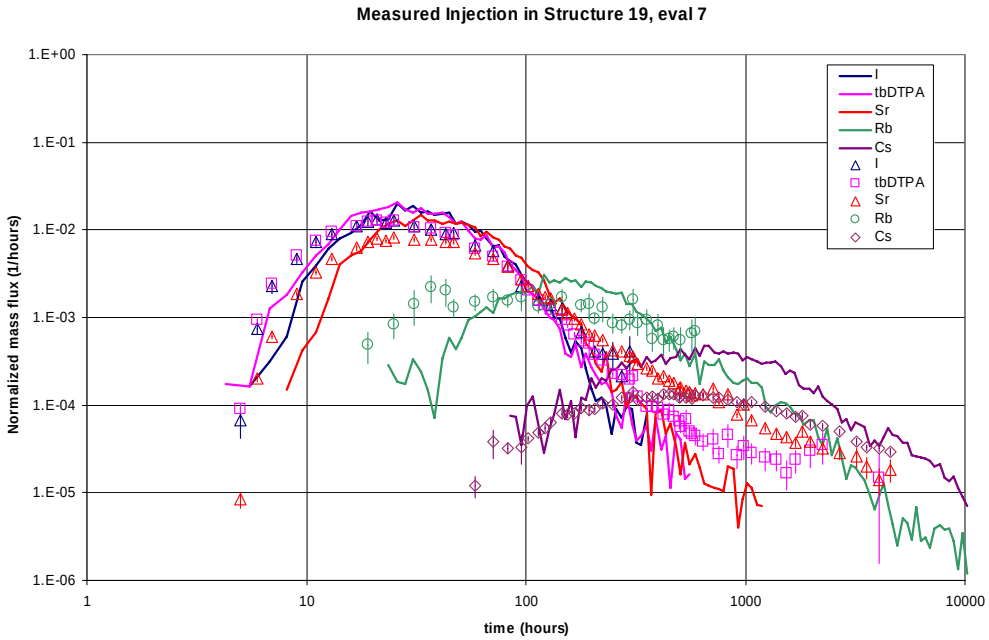

Figure 5-3: *BS2B test, injection in Structure #19, flow path I. Measured and predicted normalized Breakthrough curves. Process evaluation (Modified Kd's for Ba and Mn).*

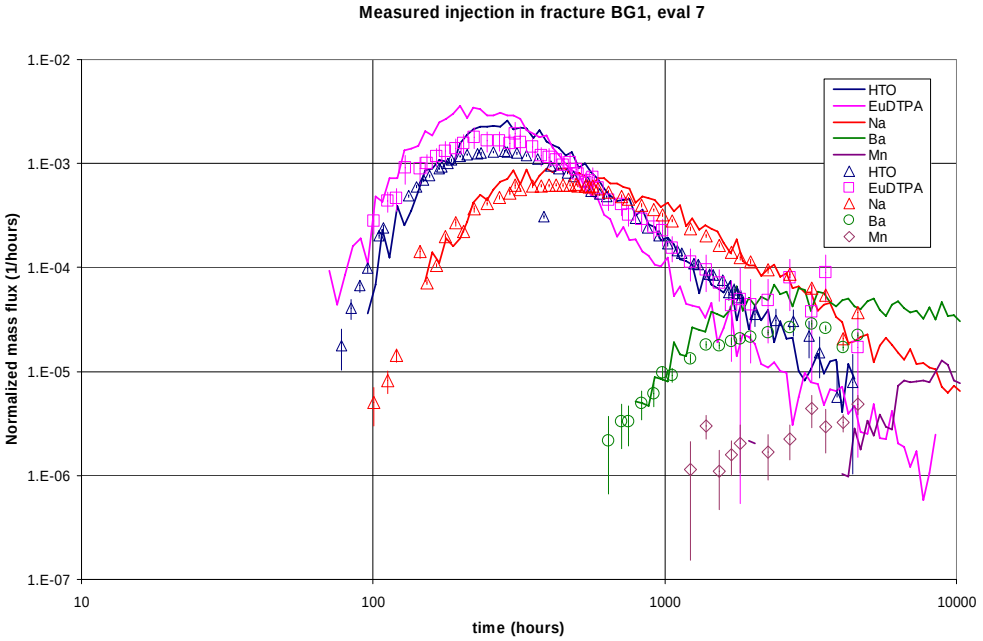

Figure 5-4: *BS2B test, injection in fracture BG1, flow path II. Measured and predicted normalized Breakthrough curves. Process evaluation (Modified Kd's for Ba and Mn).*

5.1.3 Check of parameters consistency

The parameters used for the prediction simulation were obtained by a calibration to the CPT-4a to CPT-4c tracer tests, as discussed in Section 4.1. We need to check if the new transport parameters used for the evaluation are also compatible with these earlier tests, to insure consistency of our model. Figure 5-5 to Figure 5-7 show the breakthrough curves we obtain, with these new parameters, when simulating the calibration tests. By comparison with the previous breakthrough curves (Figure 4-4 to Figure 4-6), the new curves are as well fitted (with even a slightly better fit for some tests) as compared with the previous ones. This means that the evaluation parameters we chose provide a consistent model, able to reproduce adequately all observed behaviour - we are probably taking into account enough physical phenomena for the task at hand.

However, a negative implication is that very different retardation behaviours can be obtained for two sets of parameters (the "prediction" and the "evaluation" ones), both yielding almost identical responses for the calibration tests simulations. The calibration as performed here did not provide enough constrains to accurately predict the later runs.

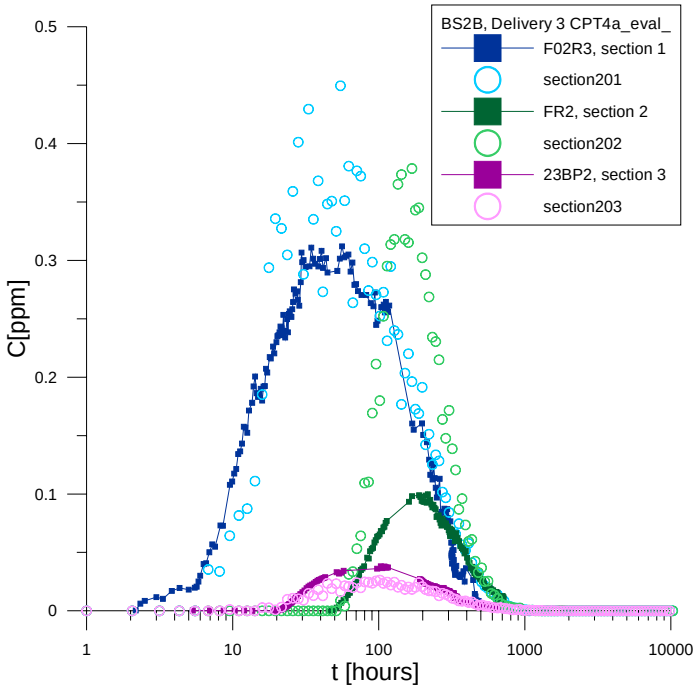

Figure 5-5: *CPT-4a test simulations breakthrough curve, evaluation parameters. One realization.*

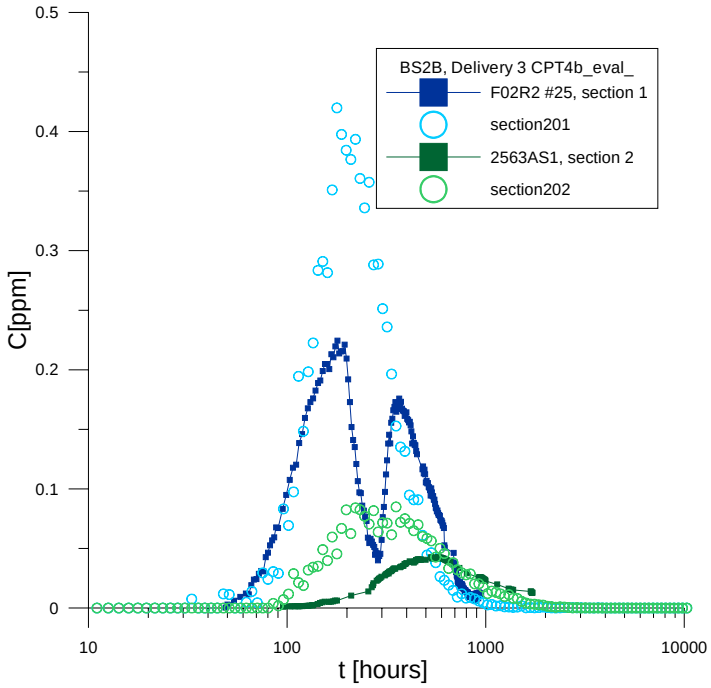

Figure 5-6: *CPT-4b test simulations breakthrough curve, evaluation parameters. One realization.*

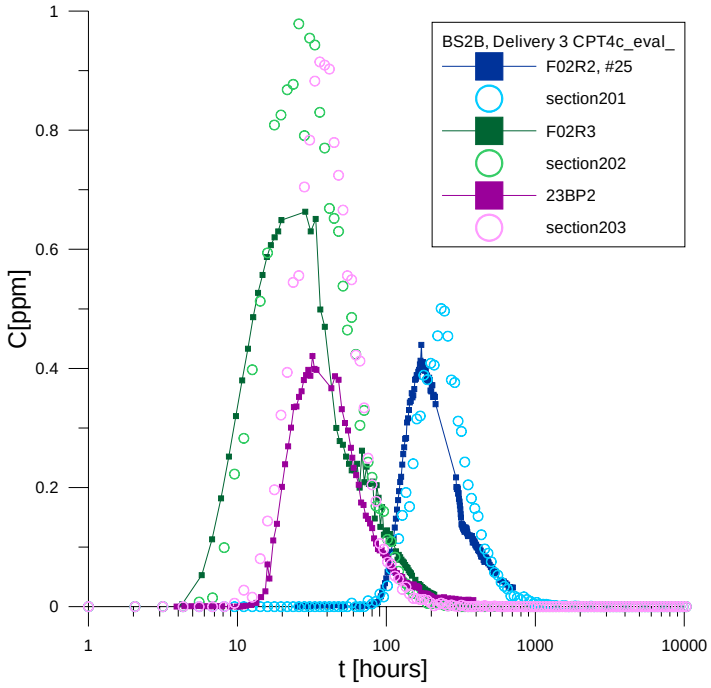

Figure 5-7: *CPT-4c test simulations breakthrough curve, evaluation parameters. One realization.*

5.1.4 Performance measures

Table 5-2 shows the new performance measures we obtain with the new evaluation parameters. We also provide the performance measures for the experimental results, when available. The results for a Dirac injection are illustrated in Figure 5-8 and Figure 5-9.

Table 5-2 : Performance measures, evaluation. Experimental values are given in parentheses.

Tracer	Recovery time						% recovery at 5000 hours
	5%, hours		50%, hours		95%, hours		
I	16	*(15)*	45	*(63)*	162	*(-)*	100
I Dirac	8		20		109		100
tbDTPA	15	*(15)*	42	*(63)*	141	*(-)*	100
TbDTPA Dirac	7		18		92		100
Sr	20	*(19)*	57	*(105)*	266	*(-)*	99
Sr Dirac	12		30		248		99
Rb	82	*(51)*	286	*(485)*	5751	*(-)*	95
Rb Dirac	61		248		4643		95
Cs	343	*(550)*	1720	*(-)*	-	*(-)*	73
Cs Dirac	343		1761		-		72
HTO	180	*(183)*	403	*(790)*	4312	*(-)*	95
HTO Dirac	141		342		3945		96
euDTPA	143	*(155)*	298	*(500)*	1427	*(-)*	98
euDTPA Dirac	110		233		1300		98
Na	280	*(300)*	999	*(1500)*	-	*(-)*	86
Na Dirac	238		958		-		86
Ba	2261	*(3300)*	-	*(-)*	-	*(-)*	19
Ba Dirac	2298		-		-		18
Mn	-	*(-)*	-	*(-)*	-	*(-)*	0.35
Mn Dirac	-		-		-		0.47

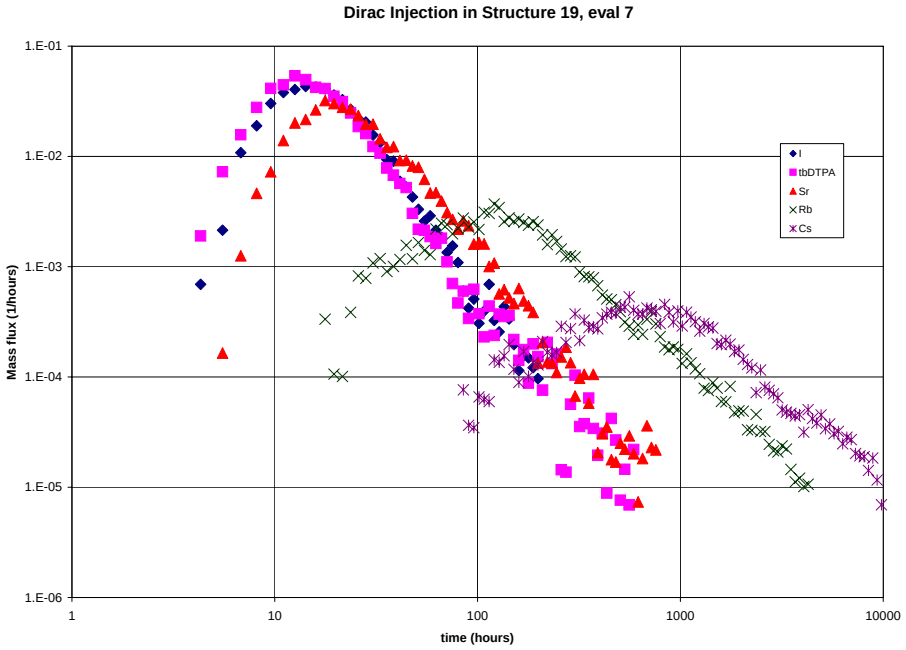

Figure 5-8: *BS2B test evaluation, simulated breakthrough curves for Dirac injection in Structure #19, flow path I (evaluated parameters).*

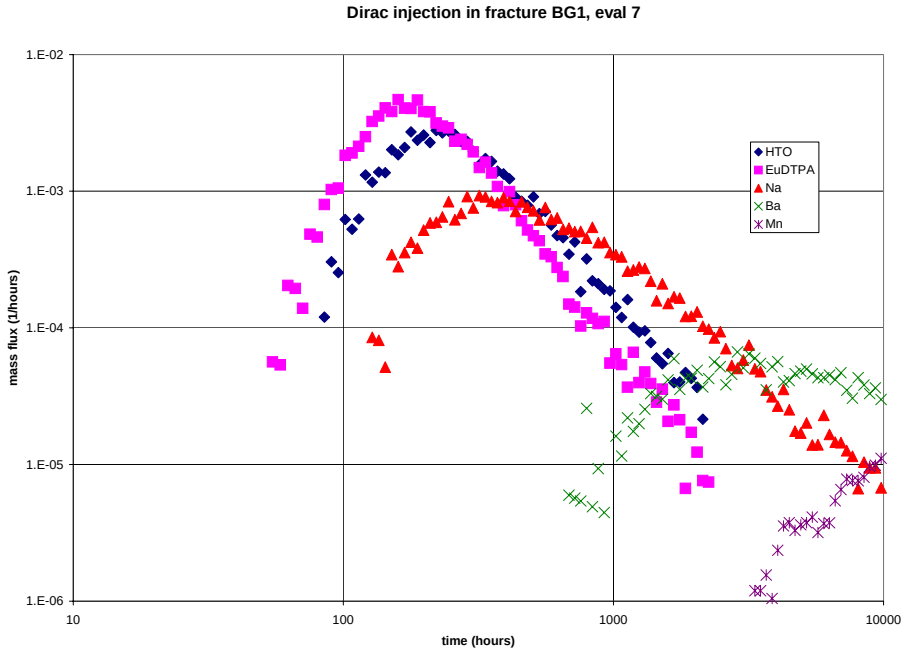

Figure 5-9: *BS2B test evaluation, simulated breakthrough curves for Dirac injection in fracture BG1, flow path II (evaluated parameters).*

5.2 Analysis of tracer paths

In this section, we study the properties of the paths followed by the tracers between the injection section in BG1 and the pumping section in Structure #19 (flow path II).

In order to fix ideas, we first show images of the transport paths for both flow paths I and II in relation to the full model. As illustrated in Figure 5-10 and Figure 5-15, flow path I occurs almost exclusively between the two boreholes in the plane of Structure # 19. Only a handful of background fractures (Figure 5-15) are touched by the tracers. Flow path II is also limited to a few background fractures before the tracers reach the sink constituted by Structure # 19 (Figure 5-12 and Figure 5-17). As can be seen in these figures, in the realization of the network we use here, fracture BG 1 does not intersect Structure #19.

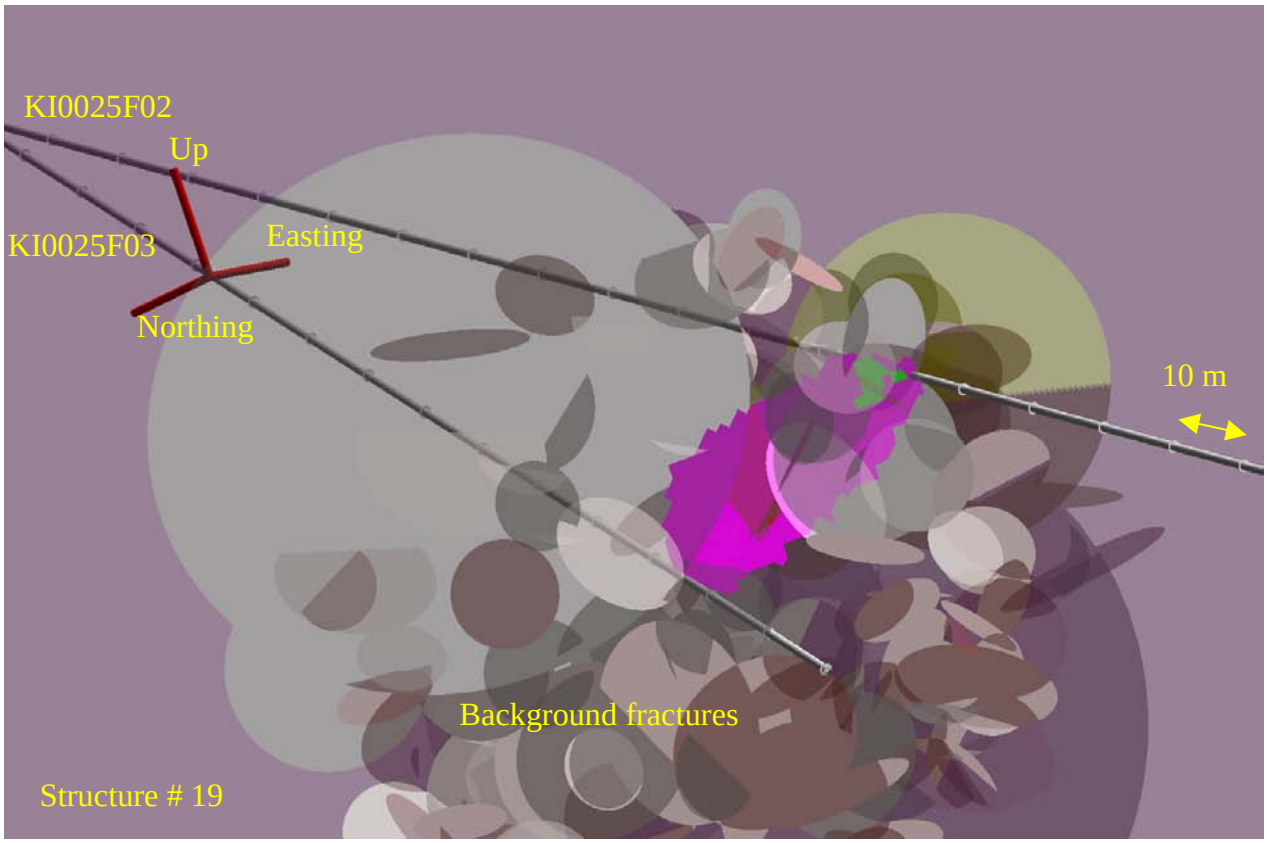

Figure 5-10: *BS2B test, injection in Structure # 19 – flow path I. View of the transport path along Structure # 19 (in pink), and of the background fractures (semi-transparent).*

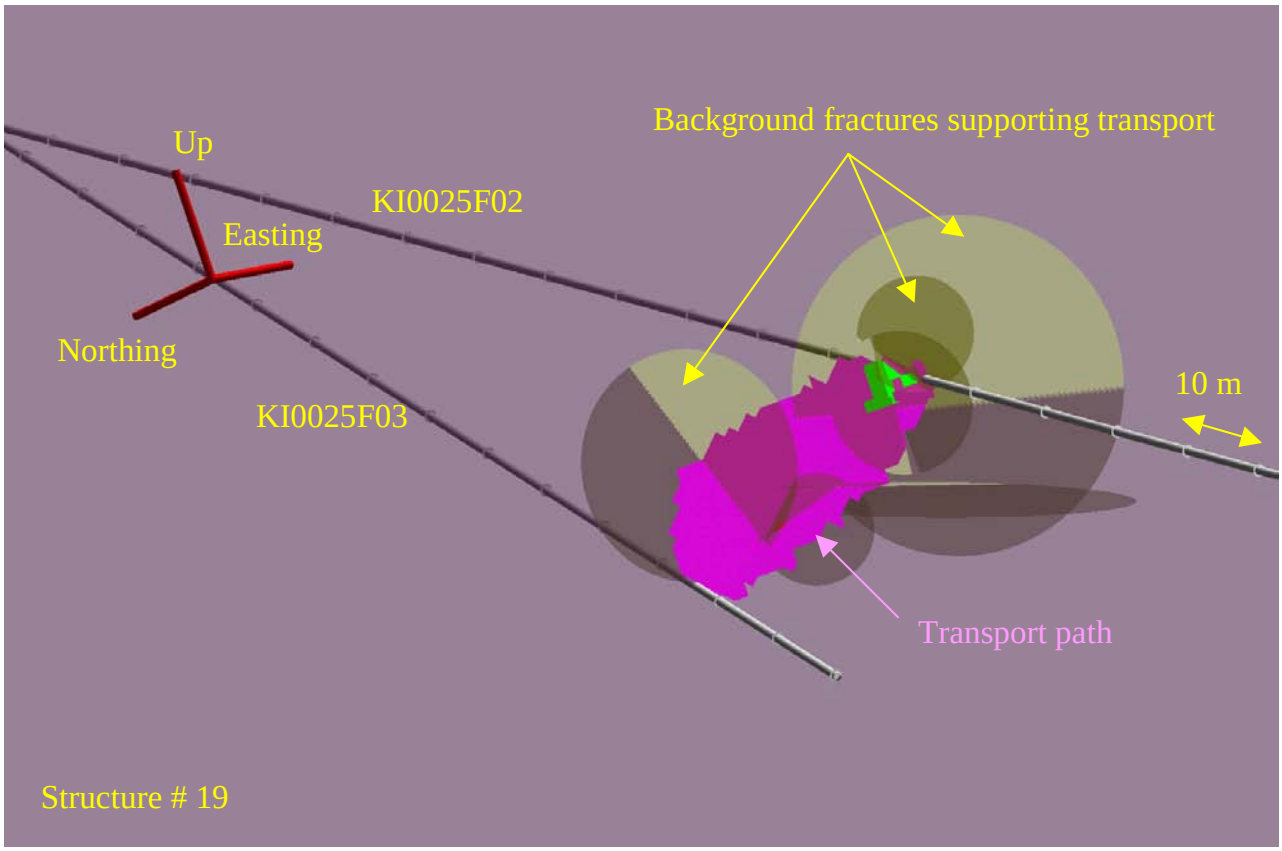

Figure 5-11: *BS2B test, injection in Structure # 19 – flow path I. View of the transport path along Structure # 19 (in pink), and of the background fractures supporting transport (semi-transparent).*

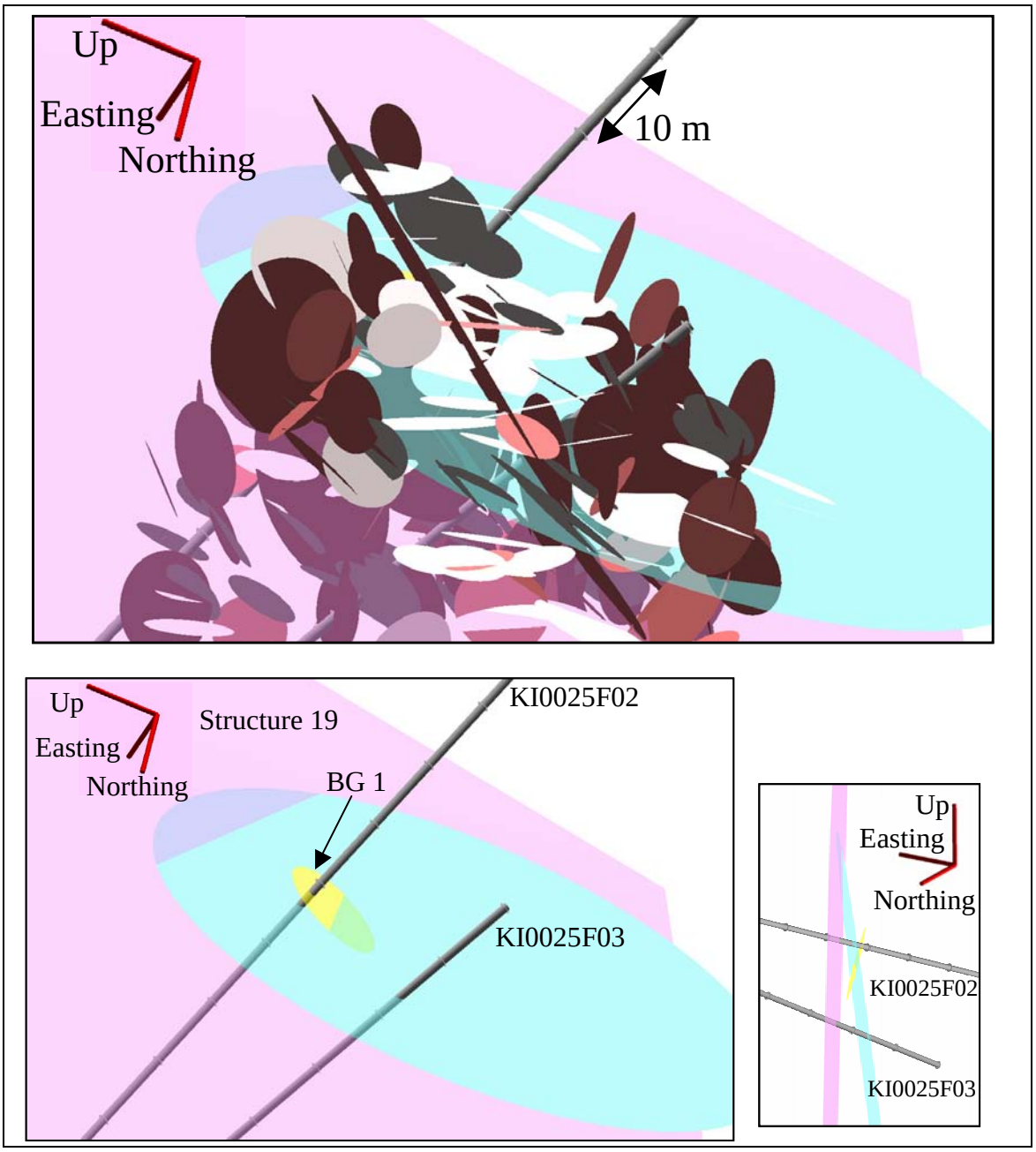

Figure 5-12: *BS2B test, injection in fracture BG1 – flow path II. Top: View of all fractures. Bottom: main transport-supporting features, from two viewpoints.*

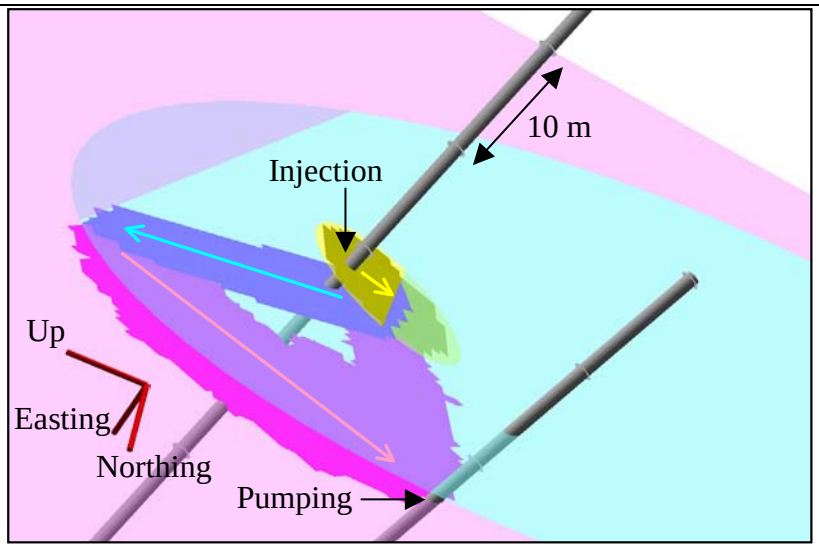

a) main transport path (coloured arrows show direction of flow)

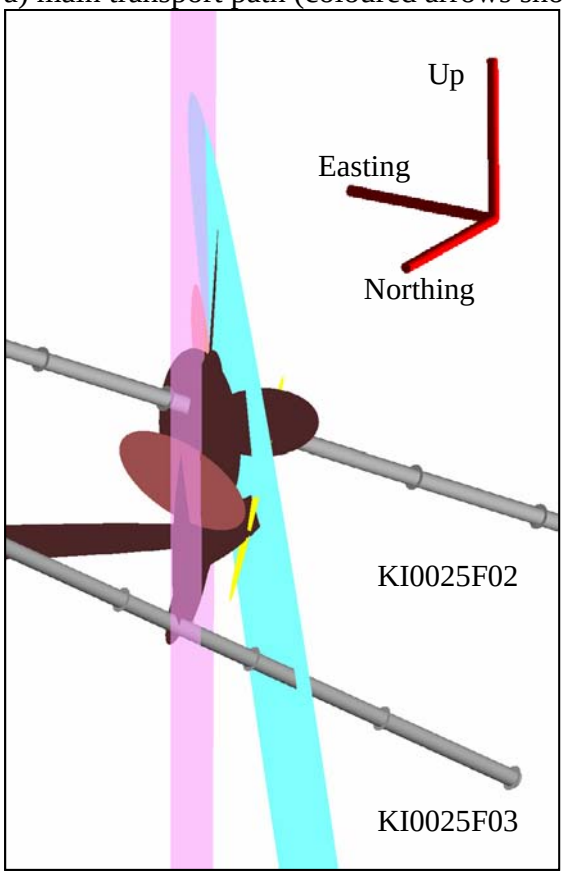

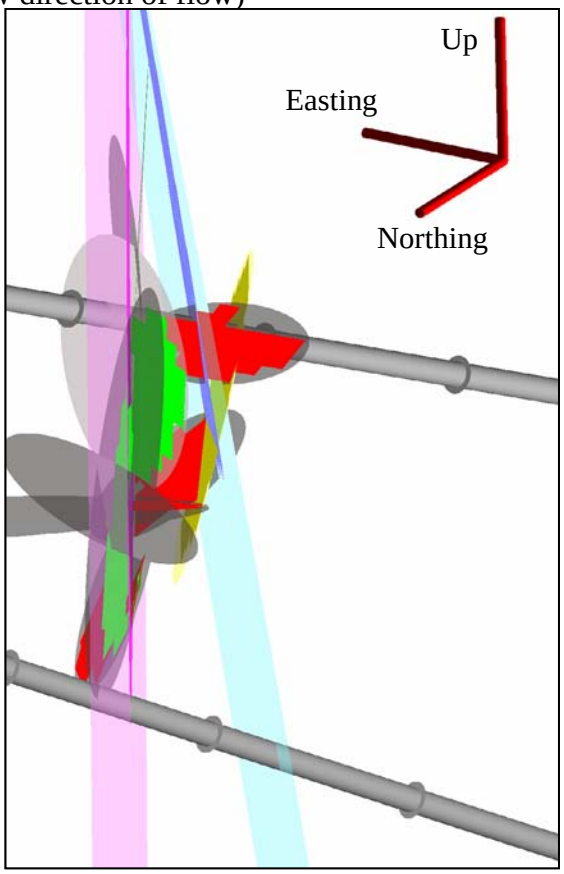

b) background fractures supporting secondary transport path c) secondary transport path

Figure 5-13: *BS2B test, injection in fracture BG1 – flow path II. The transport paths.*

The following graphics are based on the simulation of the HTO injection, however the path geometry does not depend on the tracer. Figure 5-14 and Figure 5-15 illustrate the exact model geometry of these paths, with all individual pipes drawn. Figure 5-14 outlines the three features that make up the main transport path: BG 1 (green colour), a large background fracture (cyan colour), then Structure #19 (yellow colour).

Figure 5-15 is a close-up, in which channels that where actually invaded by particles during the simulation are differentiated. The channels in Structure #19 are shown in two colours: yellow for parts of the structure never touched by the tracer, and orange for the channels which are crossed by at least one particle during the simulation. Besides Structure #19, only invaded channels are represented, distinguishing between invaded channels in BG 1 (green colour), and invaded channels in all other background fractures (cyan colour). We observe the "main path" along a large background fracture (due South-East, towards the top of the figure), then back to KI0025F03 along Structure #19. More direct "secondary paths" use background fractures sub-orthogonal to Structure #19. Note that the total area covered by the tracer is quite large, with most of the BG1 fracture invaded.

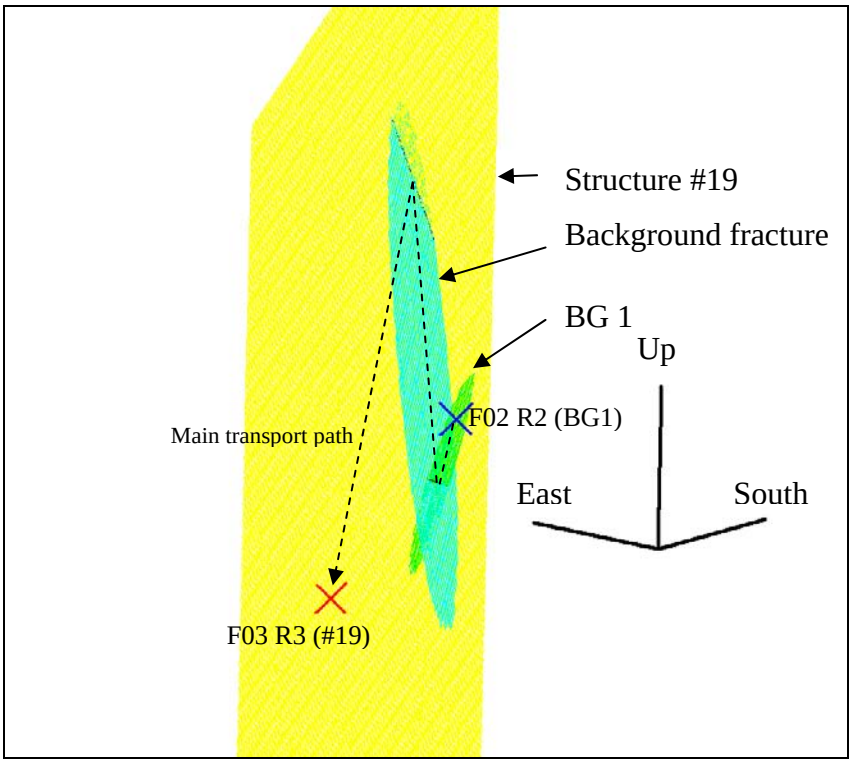

Figure 5-14: *BS2B test, injection in fracture BG1 – flow path II. Main features supporting tracer transport.*

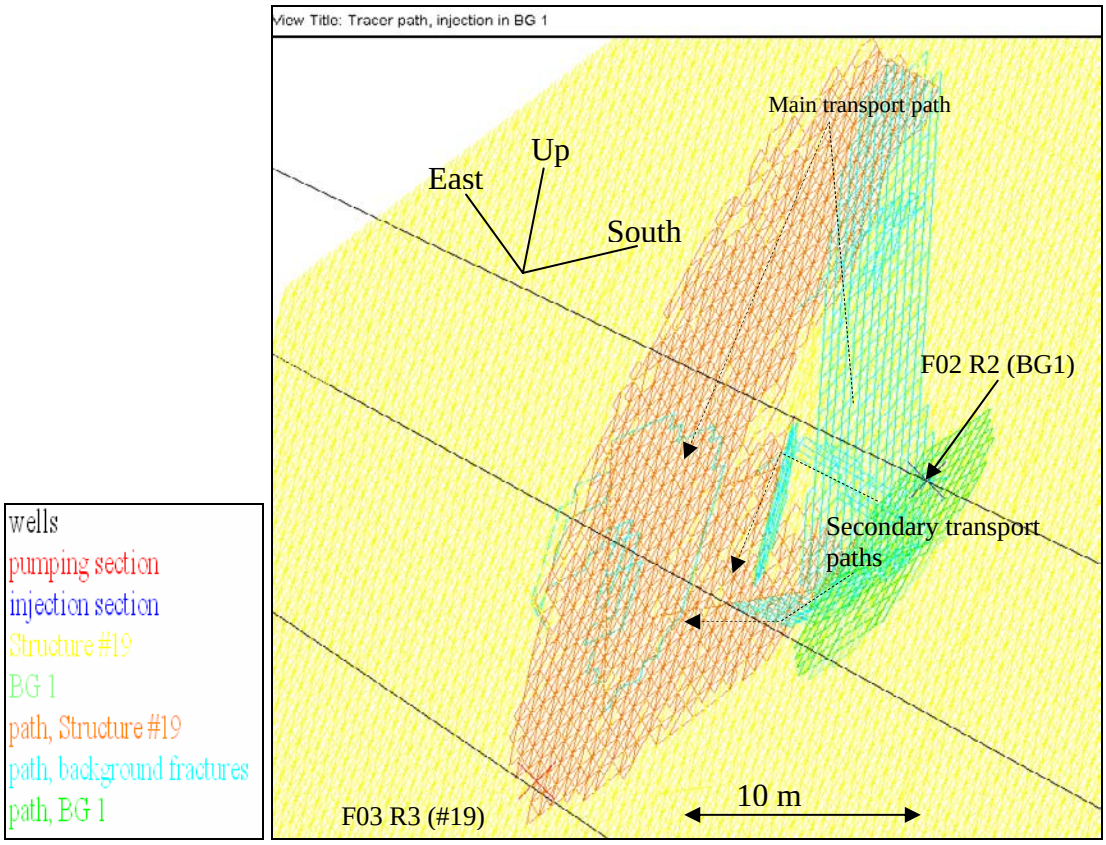

Figure 5-15: *BS2B test, injection in fracture BG1. Transport paths to pumping in Structure #19.*

The following two figures use the same view angle, and concentrate on the tracer-invaded channels, for the case of the HTO injection (conservative tracer, retarded by diffusion only). In Figure 5-16, we show mean arrival times in the various channels. The colour code is in fact for the decimal logarithm of the time (in hours), to enable a better representation of the earlier times. To fix ideas, note that the 50% recovery time (403 hours, see Table 5-2) corresponds to a log-time of 2.6. The mean arrival time at the pumping node is effectively in this range. We observe first a radial spread of the plume in BG 1, corresponding to a forced injection in a low aperture fracture. Once the tracer invasion reaches the intersection with the large background fracture (on the average, after $10^{2.25}$ = 180 hours), tracer is transported relatively fast towards Structure #19, then along the structure towards KI0025F03. Figure 5-17 shows the ratio of the total mass injected supported by each channel, in log scale: most of the tracer flows along the large background fracture and back along the structure. For comparison, we show the same log mass ratio for the injection in Structure #19 (using the test with Iodine) on Figure 5-18. The colour scale is the same for the two figures. The tracer paths are more concentrated for the Structure #19 injection, despite the larger injection flow rate, since there is no "spreading effect" from injecting in a relatively "tight" fracture.

Figure 5-19 shows the flow rates in channels making up the main transport path, with radial spreading at very low flow rates in BG1: flow rates decrease out from the source, then essentially one-dimensional in the large background fracture, with almost uniform flow rates (except a slight concentration when reaching Structure #19). Flow in Structure #19 is more complex because its large number of connections, and of its large heterogeneity, but is still mostly one-dimensional along most of the main transport path, then becomes radially converging when approaching the sink.

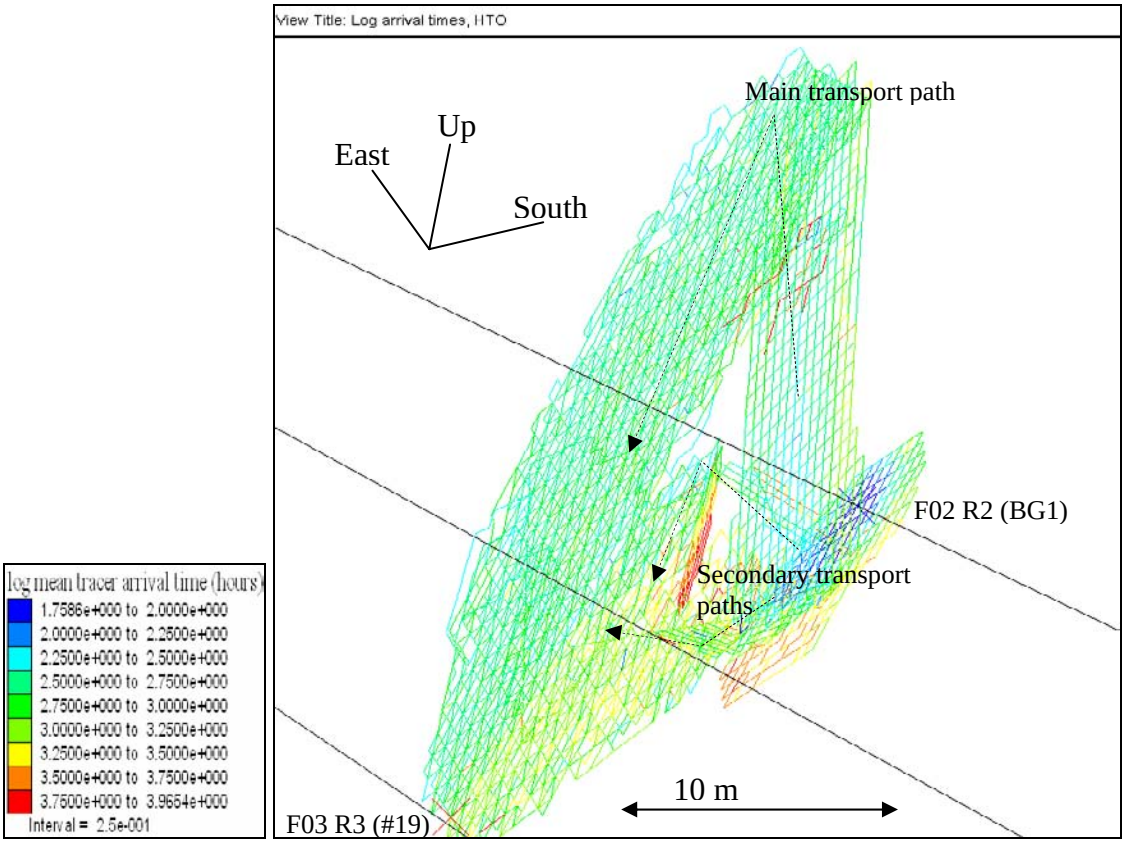

Figure 5-16: *BS2B test, HTO injection in fracture BG1. Log of mean arrival times in channels along the transport paths.*

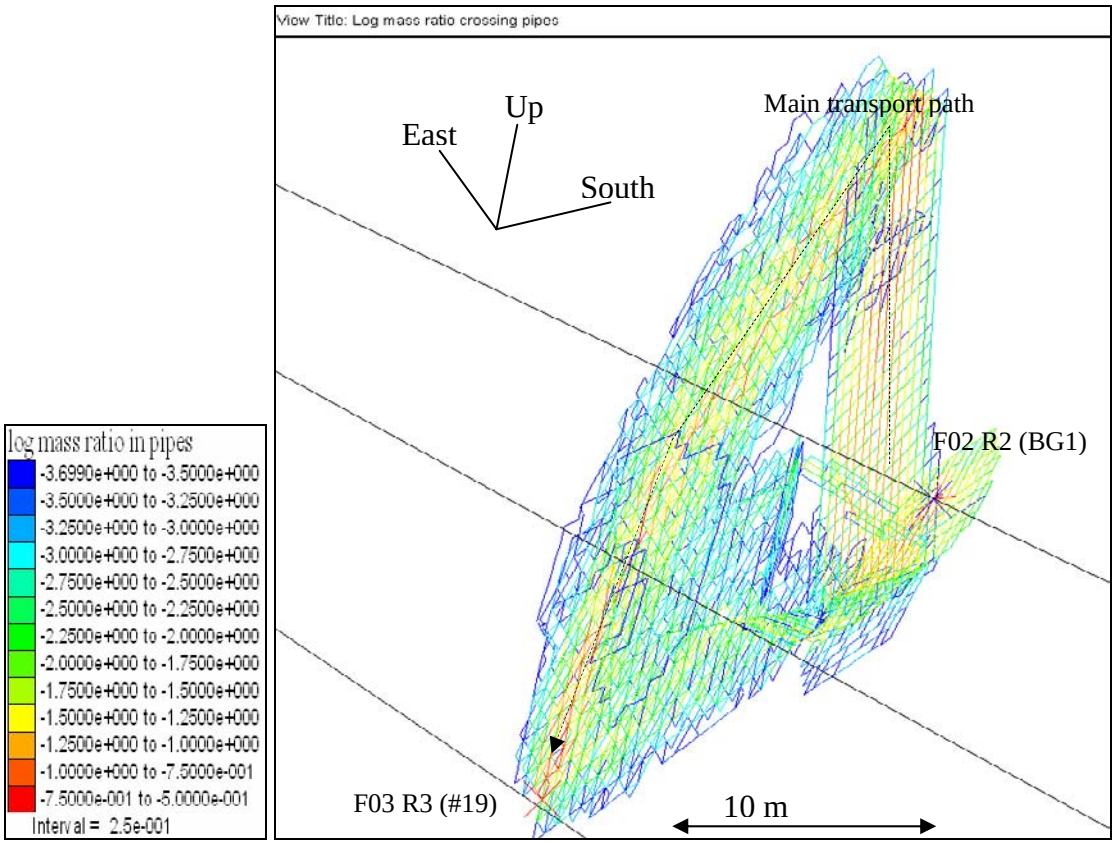

Figure 5-17: *BS2B test, HTO injection in fracture BG1. Log of mass ratio travelling through each channel along the transport paths.*

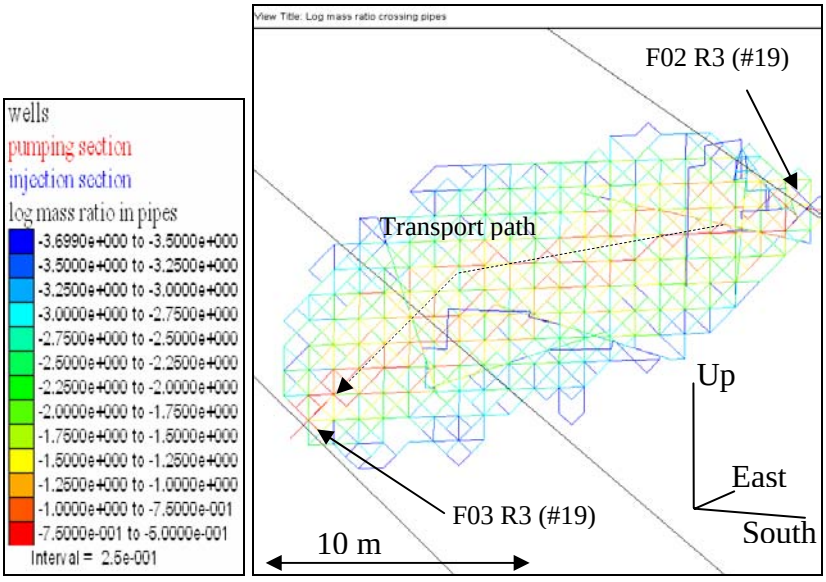

Figure 5-18: *BS2B test, Iodine injection in Structure # 19 (flow path I). Log of mass ratio travelling through each channel along the transport path.*

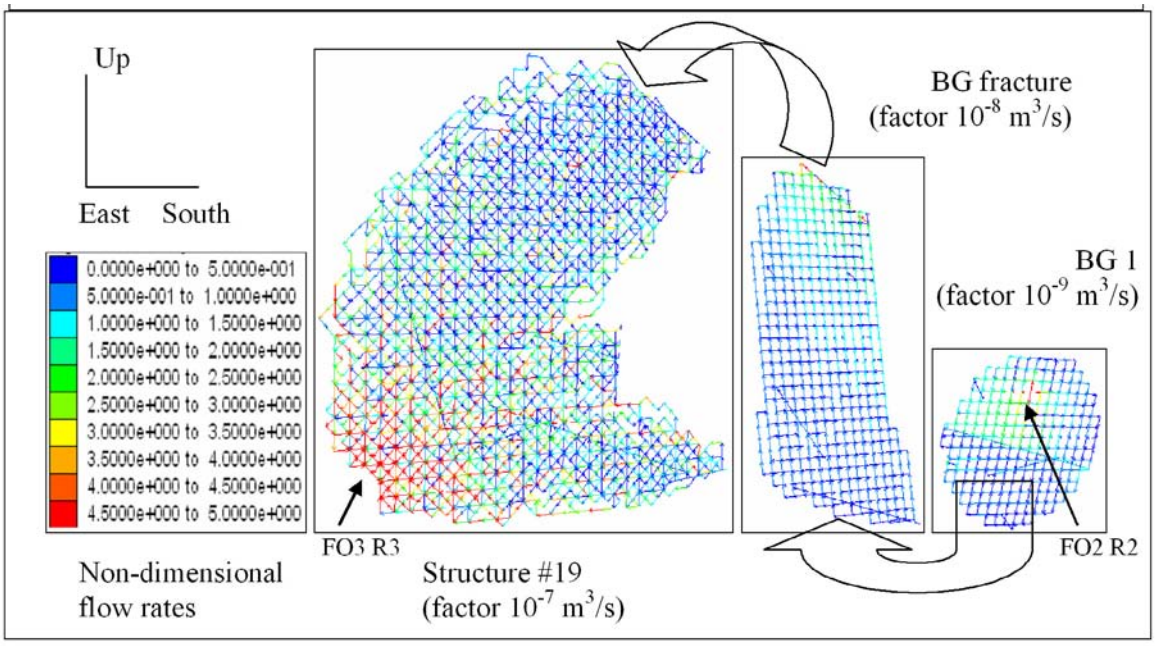

Figure 5-19: *BS2B test, HTO injection in BG 1 (flow path II). Flow rates in the main parts of the flow path. Flow rate in each plot is product of colour scale by indicated factor.*

By monitoring the displacements of all particles during simulations, we are able to study in detail the geometry of their paths from injection to pumping. For each particle, we record the total path length, the length of the part of the path situated in Structure #19 and in background fractures. Also, our conceptual model fully defines the section, length, and therefore the volume, of all the channels in the model. We can therefore add-up the volumes of all the channels travelled by a given particle to obtain the total flowing volume "seen" by the particle.

For flow path I (injection in Structure #19), we find a mean path length of 29 m, completely situated in the structure. For flow path II (injection in background fracture BG 1), we find a – much longer – path length of 71 m. On the average, 29 m of flow path II are travelled in background fractures and 42 m are travelled in Structure #19.

We show in Figure 5-20 and Figure 5-21 the distribution of path volumes seen by each particle, both for flow path I (injection in Structure #19), and for the flow path II (injection in fracture BG 1). These volumes are mostly situated in Structure #19 for both tracer paths, with a bimodal distribution for flow path II. The lower peak in Figure 5-21 corresponds to more direct paths towards Structure #19, while the higher peak reflects the long main path.

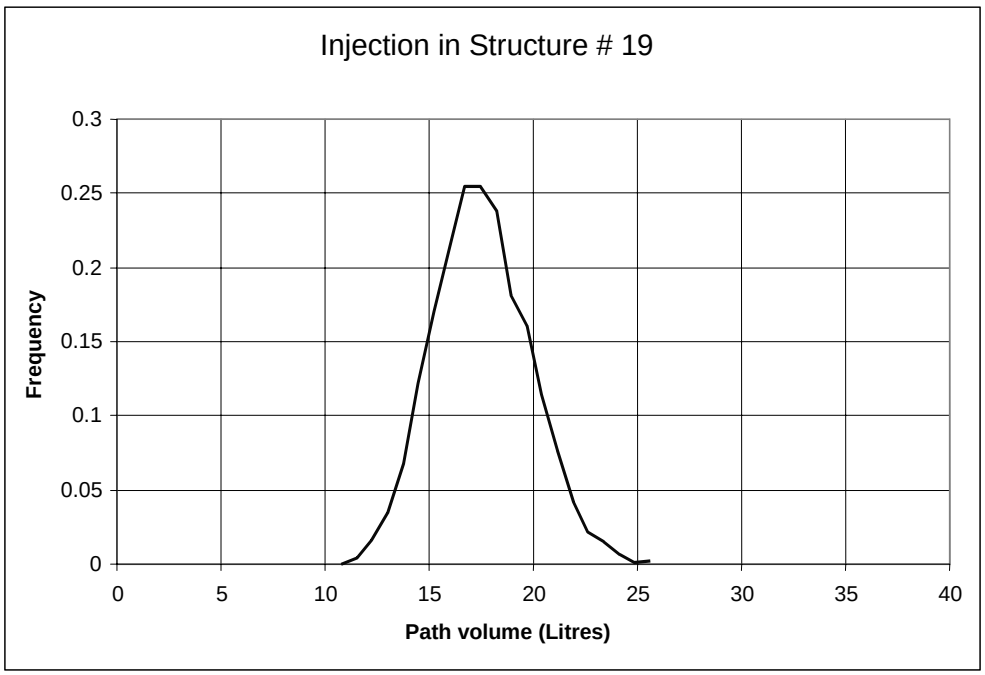

Figure 5-20: *BS2B test, injection in Structure #19 – flow path I. Statistical distribution of path volumes. Bin size is 1.485 litre.*

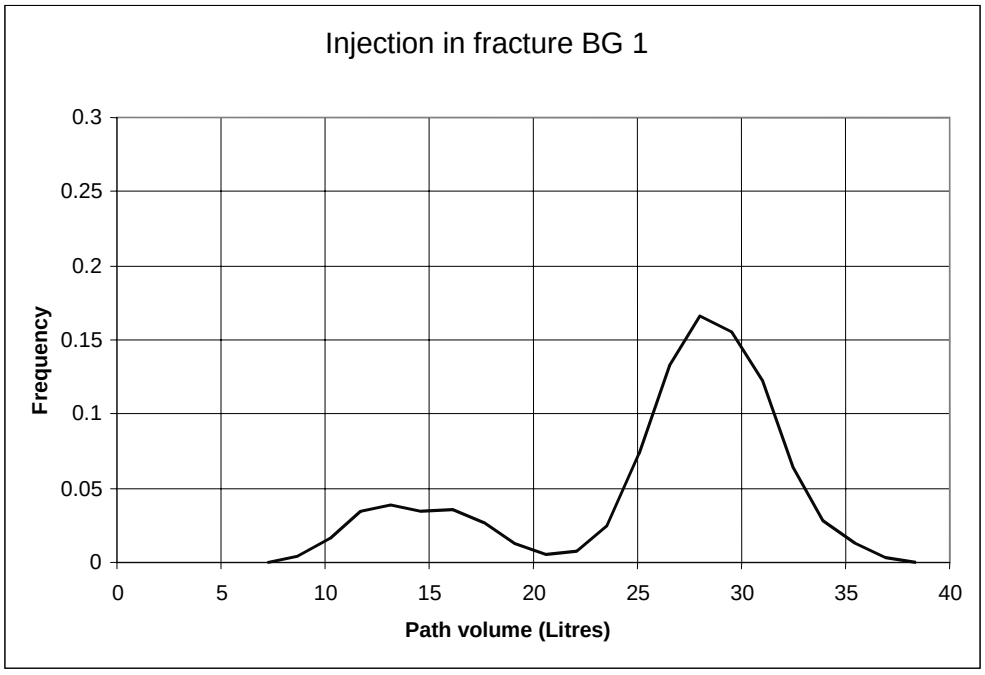

Figure 5-21: *BS2B test, injection in fracture BG 1 – flow path II. Statistical distribution of path volumes. Bin size is 1.485 litre.*

5.3 Structure vs. background fractures

In this section, we test in a simple way the significance of the difference in retention properties between structures – here, Structure #19 - and background fractures. We simply restart the evaluation simulations, using the properties described in Section 5.1.2, but without differentiating between structures and background fractures. Therefore, Figure 5-22 and Figure 5-23 show the breakthrough curves we would obtain by using structure retention properties for the background fractures, while Figure 5-24 and Figure 5-25 show the breakthrough curves we would obtain by using background fracture retention properties for the structure.

Not surprisingly, flow path I is not influenced by changing background fractures properties (compare Figure 5-22 with Figure 5-3). The tracers injected in BG 1 – flow path II - are significantly retarded (compare Figure 5-23 with Figure 5-4), since the structure retention properties are much stronger than the background fracture ones.

When switching to background fracture properties, we find the most reactive tracers injected in Structure #19 to be much less retarded (compare Figure 5-24 and Figure 5-3), which is also expected. However, for this case, the behaviour for flow path II is less intuitive. The response is unaffected (compare Figure 5-25 with Figure 5-4), although a large part of the tracer path (42 m out of 71 m on the average, see Section 5.2) is situated in Structure #19. This shows the time scale difference between the two types of features: the response of any reactive tracer spending a non-marginal part of its travel length in background fractures is governed by the properties of the background fractures, and variations in the properties of the structures are essentially irrelevant, because the time spent in them is comparatively small.

Table 5-3 shows a comparison of average time spent in Structure #19 and in the background fractures for the two tracer paths, and for two cases: a “pure advection/dispersion” tracer, and a “diffusive/non reactive” tracer (here, Iodine injected in Structure #19 and HTO injected in BG 1). Logically, the time spent in background fractures along flow path I is marginal. Note that the ratio of time spent in the background fractures goes down when adding diffusivity (injection of I and HTO). For flow path II, most of the advection/dispersion time is spent in background fractures, and this is also true for diffusive tracers.

Table 5-3: Comparison of average time spent in Structure #19 and in background fractures for various injection cases.

Injection	Tracer	Average time in Structure #19 (hours)	Average time in fractures (hours)	% time in fractures
Structure #19, flow path I	Advection/dispersion	25	0.2	0.8
Structure #19, flow path I	I	71	0.5	0.7
BG 1 flow path II	Advection/dispersion	35	204	85.
BG 1 flow path II	HTO	112	569	83.

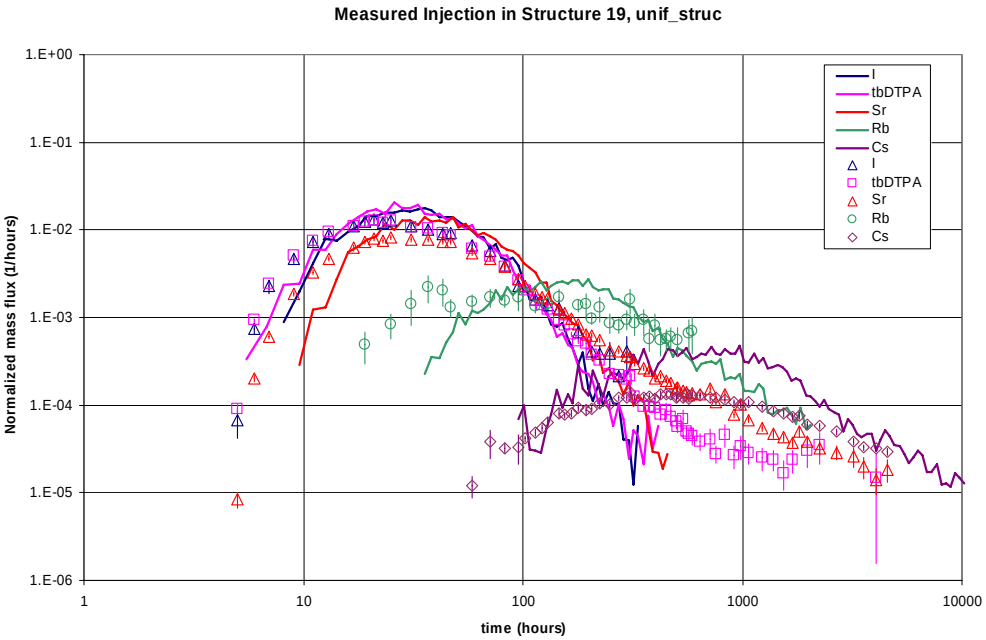

Figure 5-22: *BS2B test, flow path I. Measured and predicted normalized Breakthrough curves. When applying structure retention properties to all geological features.*

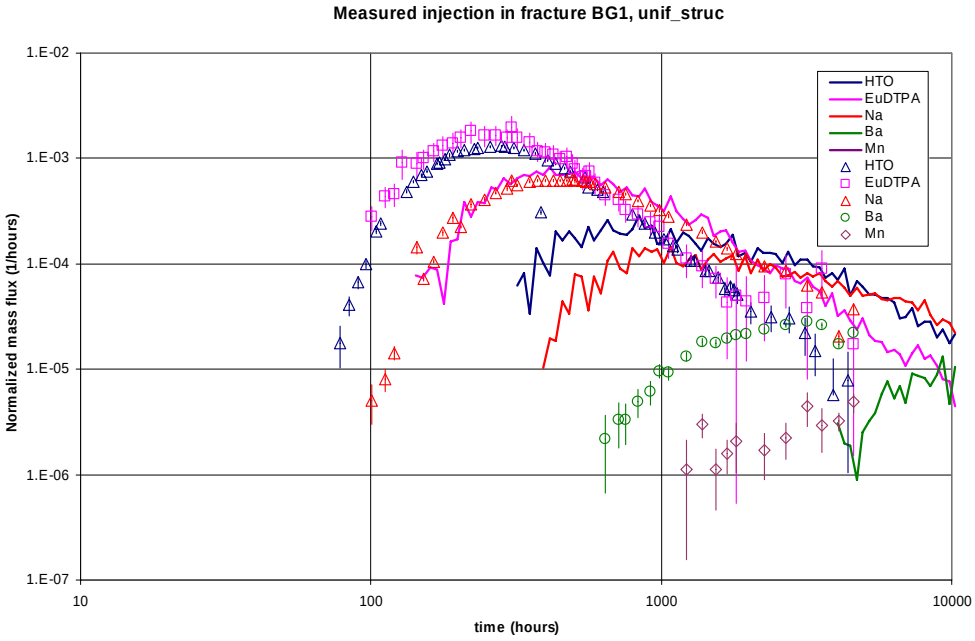

Figure 5-23: *BS2B test, flow path II. Measured and predicted normalized Breakthrough curves. When applying structure retention properties to all geological features.*

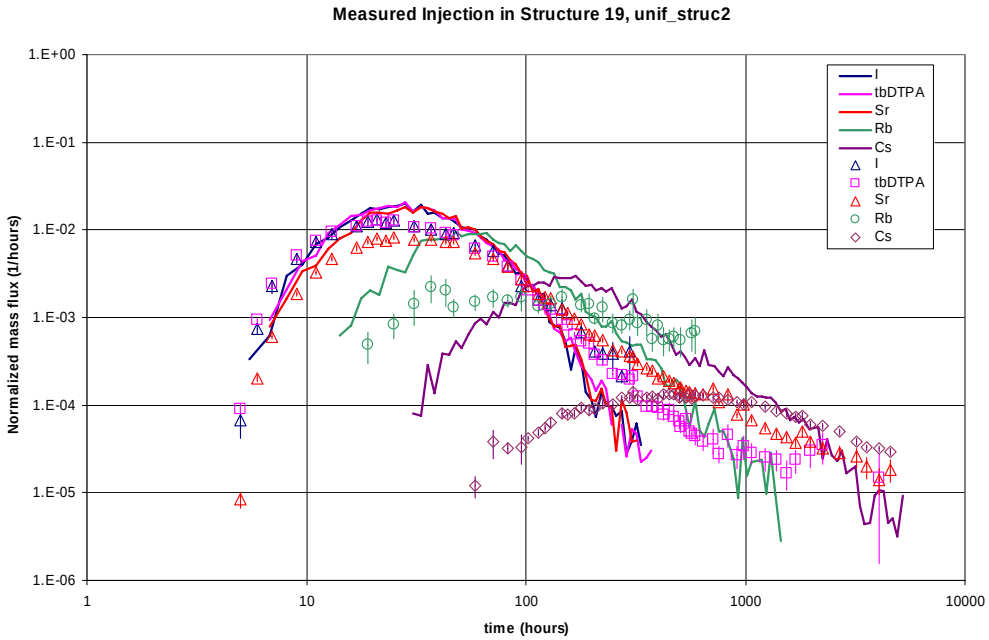

Figure 5-24: *BS2B test, flow path I. Measured and predicted normalized Breakthrough curves. When applying background fracture retention properties to all geological features.*

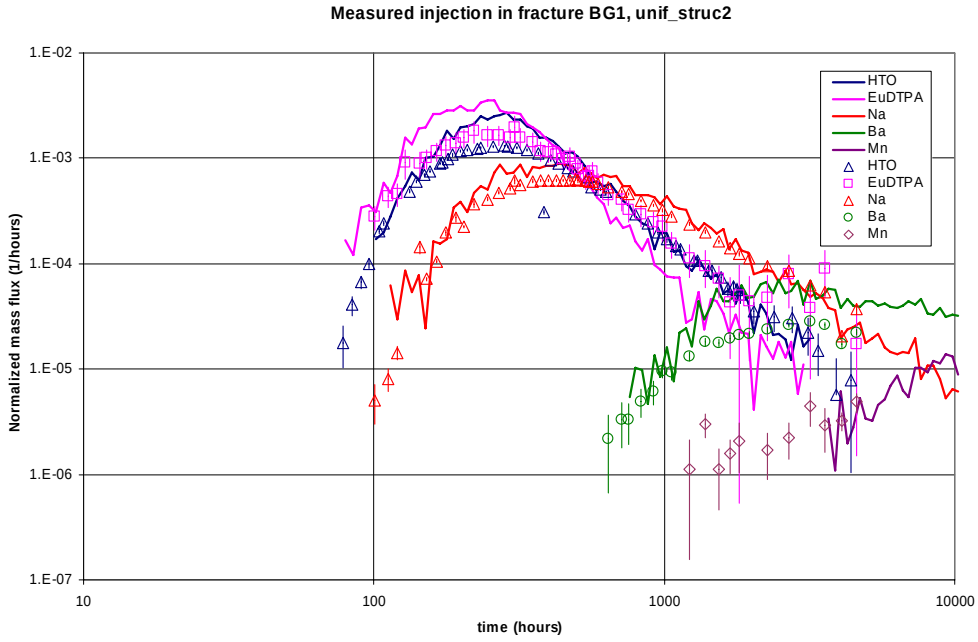

Figure 5-25: *BS2B test, flow path II. Measured and predicted normalized Breakthrough curves. When applying background fracture retention properties to all geological features.*

6 Discussion

6.1 Difficulties

After calibrating the flow and transport properties of the networks using the preliminary CPT-1 to CPT-4 tests, we used data provided by the project to assess the retention properties of the two paths to be tested by reactive tracers. However, our underestimation of the importance of filling/gouge in the background fractures and in Structure # 19 led to a substantial underestimate of the retention properties of the network. Note that, although we had a detailed conceptual model for the microstructure of both Structure #19 and background fractures, we had no information on the actual amount of filling/gouge present in the network, so that we had to make an assumption. The mismatch resulted from a lack of knowledge of a geometrical medium parameter (i.e. amount of filling in the flow network), not from a poor estimate of the process parameters.

When applying the retention properties, we used directly the values provided as TRUE Block Scale Continuation data deliveries. These were generally measured using small amounts of material from drill cores, in general not directly on the site for which they are used. We mentioned already, for example, the use of Structure 20 data to assess the Kd's for Rb and Cs in Structure #19, justified by the geological analogy between the two structures. The resulting values meant an over prediction of retention for these two tracers. In other words, the use of sparse local data to assess retention properties may incur difficulties.

More problematic is the fact that we could not use "average" responses to calibrate the model and then predict and evaluate the reactive transport breakthrough curves. We had to chose one realization of the network and work with it. Using averages could work for studying paths within a structure, where the variability of the response is moderate, even though the structure itself is quite heterogeneous locally: at the scale we are contemplating here (a few tens of meters), flow and transport in a structure are already averaged. This is not quite true when considering the response of the background fractures network. This response is very much reliant on network connections, which are not averaged over a few tens of meters. For example, when generating a number of realizations of the network, a significant portion of them yields an unconnected BG1, preventing any transport simulation. In such instances, the use of averages is meaningless. In other words, the scale we are considering here is probably way below the Representative Elementary Volume (REV) for transport in this network, if such a REV exists. We are therefore relying on a "point statistic" (i.e. one realisation) to make deductions about differences between structures and background fractures.

Here, a major factor in the behaviour of the reactive tracers at experimental time scales seems to be the filling/fault gouge in fractures and structure. In fact, such material, even if pervasively present in the network, as hypothesised in the evaluation part of this work, would still not be of much consequence for very long time scales, because of its limited thickness. It would essentially act as a thin coating and be saturated fairly rapidly. Therefore, the one part of the system that has most influence of its behaviour at the time scale we can investigate is probably not important for the time scale we are really interested in. This does not augur well of our capacity to predict reactive tracer behaviour at performance assessment time scales.

6.2 Findings

Although our predictions for the behaviour of tracers injected in Structure #19 were not satisfactory, the cause for this mismatch was easily traced to an underestimate of the proportion of filling. This could have been avoided by a more thorough knowledge – for this modelling team - of the structure geology. Therefore, we can consider that the behaviour of reactive tracers in structures can be predicted at experimental time scales, provided an accurate knowledge of the micro structure has been gained. In fact, other modelling teams with more experience on the project managed to do so.

An interesting outcome of these experiments and their evaluation may alleviate the burden of characterizing retention properties in networks of background fractures and structures. These two populations (i.e. background fractures and structures) can be studied independently of each other: on one hand, a path originating and finishing in the same structure will be extremely unlikely to leave the structure, because of the structure higher conductivity, and therefore will be insensitive to background fracture network properties. On the other hand, we can use a structure as a "sink" for a path originating in a background fracture. While permitting acceptable recoveries, travel is so much faster in the structure, that we can disregard the part of the transport path in the structure, and consider only reactive transport in the background fractures network. Therefore, the TRUE Block Scale continuation tests have confirmed the feasibility of experimenting with retention of background fractures.

Our model with 1-D channels and complete mixing at intersections does not consider that one flow tube can be responsible for most of the transport in the fracture medium. In fact, for flow path II - injection in BG1 - we notice that the flow first shows a radial pattern within the fracture. Here, it seems that the forced injection, even at a low flow rate, has a strong spreading effect on the flow pattern. This is made possible by the large difference in flow/transport properties between the injection point in BG 1 and the pumping point in Structure #19. It accounts for the fairly large (several metres) spread of the tracer. Such a pattern enhances retention by increasing the exchange area between the flowing volume and immobile zones.

7 Conclusions

The calibration, prediction, and evaluation work reported here were mostly aimed at detecting and understanding differences between background fracture network and structures in terms of tracer retention. Our main findings can be stated in terms of the hypotheses considered at the start of the continuation project.

Microstructural information can provide significant support for predicting transport of sorbing solutes at experimental time scales.

We have shown that microstructural information is required for predicting reactive transport: underestimating the presence of one of the components of microstructure results in flawed predictions. Also, a proper microstructural information will result in realistic prediction of the transport *in structures* at experimental time scales. Prediction of reactive transport *in background fractures* at length scales of a few tens of meters, and at experimental time scales, may be achieved if experimental results for non-reactive transport have been obtained in the same paths, therefore characterizing these paths.

Transport at experimental time scales is significantly different for faults and joints, due to the indicated differences in microstructure and properties".

Indeed, transport is significantly different for structures and for background fractures, as readily shown in Section 5.3. However, contrasts in microstructure and properties are only one aspect of the difference. A structure is a "known" object (although imperfectly known), for which we can define a conceptual framework. For background fracture transport, geometry cannot be known deterministically. At the scale involved, the same network statistical properties can yield realizations with widely different behaviours.

The numerical simulations here strived to predict and understand a well constrained experiment, with the help of numerous previous results, including non-sorbing tracer tests along the same transport paths. Using one - randomly chosen - realization of the network enabled us to reproduce the experiment fairly well. We don't know if this could be done with "any" realisation of the network, of if some unique feature of this particular realization made the calibration possible. Moreover, when studying a nuclear waste repository, we would have to anticipate the behaviour of many possible transport paths, at scales close to the one we studied here (scale of the transport paths from deposition hole to the nearest structure), without a priori knowledge, by the way of non-sorbing tracer tests, of these various transport paths. This will be a much more challenging task, for which we will need to revert to stochastic analyses.

8 References

Andersson, P., Byegård, J. Dershowitz, B., Doe, T., Hermanson, J., Meier, P., Tullborg, E-L., and Winberg, A., 2002. Final report of the TRUE Block Scale projekt 1. Characterisation and model development. Technical Report TR-02-13. SKB, Stockholm.

Byegård, J., and Tullborg, E.-L, 2004. Proposed sorption, porosity and diffusivity data for the modeling of the TRUE Block Scale Continuation sorbing tracer experiment, version 1.1, October 14, 2004, TRUE Block Scale Continuation, SKB, Stockholm.

Darcel, C 2003. TRUE Bloc Scale Continuation, BS2A Support Modelling. Assessment of the feasibility of tracer tests with injection in "background fractures" using a power law fractures length distribution. IPR-03-41, SKB, Stockholm.

Andersson, P., Gröhn, S., Nordqvist, 4., Wass, R., 2004. TRUE Block Scale Continuation Project. BS2B Pretests Crosshole interference, dilution and tracer tests, CPT-1 - CPT- 4. IPR-04-25. SKB, Stockhlolm.

Andersson, P., Byegård, J., Nordqvist, R. and E. Wass. 2005. TRUE Block Scale Continuation Project. BS2B tracer tests with sorbing tracers.IPR-04-25. SKB, Stockhlolm.

Dershowitz, W.; Winberg, A.; Hermanson, J.; Byegård, J.; Tullbord, E-L; Andersson, P.; and Mazurek, M. 2003. A Semi-Synthetic Model of Block Scale Conductive Structures at the Äspö Hard Rock Laboratory, IPR-03-13, SKB, Stockholm.

Rachez X. and Billaux D., 2002. Investigation of the effect of structural model updates on response to simulated tracer tests. Äspö Hard Rock Laboratory International Progress Report IPR-02-26, SKB, Stockholm